Title
Investigation of Effect of Zn on Passive Film for Alloy 600 in High Temperature Primary Water

Author
Jiang, Yifan

Publication Date
2017

Peer reviewed|Thesis/dissertation

Investigation of Effect of Zn on Passive Film for Alloy 600 in High Temperature Primary Water

By

Yifan Jiang

A dissertation submitted in partial satisfaction of the
requirements for the degree of
Doctor of Philosophy
in
Engineering-Materials Science and Engineering
in the
Graduate Division
of the
University of California, Berkeley

Committee in charge:

Professor Thomas M. Devine, Chair
Professor Fiona M. Doyle
Professor Mark Asta
Professor Paulo J.M. Monteiro

Fall 2017

Abstract

Investigation of Effect of Zn on Passive Film for Alloy 600 in High Temperature Primary Water

by

Yifan Jiang

Doctor of Philosophy in Materials Science and Engineering

University of California, Berkeley

Professor Thomas M. Devine, Chair

Due to its excellent corrosion resistance, Alloy 600 has been extensively used as the heat exchanger tubing material in the steam generator (SG) of pressurized water reactor (PWR) in nuclear industry for many years. However, the Alloy 600 is susceptible to stress corrosion cracking (SCC) on the primary side of the tubing, causing safety problems as well as increasing the cost of maintenance. Zn treatment has been applied in recent years in the industry to suppress the SCC problems, but the main mechanism for this effect is not fully understood. Since the surface film is strongly related to SCC initiation, the goal of the research is to understand how Zn affects the surface film growth on Alloy 600. This research focuses on understanding the change of kinetic parameters on oxide formation as well as the change in chemistry and structure on Alloy 600 oxide.

Electrochemical tests are performed to understand how the passive layers respond electronically to the presence of Zn. Alloy 600 samples are oxidized at various potentials from -743 mV $_{SHE}$ to -223 mV $_{SHE}$ in a lab constructed autoclave at simulated PWR PW environment with 0.1ppm Zn addition. EIS is performed *in-situ* to determine how the passive layer changes electrochemically over potential, and cross-section TEM-EDS is conducted to some samples to investigate the film formation.

The passive film formed on Alloy 600 consists of a $(Ni_xFe_{1-x})O$ outer layer, a Cr-rich spinel layer and a Cr_2O_3 inner layer. Zn incorporates into the outer and intermediate layer, and changes the morphology of the outer layer. EIS equivalent circuits based on the TEM results is constructed for each potential, and it is found that Zn largely reduces the rate of oxygen incorporation into the inner layer at potentials below -573 mV $_{SHE}$. Other parameters are not affected by Zn addition in to the solution, which agrees with the TEM results.

Table of Contents

Chapter 1. Introduction 1
1.1 Stress Corrosion Cracking in PWR 1
1.1.1 Introduction to Stress Corrosion Cracking 1
1.1.2 Stress Corrosion Cracking in Pressurized Water Reactor 2
1.2 SCC of Alloy 600 in PWR Steam Generator 2
1.2.1 Factors Affecting the SCC Susceptibility of Alloy 600 2
1.2.2 Relationship between SCC and Passivity of Alloy 600 4
1.3 Inhibition of SCC with Zn addition 5
1.4 Approach in Current Research 5
Chapter 2. Experimental Setup and Procedure 7
2.1 Experimental Setup 7
2.1.1 Pressurized Water Reactor (PWR) System 7
2.1.1.1 Flow Loop 7
2.1.1.2 Autoclave 8
2.1.1.3 Electrolyte 9
2.1.2 Electrochemical Cell Setup 10
2.1.2.1 Working Electrode 10
2.1.2.2 Counter Electrode 10
2.1.2.3 Reference Electrode 10
2.1.2.4 Autoclave Assembly 11
2.2 Experimental Procedure 12
2.2.1 Before Heating 12
2.2.2 Heatup 12
2.2.3 Electrochemical Tests 12
2.2.4 Cooldown 12
2.2.5 Film Characterization Experiments 13
Chapter 3. Characterization of the Passive Film 14
3.1 Introduction 14
3.2 Effect of Potential on Passive Film Formation in Zn Free Solution 14
3.2.1 Structure of Passive Film Formed in Zn free solution 14
3.2.2 Composition of Passive Layer formed on Alloy 600 in Primary Water 20
3.2.3 Comparison of Film oxidized at Various Potentials in Zn free Primary Water 33

3.3 Effect of Potential on Passive Film Formation in Zn Containing Solution 34
3.3.1 Structure of Passive Film Formation Zn Containing Solution..... 34
3.3.2 Composition of Passive Layer formed on Alloy 600 in Zn Containing Primary Water 38
3.3.3 Comparison of Film oxidized at Various Potentials in Zn Containing Primary Water 51
3.4 Effect of Zn in Passive Film Composition on Alloy 600..... 52
Chapter 4. Electrochemical Analysis on Alloy 600 55
4.1 Potentiodynamic Scan on Alloy 600..... 55
4.2 Potentiostatic Polarization on Alloy 600..... 57
4.3 Electrochemical Impedance Spectroscopy for Alloy 600..... 58
4.3.1 EIS results and observation in Zn free and Zn containing Solution 58
4.3.2 Validation of Impedance Results..... 63
4.3.3 EIS Equivalent Circuit..... 65
4.3.3.1 Model Construction..... 65
4.3.3.2 Modification of the Model..... 68
4.3.3.2.1 Low Potential Region (-750 mV $_{SHE}$ to -600 mV $_{SHE}$)..... 68
4.3.3.2.2 Mid Potential Region (-600 mV $_{SHE}$ to -500 mV $_{SHE}$) 69
4.3.3.2.3 High Potential Region (-500 mV $_{SHE}$ to -200 mV $_{SHE}$)..... 71
4.3.4 Fitting Results for Zn containing and Zn free Solutions..... 72
Chapter 5. Discussion..... 78
5.1 Effect of Zn on the Alloy 600 Oxide Chemistry..... 78
5.1.1 Verification of Film Structure with DPA analysis..... 78
5.1.2 Oxide Formation in Zn free Solution..... 81
5.1.2.1 Formation of Outer Layer..... 81
5.1.2.2 Formation of Inner Layer 82
5.1.3 Oxide Formation in Zn containing solution..... 82
5.1.3.1 Formation of Outer Layer..... 82
5.1.3.2 Formation of Inner Layer 84
5.2 Discussion of EIS in the Context of Results of TEM and SEM 84
5.2.1 Overview..... 84
5.2.2 Comparison of fitting parameters 85
5.2.2.1 CPE_{sc}, R_M, and the Alloy/Film Interface..... 86
5.2.2.2 R_{ox}, Z_{W_ox}, CPE_{IL} and the Inner Layer of Cr_2O_3 and MCr_2O_4..... 89

5.2.2.3 R_{red}, Z_{Wred} and Reduction of Hydrogen 93
5.2.2.4 R_{OL}, C_{OL}, and Porous NiO 95
Chapter 6. Conclusions 99
References 100
Appendix 104

Table of Figures

Figure 1-1: Critical Factors for stress corrosion cracking, reproduced from reference [2] 1
Figure 1-2: Schematic of PWR reactor [5] 2
Figure 1-3: Simplified Pourbaix diagram for nickel and iron at 300°C showing the principal pH-potential combinations for PWR primary and secondary water, BWR Normal Water Chemistry (NWC) and BWR Hydrogen Water Chemistry (HWC) and the modes of stress corrosion cracking of Alloy 600, [12], [13] 4
Figure 2-1: Autoclave and pressurized system: 1. autoclave and electrode system, WE – working electrode (Alloy 600), RE – reference electrode (Pt), CE – counter electrode (Pt); 2. storage tank (glass); 3. pressure nitrogen gas; 4. bubbling column (glass); 5. pressure forming gas (4% H_2-balance N_2) bottle; 6. high pressure pump; 7. heat exchanger; 8. safety valve; 9. back pressure regulator; 10. heating element; 11. thermocouple 7
Figure 2-2: Top-down overview of the autoclave 9
Figure 2-3: Sample holder that is inserted from the back of the autoclave and can hold up to 2 electrodes in one holder 9
Figure 2-4: Sample location in the autoclave after loading 11
Figure 3-1: SEM view of the oxide film formed at -700 mV $_{SHE}$ at 320 °C in PWR simulated primary water, showing whisker shape oxides on top and small particles below whiskers. 15
Figure 3-2: TEM cross-section of the oxide film formed at -700 mV $_{SHE}$. In the image, the lower part is the Alloy 600 matrix, whereas the upper part is the deposited Pt layer. 15
Figure 3-3: SEM view of the oxide film formed at -550 mV $_{SHE}$ at 320 °C in PWR simulated primary water, showing whisker shape oxides on top and small particles below whiskers. 17
Figure 3-4: TEM cross-section of the oxide film formed at -550 mV $_{SHE}$. In the image, the lower part is the Alloy 600 matrix, whereas the upper part is the deposited Pt layer. 18
Figure 3-5: SEM view of the oxide film formed at -223 mV $_{SHE}$ at 320 °C in PWR simulated primary water, showing needle- shape oxides and small particles. 19
Figure 3-6: TEM cross-section of the oxide film formed at -223 mV $_{SHE}$. In the image, the lower part is the Alloy 600 matrix, whereas the upper part is the deposited Pt layer. 19
Figure 3-7: EDX mapping of the passive film formed at -700 mV $_{SHE}$ in Zn free primary water. (a) overlaying elemental map. (b) individual elemental maps for Cr, O, Fe, Ni. 21
Figure 3-8: Line scan on different regions of Alloy 600 passive layer oxidized at -700 mV $_{SHE}$ in Zn free primary water. (a) TEM image showing regions of line scans. (b) Line scan of region 1 showing outer layer particles stacking porously and inner layer. (c) Line scan of region 2 showing different orientations of outer layer particles and inner layer. (d) Line scan of region 3 showing some outer layer parts and mostly inner layer. 25
Figure 3-9: EDX mapping of the passive film formed at -550 mV $_{SHE}$ in Zn free primary water. (a) overlaying elemental map. (b) individual elemental maps for Cr, O, Fe, Ni. 26
Figure 3-10: Line scan on different regions of Alloy 600 passive layer oxidized at -550 mV $_{SHE}$ in Zn free primary water. (a) TEM image showing regions of line scans. (b) Line scan of region 1 showing different orientations of outer layer particles and inner layer. (c) Line scan of region 2 showing mostly inner layer. (d) Line scan of region 3 showing porous outer layer particles and inner layer. 29
Figure 3-11: EDX mapping of the passive film formed at -223 mV $_{SHE}$ in Zn free primary water. (a) overlaying elemental map. (b) individual elemental maps for Cr, O, Fe, Ni. 30

Figure 3-12: Line scan on different regions of Alloy 600 passive layer oxidized at -223 mV $_{SHE}$ in Zn free primary water. (a) TEM image showing regions of line scans. (b) Line scan of region 1 showing thin outer layer and inner layer. (c) Line scan of region 2 showing both outer layer particle and compact inner layer. 33
Figure 3-13: SEM view of the oxide film formed at -700 mV $_{SHE}$ at 320 °C in Zn containing PWR simulated primary water, showing octahedral oxides and small particles. 35
Figure 3-14: TEM cross-section of the oxide film formed at -700 mV $_{SHE}$. In the image, the lower part is the Alloy 600 matrix, whereas the upper part is the deposited Pt layer. 35
Figure 3-15: SEM view of the oxide film formed at -550 mV $_{SHE}$ at 320 °C in Zn containing PWR simulated primary water, showing octahedral oxides and small particles. 36
Figure 3-16: TEM cross-section of the oxide film formed at -550 mV $_{SHE}$. In the image, the lower part is the Alloy 600 matrix, whereas the upper part is the deposited Pt layer. 36
Figure 3-17: SEM view of the oxide film formed at -223 mV $_{SHE}$ at 320 °C in Zn containing PWR simulated primary water, showing small particles. 37
Figure 3-18: TEM cross-section of the oxide film formed at -223 mV $_{SHE}$. In the image, the lower part is the Alloy 600 matrix, whereas the upper part is the deposited Pt layer. 38
Figure 3-19: EDX mapping of the passive film formed at -700 mV $_{SHE}$ in Zn containing primary water. (a) overlaying elemental map. (b) individual elemental maps for Cr, O, Fe, Ni, Zn. 39
Figure 3-20: Line scan on different regions of Alloy 600 passive layer oxidized at -700 mV $_{SHE}$ in Zn containing primary water. (a) TEM image showing regions of line scans. (b) Line scan of region 1 showing outer layer, inner layer and oxide below inner layer. (c) Line scan of region 2 showing mostly inner layer. (d) Line scan of region 3 showing outer layer particles and inner layer. 43
Figure 3-21: EDX mapping of the passive film formed at -550 mV $_{SHE}$ in Zn containing primary water. (a) overlaying elemental map. (b) individual elemental maps for Cr, O, Fe, Ni, Zn. 45
Figure 3-22: Line scan on different regions of Alloy 600 passive layer oxidized at -550 mV $_{SHE}$ in Zn containing primary water. (a) TEM image showing regions of line scans. (b) Line scan of region 1 showing outer layer, inner layer and oxide below inner layer. (c) Line scan of region 2 showing outer layer particles and inner layer. (d) Line scan of region 3 showing outer layer particles and inner layer. 48
Figure 3-23: EDX mapping of the passive film formed at -223 mV $_{SHE}$ in Zn containing primary water. (a) overlaying elemental map. (b) individual elemental maps for Cr, O, Fe, Ni, Zn. 49
Figure 3-24: Line scan on different regions of Alloy 600 passive layer oxidized at -223 mV $_{SHE}$ in Zn containing primary water. (a) TEM image showing regions of line scans. (b) Line scan of region 1 showing outer layer and inner layer. (c) Line scan of region 2 showing outer layer particles, inner layer and oxide below inner layer. 51
Figure 3-25: Compositional variance of outer layer on Alloy 600 formed in (a) Zn free solution, (b) Zn containing solution. 53
Figure 4-1: Example of polarization of Alloy 600 in both Zn free and Zn containing primary water containing 1200ppm B, 2ppm Li at 320 ºC 1800psi. Each test was conducted from low potential to high potential at 1mV/s scan rate. The pH of the solution was calculated to be 7.28 at 320 ºC. 56
Figure 4-2: Pourbaix Diagram of Alloy 600 at 320ºC and 2250psi in water containing H_3BO_3 and LiOH constructed by Kaufman [35]. 57

Figure 4-3: I-V relationship for Alloy 600 in Zn containing and Zn free solution oxidized for 4 hrs. at each potential for three different runs. Error bars represent the standard error between three sets of tests at each potential. 58
Figure 4-4: a) Bode plot, b) phase angle plot, c) Nyquist plot for Alloy 600 in Zn free solution at 320ºC and 1800psi. Each impedance spectrum was obtained after 4-hr. static polarization..... 60
Figure 4-5: a) Bode plot, b) phase angle plot, c) Nyquist plot for Alloy 600 in Zn containing solution at 320ºC and 1800psi. Each impedance spectrum was obtained after 4-hr static polarization. 62
Figure 4-6: (a) Kramers-Kronig transformation, and (b) results with 2 scanning directions: high-to-low and low-to-high for Alloy 600 oxidized at -743 mV $_{SHE}$ for 4hrs in Zn containing PW water at 320 ºC and 1800 psi. 65
Figure 4-7: Schematic illustration of possible reactions and transport through the passive film based on PDM and MCM. 66
Figure 4-8: (a) circuit element to start with. (b) Circuit elements representing reactions at the inner layer interfaces and transport through inner layer 67
Figure 4-9: (a) Equivalent circuit for potentials -750 mV $_{SHE}$ to -600 mV $_{SHE}$ (b) Example of fitting results with this model at -723 mV $_{SHE}$ 69
Figure 4-10: (a) Equivalent circuit model for potentials -600 mV $_{SHE}$ to -500 mV $_{SHE}$. (b) Example of fitting at potential -573 mV $_{SHE}$. 70
Figure 4-11: (a) Equivalent circuit model for potentials between -500 mV $_{SHE}$ and -200 mV $_{SHE}$. (b) Example of fitting at –potential 323 mV $_{SHE}$..... 72
Figure 4-12: (a) Impedance modulus and (b) Phase angle fitting for Alloy 600 in Zn free primary water at 320 ºC and 1800psi. Points- Experimental values. Solid lines- Curve fitting 74
Figure 4-13: (a) Impedance modulus and (b) Phase angle fitting for Alloy 600 in 0.1ppm Zn containing primary water at 320 ºC and 1800psi. Points- Experimental values. Solid lines- Curve fitting 76
Figure 5-1: DPA analysis of Alloy 600 based on TEM results using (Ni,Fe)-Cr-Water pseudo-ternary phase diagram [49]. 79
Figure 5-2: Overall morphology and composition of passive layer formed on Alloy 600 in (a) Zn free and (b) Zn containing solutions. Different colors represent difference in compositions. 81
Figure 5-3: Summary of impedance equivalent circuits for Alloy 600 85
Figure 5-4: Fitting results of seven different tests (three tests in Zn free solution and four tests in Zn containing solution) for (a) Yo_{SC}, (b) α_{SC}, (c) $C_{SC_eff}^{-2}$and (d) R_M representing the alloy/Cr_2O_3 interface. Each line shows one sample oxidized at different potentials from -743mV $_{SHE}$ to -223mV $_{SHE}$. 89
Figure 5-5: Fitting results of seven different tests (three tests in Zn free solution and four tests in Zn containing solution) for (a) Yo_{IL}, (b) α_{IL}, (c) R_{ox} and (d) σ_{ox} representing the Cr_2O_3, MCr_2O_4 and IL/OL interface. Each line shows one sample oxidized at different potentials from -743mV $_{SHE}$ to -223mV $_{SHE}$. 93
Figure 5-6: Fitting results of seven different tests (three tests in Zn free solution and four tests in Zn containing solution) for (a) R_{red} and (b) σ_{red} representing the hydrogen reduction reaction at IL/OL interface. Each line shows one sample oxidized at different potentials from -743mV $_{SHE}$ to -223mV $_{SHE}$. 95
Figure 5-7: Fitting results of seven different tests (three tests in Zn free solution and four tests in Zn containing solution) for $R_{OL}C_{OL}$ representing the porous outer layer of whiskers and particles. Each line shows one sample oxidized at different potentials from -743mV $_{SHE}$ to -223mV $_{SHE}$.. 98

Figure A-1: Polarization curves for Alloy 600 in PWR Primary water at 320ºC at 1mV/s. The plot includes 2 scans in Zn free solution and 5 scans in Zn containing solution. 104

List of Abbreviations

PWR	Pressurized Water Reactor
PW	Primary water
SCC	Stress corrosion cracking
IGSCC	Intergranular stress corrosion cracking
PWSCC	Primary water stress corrosion cracking
S	Solution
OL	Outer layer (whiskers for Zn free solutions and octahedral particles for Zn containing solutions)
IL	Inner layer: Cr_2O_3 with spinel
OL/S	Outer layer/solutioninterface
IL/OL	Inner layer/ outer layer interface
M/IL	Alloy/inner layer interface
C	Capacitance
$\varepsilon/\varepsilon_r$	Relative permittivity of material
ε_o	Permittivity of vacuum
A	Area of the sample
l	thickness of oxide/ thickness of pore
PDM	Poind defect model
MCM	Mixed conduction model
Z	Impedance
Z_{CTR}	Impedance associated with charge transfer reaction
Z_w	Warburg impedance
i_{total}	Total current density
i_{red}	Current density of hydrogen reduction reaction
i_{ox}	Current density of film formation in the inner layer
i_{cap}	Current density related to charging/discharging of the inner layer

k_i	Rate constants for reactions taking place at interfaces
Z_{red}	Impedance associated with hydrogen reduction reaction
Z_{ox}	Impedance associated with film formation in the inner layer
Z_{cap}	Impedance associated with charging/discharging of the inner layer
CPE	Constant phase element
Y_o	pre-exponential term for constant phase element
α	Exponential term for constant phase element
W	Warburg element
σ	Warburg coefficient
ω	angular frequency
j	Imaginary unit
$M_{Cr}^{\delta-}$	Metal cation in Cr site in the oxide
$M_{aq}^{3-\delta}$	Aqueous metal cation
V_{Cr}^{3-}	Chromium vacancy in oxide
V_o^{2+}	Oxygen vacancy
Z_{SC}	Space charge impedance at metal/inner layer interface
C_{SC_eff}	Effective space charge capacitance associated with charging/discharging of double layer at metal/inner layer interface
Yo_{SC}	Pre-exponential term for space charge capacitance that is located at the metal/inner layer interface
α_{SC}	Exponential term for space charge capacitance located at the metal/inner layer interface
R_M	Faraday resistance associated with metal oxidation at metal/inner layer interface
R_{ox}	Charge transfer resistance associated with oxygen injection and cation dissolution at the IL/OL interface
σ_{ox}	Warburg coefficient associated with cation/oxygen vacancy transport phenomena across the inner layer
R_{red}	Charge transfer resistance associated with hydrogen reduction reaction at the IL/OL interface

σ_{red}	Warburg coefficient associated with hydrogen transport in spinel
Yo_{IL}	Pre-exponential term for inner layer (Cr_2O_3 and chromite)
α_{IL}	Exponential term for inner layer (Cr_2O_3 and chromite)
R_{ad}	Resistance associated with adsorption process at IL/OL interface at potentials above -500mV $_{SHE}$
L_{ad}	Inductance associated with adsorption process at IL/OL interface at potentials above -500mV $_{SHE}$
C_{OL}	Capacitance of the outer porous layer
R_{OL}	Resistance associated with the outer porous layer due to current passing through

Acknowledgement

I would like to acknowledge and thank my advisor and mentor, Professor Thomas M. Devine for his guidance and support both personal and technical. Without him I would not have completed the research.

I want to thank Dr. Chris Kumai, Dr. Brian Patrick for all the friendship and discussion throughout my research. I received a lot of great suggestion and encouragement from them, especially regarding the experimental setup and troubleshooting. I appreciate all the discussion with Professor Digby D. Macdonald and his group members regarding the EIS data. I would also like to thank Professor Andrew Minor, Dr. Karen Bullisto, Chengyu Song and John Turner for all the training and support regarding the work at Lawrence Berkeley Lab. Without them, I would not have completed the TEM/SEM characterization work of my research.

Finally I appreciate all the love and care from my parents. I want to thank them for always being supportive with my work, both mentally and financially.

Work at the Molecular Foundry was supported by the Office of Science, Office of Basic Energy Sciences, of the U.S. Department of Energy under Contract No. DE-AC02-05CH11231.

Chapter 1. Introduction

1.1 Stress Corrosion Cracking in PWR

1.1.1 Introduction to Stress Corrosion Cracking

Stress corrosion cracking (SCC) is referred to as cracking due to a conjoint process of corrosion and straining of a susceptible material due to a residual or applied force [1]–[3]. As one of the environmentally assisted cracking (EAC) mechanism, SCC could occur without prior warning and cause catastrophic consequences, and thus it has brought great interest for investigators to understand the process in order to avoid the failure.

Figure 1-1: Critical Factors for stress corrosion cracking, reproduced from reference [2]

There are three factors essential for SCC to occur: a susceptible material, tensile stress and a corrosive environment, as described in Figure 1-1. Tensile stress could either be inherited from the manufacturing process, or be generated during service. The corrosion environment for different materials varies, but it generally involves an aqueous electrolyte as media. Material susceptibility to SCC is related to the microstructure and composition of the metal or alloy. In summary, SCC is a localized corrosion that occurs below the designed strength of the material, and that is generally believed to be a combination of material-environment affect.

Just like other forms of cracking, the occurrence of SCC consists of two parts, crack initiation and propagation. The initiation process is generally believed to be associated with growth of a passive layer, which relates to a mixed effect from material property and environment, and can take up to decades of years. At this stage, a passive film grows as a corrosion product, where cracks are established. Propagation, on the other hand, is a combinative consequence of stress and environment when the crack tip stress intensity (K_I) grows beyond a critical value (K_{ISCC}) [2], [4].

Different models have been developed to explain the SCC propagation process, among them, active path dissolution model, film rupture model, film-induced cleavage model, and coupled environment fracture model (CEFM) [1]. Although no decisive statement has been established, it is agreed that SCC propagation is also associated with a passive film on the susceptible material. In order to minimize SCC, one or more of the three factors described above need to be

controlled so that the crack tip does not reach the threshold level, and as a result the passive film is affected by controlling the factors.

1.1.2 Stress Corrosion Cracking in Pressurized Water Reactor

Reliability of nuclear plants is very important to the nuclear industry due to high economic loss during repair and shut-down for the whole plant. Among all the degradation failures, SCC is one of the most severe problems.

In pressurized water reactor (PWR), a steam generator transfers the heat energy generated from the reactor vessel (primary loop) to vaporize water to steam that is used to generate electricity at the turbine (secondary loop) [3]. A schematic of PWR power plant is shown in Figure 1-2. SCC failures have been observed in worldwide PWR since the mid-1970s, and most of the failures are found intergranular in Ni-based alloys, particularly in Alloy 600, 132, 182, and 718 located at SG tubings, pressure vessel nozzles, and in the shells of the primary loop (PWSCC) [2]. SCC is also observed in Alloy 600 in secondary loop (ODSCC).

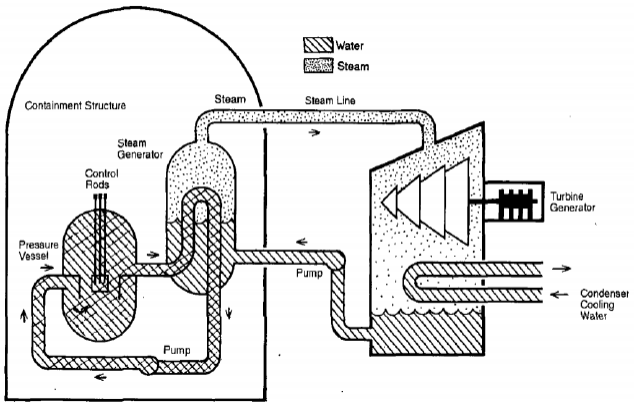

Figure 1-2: Schematic of PWR reactor [5]

1.2 SCC of Alloy 600 in PWR Steam Generator

As is mentioned before, the steam generator (SG) is one of the locations where PWSCC occurs in PWR. A SG is crucial to PWR because it exchanges the heat energy to drive turbine for electricity generation. It also creates a barrier between radiated primary loop and non-radiated secondary loop / environment. The material used for SG tubing is Alloy 600.

1.2.1 Factors Affecting the SCC Susceptibility of Alloy 600

Alloy 600 is an austenitic Ni-based alloy that contains 14-17% Cr and 6-10% Fe. It is used in PWR SG due to the excellent corrosion resistance to chloride induced transgranular SCC (TGSCC) and its low corrosion rate in oxygenated water [6]. It is found that the susceptibility of Alloy 600 not only is affected by the primary water environment, but also is dependent on the metallurgical structure. The nominal composition of the alloy is shown below in Table 1-1 [7], [8].

Table 1-1: Composition of Alloy 600 (wt%)

	Ni	Cr	Fe	Mn	Cu	Si	C	S
Alloy 600	≥72.0	14.0-17.0	6.0-10.0	≤1.0	≤0.50	≤0.50	≤0.15	≤0.015

It is proved by several studies [2], [3] that carbide morphology and cold work affect the SCC susceptibility of Alloy 600. Usually found in the form of M_7C_3, the carbide in Alloy 600 is formed with carbon and chromium. Carbides can be transgranular or intergranular, and studies have found that the formation of intergranular carbides along the grain boundaries increases the alloy resistance to PWSCC, whereas alloys with transgranular carbides are more susceptible to PWSCC [2], [9]–[11]. Was et al. [10] showed that Alloy 600 with carbides along grain boundaries had a delayed initiation and shallower crack depths than alloys with carbides inside grains. One explanation is that intergranular carbides act as obstacles for grain boundary sliding and thus reduces the crack growth [10]. In order to create a favored microstructure with intergranular carbides, high temperature mill annealing and thermal treatment are usually performed on alloys.

Primary water environment also accounts for the Alloy 600 PWSCC susceptibility. Aside from the radiation effects, the primary loop of PWR operates at 310 ºC – 325 ºC and 15.5 MPa, and contains boron, lithium and hydrogen in the solution [5]. Boron is added in form of H_3BO_3 as a neutron absorber to control neutron reaction in the reactor vessel. Due to its low neutron cross-section and improbability to fission in the reactor core, lithium is added as LiOH to control the pH of the solution to keep it between 6.8 and 7.4 at the operating temperature. Oxygen content is strictly controlled in the solution ($[O_2] < 10$ppb), and hydrogen gas (25-50cc/kg) is dissolved in the solution in order to control the electrochemical potential of the system [2]. PWSCC is strongly related with the electrochemical potential and pH, and is found in the potential range around the Ni/NiO equilibrium potential, as shown in Figure 1-3 [12], [13]. This is also part of the potential region for which this research is concerned.

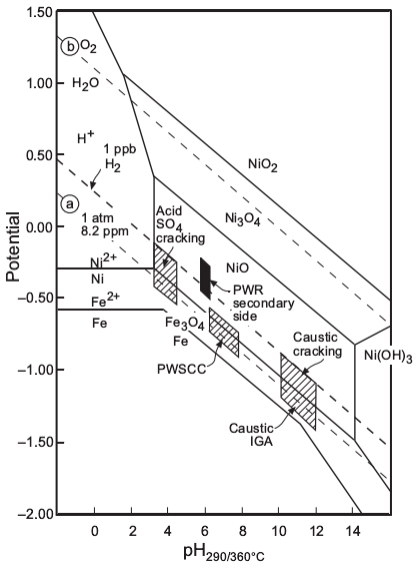

Figure 1-3: Simplified Pourbaix diagram for nickel and iron at 300°C showing the principal pH-potential combinations for PWR primary and secondary water, BWR Normal Water Chemistry (NWC) and BWR Hydrogen Water Chemistry (HWC) and the modes of stress corrosion cracking of Alloy 600, [12], [13]

1.2.2 Relationship between SCC and Passivity of Alloy 600

As mentioned before, SCC initiation is associated with the passive film, where cracks are created at defective sites. Film formation is also related to SCC propagation, as the formation of oxides along crack walls affects the crack growth rate [1].

The relationship between SCC and the surface film is also shown by several researchers [14]–[17]. J. Flis found that formation of γ-Fe_2O_3 accounts for SCC of mild steel in nitrate acids at 75 ºC, whereas Fe_3O_4 prevents SCC [14]. Kumai and Devine [15] used in-situ SERS technique to investigate the surface film on 304 stainless steel, and related IGSCC of 304SS in BWR environment with the inadequate amount of γ-Fe_2O_3 oxide.

As for Alloy 600, several researchers [16], [17] investigated the relationship between SCC and water chemistry, and agreed that the oxide films formed on Alloy 600 show various morphologies and chemistry with change in dissolved hydrogen concentration, which corresponds to the protectiveness of the film and SCC initiation. According to Panter et al., oxygen was transported through the oxide film into the alloy via vacancies, and created grain boundary oxides that embrittled the grain boundary of the alloy and enhanced IGSCC [18]. As a result, since the vacancies were created through selective oxidation of metal, the passive film growth would be associated with IGSCC.

It is generally agreed that the passive film formed on Alloy 600 in PW is composed of duplex layers— a chromium-rich inner layer and an iron/nickel-rich outer layer. Panter, et al. [18] investigated the oxide layers formed on Alloy 600 in PW at 360°C and found that the passive film formed after 300 hours was comprised of an outer layer of sparse, large crystallites of $NiFe_2O_4$ (at least 200nm), a more compact middle layer of $Ni(Fe/Cr)_2O_4$ crystallites (~50nm), and a 5nm inner layer of Cr_2O_3. It was suggested by the author that only the inner Cr_2O_3 layer

performs as a barrier for IGSCC. Sennour et al. also studied Alloy 600 at 325 °C, and found a precipitation-driven external spinel layer of large $Ni_{(1-z)}Fe_{(2+z)}O_4$ crystallites, an internal continuous spinel layer of mixed iron and nickel chromite ($Ni_{(1-x)}Fe_xCr_2O_4$), and nodules of Cr_2O_3 between the spinel and the alloy [19]. Machet et al. conducted *in-situ* XPS analysis on Alloy 600 for short time oxidation, and found that the passive film consisted of Cr_2O_3 inner layer, $Cr(OH)_3$ (transformed to Cr_2O_3 over time) and $Ni(OH)_2$ outer layer[20]. This article also confirmed the transport of Cr^{3+} and Ni^{2+} through the oxide, and $Ni^{2+}_{(aq)}$ release into solution. F. Wang and Devine [21] reported similar results using *in-situ* SERS that the Alloy 600 grew an inner layer of Cr_2O_3 and outer layer of Cr-rich chromite $(Ni/Fe)Cr_2O_4$. The existence of NiO could not be distinguished, because it overlapped with the signal of Cr_2O_3.

1.3 Inhibition of SCC with Zn addition

The BWR experience showed benefits on dose reduction and corrosion inhibition with Zn^{2+} addition, so Zn cations in the form of zinc acetate was originally added to Primary water in order to reduce the activity buildup in PWR [2], [22]. It was surprising to find that Zn^{2+} addition in primary water also reduced PWSCC by changing the chemical composition and structure of oxide film formed on austenitic steels and nickel-based alloys [22]–[28]. It was found by Liu et al. that Zn^{2+} substitutes the tetrahedral sites of Ni^{2+} and Fe^{2+}, and $ZnFe_2O_4$ and $ZnCr_2O_4$ are formed on 316L SS and 304 SS [27], [28]. With long time immersion in Zn containing primary water at 573K, the thickness of both the ferrite outer layer and chromite inner layer are reduced. With the formation of a more protective film ($ZnCr_2O_4$), the rate of dissolution for metal ions is largely reduced.

Kawamura [23] showed that at 360°C, with 10ppb Zn addition, pre-filmed mill-annealed (MA) Alloy 600 has better SCC resistance, as the outer layer of $NiFe_2O_4$ is eliminated whereas the inner layer of $Fe_xNi_{(1-x)}Cr_2O_4$ is also thinned, and Zn is incorporated into inner tetrahedral sites of the spinel oxide ($Zn_{(y+z)}Fe_{(x-y)}Ni_{(1-x-z)}Cr_2O_4$) to enrich Cr content. SCC propagation rate of prepassivated Alloy 600 is also reduced by 10%. Hanson found that besides the substitution of Ni/Fe with Zn in chromite and ferrite, Zn-containing ferrite crystals were smaller in size and was able to delay the ingress of water toward inner layer [25].

J. Huang's study showed similar results for Alloy 690, with a passive film thinning effect for up to 150 ppb Zn, which was added in the form of ZnO. With Zn injection, both Ni^{2+} and $Fe^{2+}$are replaced in the tetrahedral sites in spinel crystals, forming a $ZnFe_2O_4$ external layer and $ZnCr_2O_4$ internal layer [26].

It has also been found that Zn injection in the solution resulted in a reduction of corrosion rate and release rate of both Alloy 600 and Alloy 690 [22]. It was suggested that Ni release rate into the solution was largely impeded by Zn, whereas Fe release rate was only affected in the initial stage when there was an increase in soluble Fe.

1.4 Approach in Current Research

Although much research has been conducted on Alloy 600 to investigate the change in oxide chemistry and structures, the kinetics and process of Zn incorporation into the film remain unclear. In order to understand the effect of Zn on the oxidation process, *in-situ* electrochemical

impedance spectroscopy (EIS) is applied in a range of potentials to understand the kinetics of film formation, and *ex-situ* cross-sectional TEM is used to support the kinetic study as well as to study the chemical composition and structure of the film.

All the in-situ experiments and alloy oxidation were conducted in a lab built water system that simulates the primary water condition at 320 ºC and 1800psi. One advantage of the autoclave system in this study is that the autoclave and tubings that are exposed to high temperature environment are all made with high purity grade II titanium rather than Ni/ SS. As a result, we are able to eliminate saturation of Fe and Ni ions in the pressurized solution that could affect the film formation.

Chapter 2. Experimental Setup and Procedure

2.1 Experimental Setup

The system simulating PWR water loop is used for the experiments and a schematic experimental setup is shown in Figure 2-1. As is shown in the figure, a single-path water loop is constructed, where room temperature primary water (2 ppm Li, 1200 ppm B) is deaerated and is transferred to the autoclave (#1) from a water tank (#2) through the bubbling water column (#4), the high pressure pump (#6), a heat exchanger (preheater, #7). The water then exits the autoclave and goes back through the heat exchanger before it is disposed in the sink. The temperature inside the autoclave is controlled to approximately 320 °C, and the pressure is set to approximately 1800 psi.

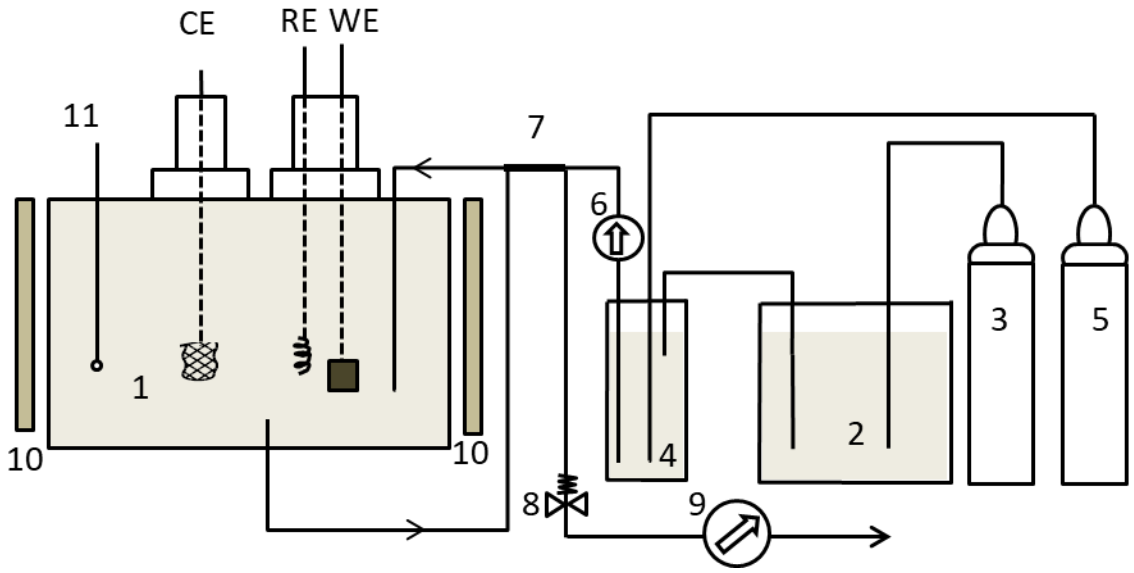

Figure 2-1: Autoclave and pressurized system: 1. autoclave and electrode system, WE – working electrode (Alloy 600), RE – reference electrode (Pt), CE – counter electrode (Pt); 2. storage tank (glass); 3. pressure nitrogen gas; 4. bubbling column (glass); 5. pressure forming gas (4% H_2- balance N_2) bottle; 6. high pressure pump; 7. heat exchanger; 8. safety valve; 9. back pressure regulator; 10. heating element; 11. thermocouple

2.1.1 Pressurized Water Reactor (PWR) System

The system is constructed to conduct electrochemical tests at high temperature and high pressure conditions.

2.1.1.1 Flow Loop

The piping and Swagelok fittings exposed to high temperature environment are all constructed from Grade II Titanium to eliminate possible contamination from metal ions introduced into the solution. It is possible that Ti cations will be present in the solution. However, using Auger electron spectroscopy Mintz and Devine [29] investigated the composition of the passive films formed on Alloy 600 in an all Ti system and did not detect Ti^{4+} in the passive film although Ti^{4+} could be present in the solution.

The solution is stored and deaerated using a 10-gallon water tank. Over 40 liters of solution is deaerated with pure nitrogen using two fritted tubes with 40-60μm pore size.

Two borosilicate water columns (1.57" diameter, 64" height) are used to further deaerate the solution, and to dissolve hydrogen gas using forming gas (4%H_2- balance N_2). Each column is equipped with a gas bubbler at the bottom, with a solution inlet at the top and outlet at the bottom. The gas outlet is located at the top of the column. The water tank and two bubbling columns each has a gas outlet at the top that is connected to a flask filled with water to avoid further oxygen contamination.

Three pumps are used in the experiment. Two Pulsafeeder Model 680-S-E 3000psi diaphragm pumps transfers the solution from the water tank to the two water columns in sequence, and the high pressure stainless steel NEPTUNE chemical pump (Model Number: 500-S-N3HP-T15) is used between the water column and the Ti coaxial heat exchanger. The heat exchanger efficiently uses the water exiting the autoclave to preheat the water entering the autoclave. When passing through the pump, the solution does contact a small amount of stainless steel; however the temperature of the water is approximately 20°C so that very few iron and nickel cations are injected into the water. The low concentration of iron and nickel in the solution is confirmed by previous research conducted in the group [15], [21], [29]. The flow rate is controlled at 0.2GPH.

The heat exchanger is composed of 1/4" and 1/8" OD Ti tubing, where the heated solution goes through the narrow tubing and unheated solution goes through the wider tubing. The concentric heat exchanger is constructed with 1/8" OD tubing inserted into 1/4" OD tubing, so that the hot solution coming out from the autoclave not only preheats the cold solution before it enters the autoclave, but also so that the hot solution is cooled before flowing back to the back pressure regulator and being disposed.

Pressure is maintained at 1800 psi using a pressure regulator. A bleeder valve and rupture disk are used with the backpressure regulator to prevent inadvertent overpressures. After passing through the back pressure regulator, the solution is disposed to the sink so that the solution going through the autoclave is kept fresh during the experiment.

2.1.1.2 Autoclave

The autoclave is constructed with titanium to eliminate unwanted iron, nickel, and chromium ions dissolving into the solution. The body is cylindrical, with a water inlet located at the back of autoclave and a water outlet located at the front. Two sample holders are connected from the back of the autoclave in to the cylindrical chamber, which can hold up to 50ml solution. Figure 2-2 and Figure 2-3 show both the autoclave body and the sample holder. Heating rods can be inserted from the back of the autoclave through the body to the front to ensure uniform heating. A thermocouple is installed at the front of the autoclave next to the water outlet to monitor temperature and control the heating system.

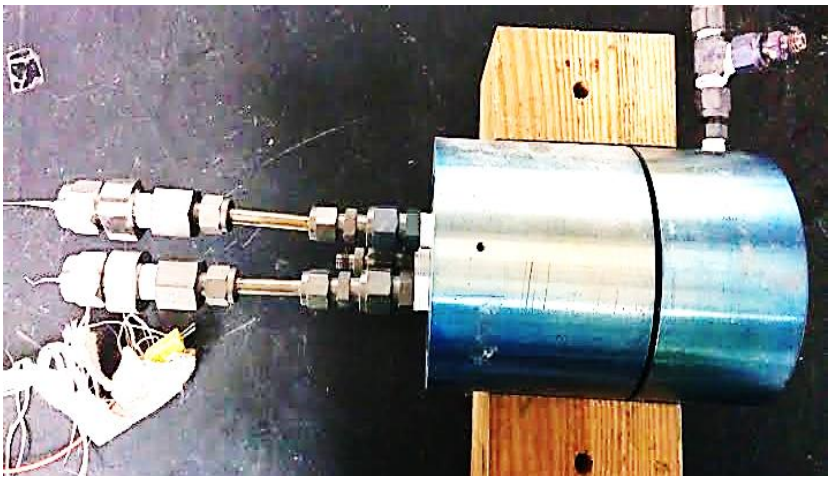

Figure 2-2: Top-down overview of the autoclave.

Figure 2-3: Sample holder that is inserted from the back of the autoclave and can hold up to 2 electrodes in one holder

In order to seal the autoclave without deforming the material with high pressure, an O-ring made from 0.05mm diameter gold wire (99.95% metal basis) is used between the autoclave between the front and the back of the autoclave body.

2.1.1.3 Electrolyte

In order to simulate the primary water environment where Alloys 600 are used, 1200 ppm (μg/g) B (as boric acid H_3BO_3), and 2 ppm Li (as lithium hydroxide LiOH) solution is added to double deionized water. The pH of the solution is calculated to be 7.28 at 320°C using the software developed by Macdonald [30]. An additional 100 ppb Zn (as zinc acetate dihydrate) is added to the solution in order to determine the Zn effect on the sample's passive films. Industry found that the amount of zinc in the film, which was an indication of the effectiveness of Zn injection to PWSCC inhibition, was determined by the term "integrated zinc concentration", "ppb-mo" [2]. Thus, it is assumed that a higher Zn addition in solution could lead to a similar result to long exposure time. Although it is shown from industry that only up to 30ppb of Zn is applied in line [22], 100ppb of Zn^{2+} is added in this experiment in order to create a largest possible effect of Zn^{2+}, as the amount of zinc addition approaches the solubility of zinc acetate in primary water at 320 ºC.

The solution is deaerated by bubbling N_2 gas for a minimum of 12 hours before the experiment to keep a low concentration of O_2. The solution is then bubbled with forming gas (96% N_2 and 4% H_2 mixture) during the initial heating and during the experiment.

2.1.2 Electrochemical Cell Setup

2.1.2.1 Working Electrode

The Alloy 600 samples used during this project are part of commercial heats, provided by Dr. Peter Anderson from General Electric Global Research Center (GE-GRC).

The alloy samples are cut into rectangular pieces of around 0.7cm x 0.7cm x 0.08cm. Each sample is grinded with SiC sandpaper from 240 up to 1500 grit, and then polished using 6um and 1um diamond paste. The sample is then spot-welded to a 0.05mm-diameter Alloy 600 wire, which is then shielded with 0.66mm OD PTFE sleeve tubing and an outer ceramic tube insulator (0.156" OD, 0.052" IN).

2.1.2.2 Counter Electrode

The counter electrode is a 425 mg, 100 mesh platinum gauze (99.9% metal trace basis) spot-welded to a 0.05mm-diameter Pt wire (99.95% metal basis). The dimension of the gauze is 25mm x 25mm. The distance between the counter electrode and the sample is 16mm, and the distance between the counter electrode and the reference electrode is also 16mm.

2.1.2.3 Reference Electrode

A 0.05mm-diameter Pt wire (99.95% metal basis) is used as the reference electrode. Since forming gas (96%N_2, 4%H_2) is inserted into the solution, the reaction at the reference electrode at equilibrium is

$$2H^+ + 2e^- \rightarrow H_2 \qquad (1)$$

The equilibrium potential for the reference electrode is calculated using Nernst Equation:

$$\Delta\phi_e = \Delta\phi_e^o - \frac{RT}{zF}\ln\frac{f_{H_2}}{\left[H^+\right]^2} = \Delta\phi_e^o - \frac{2.303RT}{F}pH - \frac{RT}{2F}\ln f_{H_2} \qquad (2)$$

In which $\Delta\phi_e^o$ is the standard reduction potential ($\Delta\phi_e^o$ =0.0 V vs. SHE for this half-cell reaction at all temperature); R is the ideal gas constant; T is temperature; z is charge transfer number (z=2 in this reaction); F is Faraday's constant; f_{H2} is the fugacity of H_2; $[H^+]$ is the concentration of H^+ ($pH_{320°C}$ =7.28 at 320 ºC for the solution using the PWR-ELECTROCHEM code developed by Macdonald and Kim [30])

The fugacity of H_2 is calculated using temperature-dependent Henry's Law [30],

$$m_{H_2}^T = K_H^T f_{H_2}^T = K_H^{T_0} f_{H_2}^{T_0} \qquad (3)$$

Where $K_{H_2}^T$ is Henry's law constant in mol/kg-atm, $f_{H_2}^{T_0}$ is the fugacity of H_2 in the standard state, and $f_{H_2}^T$ is the temperature dependent fugacity. Henry's law constant for H_2 in water is given as

$$\log\left(K_{H_2}^T\right) = \frac{1321}{T} - 10.703 + 0.010468 \times T \quad (4)$$

The fugacity of H_2 at temperature T in the solution is calculated as

$$f_{H_2}^T = \frac{K_H^{T_0}}{K_H^T} f_{H_2}^{T_0} \approx \frac{K_H^{T_0}}{K_H^T} P_{H_2} \qquad (5)$$

Where P_{H_2} is the dissolved hydrogen gas pressure. The forming gas contains 4% H_2, so P_{H_2} is 0.04atm at room temperature. The fugacity of H_2 at 320℃ is 0.0055atm.

This yields an equilibrium potential of -0.723V $_{SHE}$.

$$\Delta\phi_{e\_320C} = -0.723V \; vs \; SHE \qquad (6)$$

2.1.2.4 Autoclave Assembly

All three electrodes are electrically connected to the potentiostat using 0.05mm wires attached to the electrodes, and all the connection wires are insulated with PFA Teflon. A double bore alumina rod separates the two electrodes inserted into one sample holder. The wires are sealed at the back of the sample holder using Conax fitting, with part of each wire outside the holder for electrical connection with the potentiostat. Figure 2-4 shows the locations of the electrodes in the autoclave after loading. Holes for heaters as well as for sealing the autoclave can also be seen.

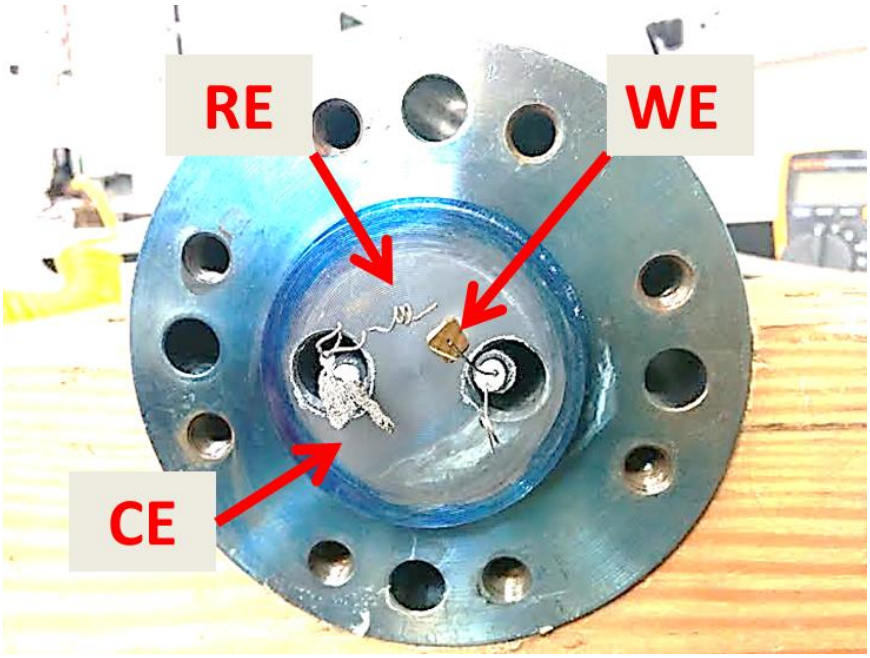

Figure 2-4: Sample location in the autoclave after loading

2.2 Experimental Procedure

2.2.1 Before Heating

Over 40 liters of solution (Zn free and Zn containing) is pre-mixed in the water tank using DI water and is deaerated for over 72hrs before transporting to the water column, where further deaeration and hydrogen dissolution is conducted for at least 8 hours before heating. Once the autoclave is assembled and connected to the water system, the flow is turned on for at least 15 min to remove residual oxygen in the system before heating.

2.2.2 Heatup

After the heaters are connected to the autoclave, and the whole autoclave body is insulated with glass wool and fire bricks, the autoclave is heated from room temperature to 320 ºC. In order to prevent too much pressure to the autoclave, temperature increases fast at low temperature and slows down as it approaches 320 ºC. The sample is cathodically polarized at -1.20V $_{REF}$ (-1.54V $_{SHE}$ at 20 ºC and -1.972V $_{SHE}$ at 320 ºC) during the 4-hr heating process in order to prevent oxide formation as well as to reduce the air-formed passive layer before the experiment. The buffered primary water solution is able to maintain the pH of the solution although hydrogen is generated during the heating process.

2.2.3 Electrochemical Tests

A Gamry potentiostat (PCI4-750) is used for the electrochemical tests. After the temperature stabilizes, the sample is polarized at various potentials (-743 mV $_{SHE}$, -723 mV $_{SHE}$, -673 mV $_{SHE}$, -623 mV $_{SHE}$, -573 mV $_{SHE}$, -523 mV $_{SHE}$, -423 mV $_{SHE}$, -323 mV $_{SHE,}$ -223 mV $_{SHE}$) for 4hrs at each potential before electrochemical impedance spectroscopy (EIS) is conducted at these potentials. The long-time polarization is necessary so that the film growth reaches a steady state during the EIS measurement. The steady state is confirmed conducting Kramers-Kronig transformation at each potential. Each EIS measurement is conducted at frequency ranging from 50 kHz to 3 mHz.

EIS is a useful *in-situ* electrochemical method to study the electrochemical system, because different reaction steps dominate different frequency ranges. At high frequencies (f>300Hz), the impedance reveals the quick response from the oxide, whereas low frequency impedance shows response from double layer, Faraday process and mass transport [31], [32]. The capacitive behaviors could overlap in frequency, making it difficult to differentiate them from the raw data obtained. With equivalent circuit and kinetic modelling, kinetic parameters for reactions can be extrapolated to understand the electrochemical system.

2.2.4 Cooldown

The samples are cooled at a rate of 2 ºC/min. After the sample is cooled to room temperature, it is removed from the autoclave, rinsed with water and stored in the dry box. No further protection is made because Feng and Devine found that the oxide formed on Ni-based alloys at high temperature does not change during cooling process as well as after being exposed to air [21].

2.2.5 Film Characterization Experiments

Several samples oxidized at various potentials (-700 mV $_{SHE}$, -550 mV $_{SHE}$ and -223 mV $_{SHE}$) are examined by TEM microscopy to study the oxide structure and composition. This part of the experiment is conducted at NCEM of Lawrence Berkeley National Lab. The morphology of the samples are examined using FEI Strata 235 dual beam Focused Ion Beam (FIB) before they are milled using focused Ga^{+} ion beam to prepare cross-section samples. Pt is deposited for sample protection before each TEM lift-out sample is prepared with the Omniprobe system. The TEM samples are initially thinned using FIB, and further milled using NanoMill TEM Sample Preparation System (Model 1040). The FEI TitanX 60-300 microscope is used to conduct EDS analysis on the oxide films to investigate the chemical composition. The experiments are all conducted at 200kV.

Chapter 3. Characterization of the Passive Film

3.1 Introduction

The chemistry of the passive layer formed on Alloy 600 under different conditions has been investigated by various investigators. Microscopy is found to be one of the most efficient methodologies to study the structure and chemistry of the film. As is described in the introduction, the passive film on Alloy 600 generally consists of a Cr-rich inner compact layer and a Fe/Ni-rich outer layer. The inner layer is formed by ion migration and oxidation at the metal/film interface, whereas the outer layer is formed through dissolution/precipitation process [17], [20], [22], [23], [25]. This chapter will describe the microscopic structure of the passive layer formed at different conditions, i.e. potentials and water chemistry, and will discuss the possible film formation process.

The experiments were conducted using the lab-constructed system, polarizing the samples at different potentials for at least 4 hrs. The final potentials for the samples tests were found to be -700 mV $_{SHE}$,-500 mV $_{SHE,}$ and -223 mV $_{SHE}$.

3.2 Effect of Potential on Passive Film Formation in Zn Free Solution

3.2.1 Structure of Passive Film Formed in Zn free solution

Figure 3-1 shows the top-down morphology of the Alloy 600 surface formed at -700 mV $_{SHE}$ in Zn free solution at 320 ºC. It is observed that the surface is covered with whiskers averaging about 25-nm wide and 2-5-μm long, below which are sparsely distributed particles about 25-30 nm in diameter. Whiskers have been reported by Mintz et al. [33] to grow on Alloy 600 under high potentials in PWR primary water, and the whiskers were identified as NiO nanowires. Both the whiskers and particles shown can be related with the outer layer of the passive film given the non-compact nature of the morphology. The cross sectional TEM results are more informative about the difference between the inner layer and outer layer, as shown in Figure 3-2. It can be seen from the figure that the outer layer is not uniform in thickness or orientation. There is a large cluster of particles in the middle with irregular shape, likely formed by whiskers with different orientations shown in the SEM image, but damaged and deformed during the FIBing process. The identity of the cluster will be identified using EDS. Discrete small particles/nodules are also observed on the surface, ranging between 20-50 nm in diameter. These nodules may be associated with either whiskers or particles observed in the SEM image. The underneath more continuous layer can be defined as the compact inner passive layer.

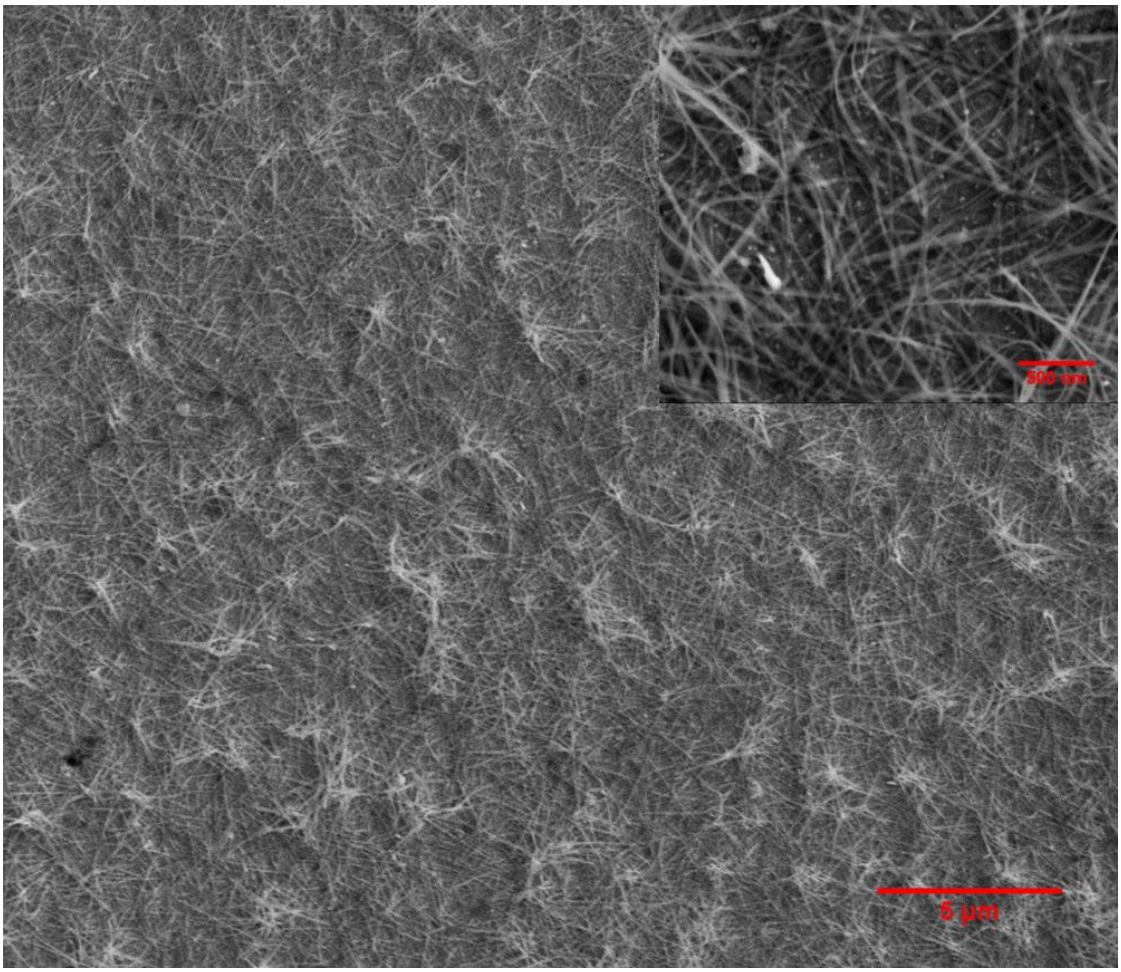

Figure 3-1: SEM view of the oxide film formed at -700 mV $_{SHE}$ at 320 °C in PWR simulated primary water, showing whisker shape oxides on top and small particles below whiskers.

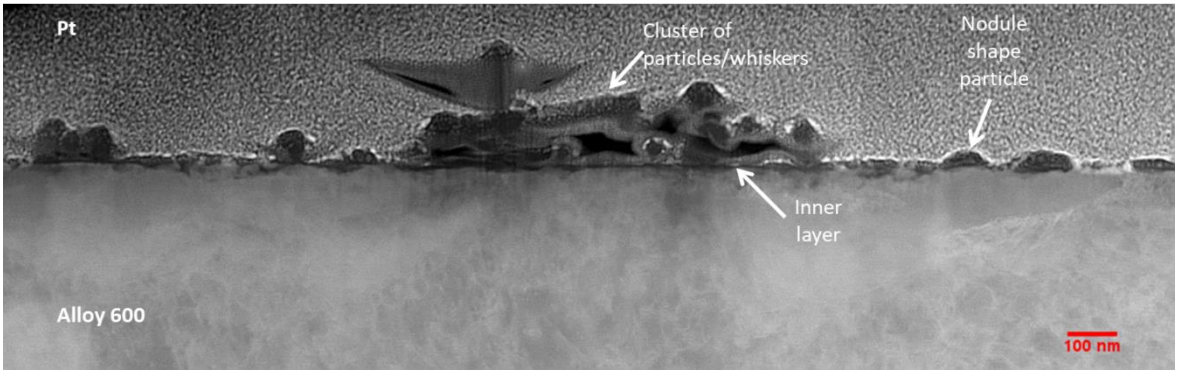

Figure 3-2: TEM cross-section of the oxide film formed at -700 mV $_{SHE}$. In the image, the lower part is the Alloy 600 matrix, whereas the upper part is the deposited Pt layer.

Figure 3-3 shows the SEM image of the Alloy 600 surface oxidized at -550 mV $_{SHE}$. Similar to what is shown on Alloy 600 at -700 mV $_{SHE}$, whiskers are observed on top of the surface. The density of the whiskers is larger than what was observed at lower potential, indicating that more whiskers grow at this potential. The diameters of the whiskers average around 25nm, which is

consistent with what is observed at lower potential. Because the whiskers are more densely packed, the distribution of any particles underneath whiskers cannot be determined from the SEM image. However, from the particles detected, diameters of the particles average around 50 nm, approximately twice as large as what was observed at lower potentials. Some 500-nm crystalized particles are also observed in the low magnification image lying on top of the whiskers, and these particles are likely the product of precipitation of aqueous ions in the autoclave, as is described by Huang et al. [34]. Huang suggested that this precipitation will not strongly affect the growth of oxide film, so these particles will not be discussed in the following texts.

The cross-sectional TEM image is presented in Figure 3-4. It can be seen that there are three different types of particles/films present on the Alloy 600 surface, elongated particles with average length of 150 nm, and discrete nodule shape particle that range between 40-70 nm in diameter. The elongated particles are associated with randomly oriented whiskers that were intercepted by the plane of observation of the photograph. The discrete nodule shape particles correspond to the particles with similar sizes observed underneath the whiskers in the SEM image and those observed in -700 mV $_{SHE}$ image. These particles do not undergo significant growth in size with potentials.

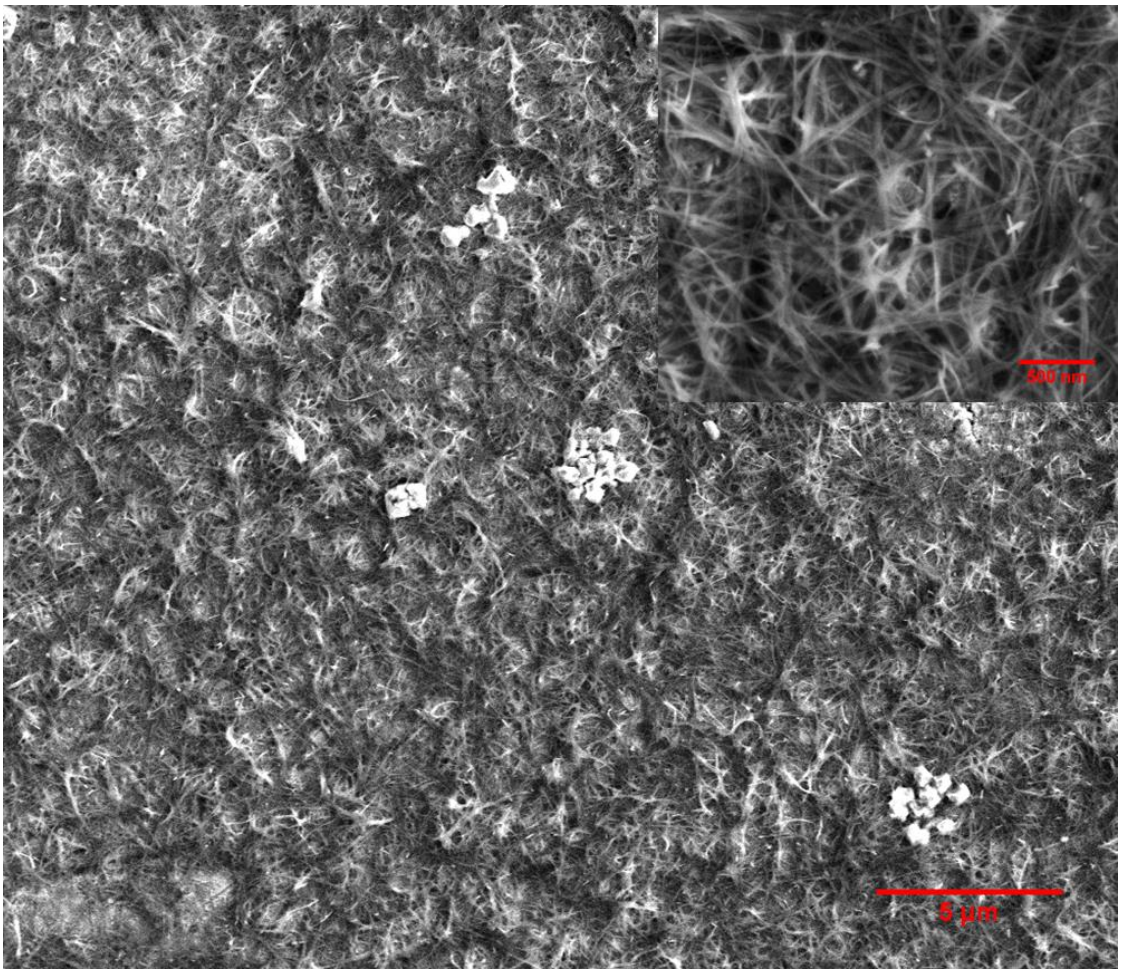

Figure 3-3: SEM view of the oxide film formed at -550 mV $_{SHE}$ at 320 °C in PWR simulated primary water, showing whisker shape oxides on top and small particles below whiskers.

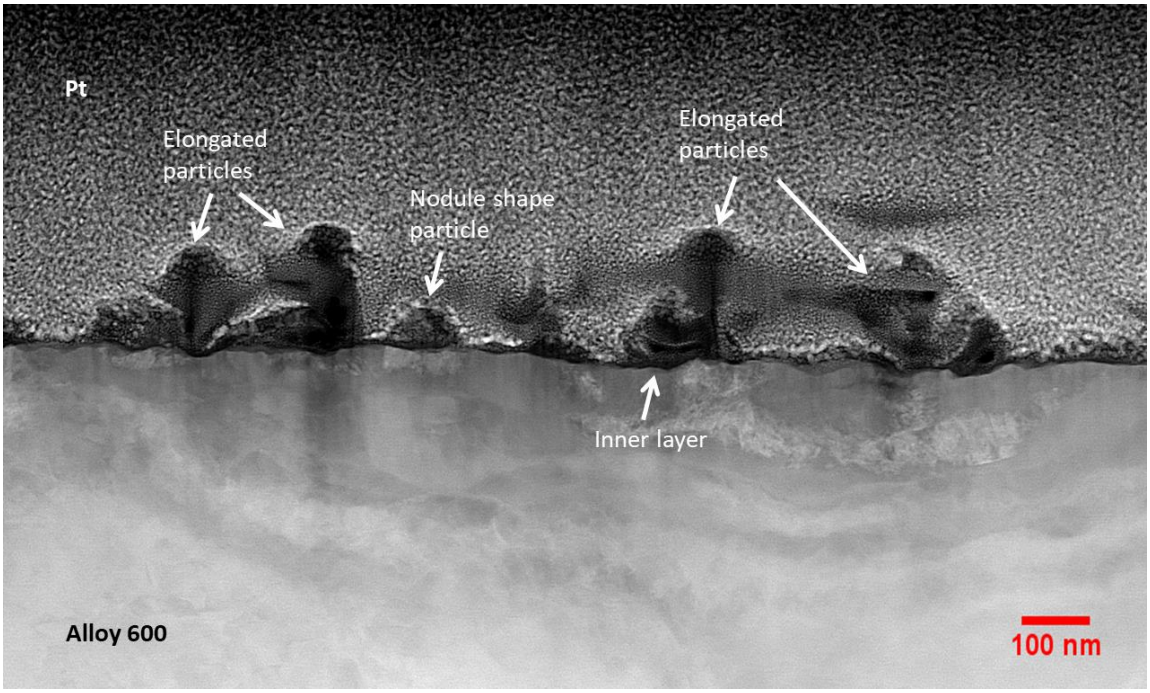

Figure 3-4: TEM cross-section of the oxide film formed at -550 mV $_{SHE}$. In the image, the lower part is the Alloy 600 matrix, whereas the upper part is the deposited Pt layer.

The top-down image of the Alloy 600 surface oxidized at -223 mV $_{SHE}$ is shown in Figure 3-5. The surface exhibits a very different morphology than the surfaces oxidized at lower potentials. Instead of whiskers growing on the whole surface, needle-shape oxides only cover part of the metal surface. The overall film is largely diminished given the fact that some scratches are detectable in the SEM picture. In the high-mag image, both needle-shape oxides and small discrete particles are observed. The diameters of the needle-shape particles vary between 35 nm to 65 nm, whereas the diameters of the particles average around 50 nm. Although the sizes of the particles do not change from those formed at lower potentials, the morphology change of oxides may be associated with a composition change at higher potentials, and this possibility is investigated by EDS and the results are presented later in the chapter. The cross-sectional TEM results of the film also indicate a difference in the oxide structure, as is shown in Figure 3-6. Compared with the passive films formed at lower potentials, the passive film formed at -223 mV $_{SHE}$ is absent of particles of irregular shape, but has a semi-continuous outer layer with non-uniform thickness ranging between 16 nm and 75 nm. Particles observed in the SEM image are not observed in this TEM cross-section, but may be present in other regions.

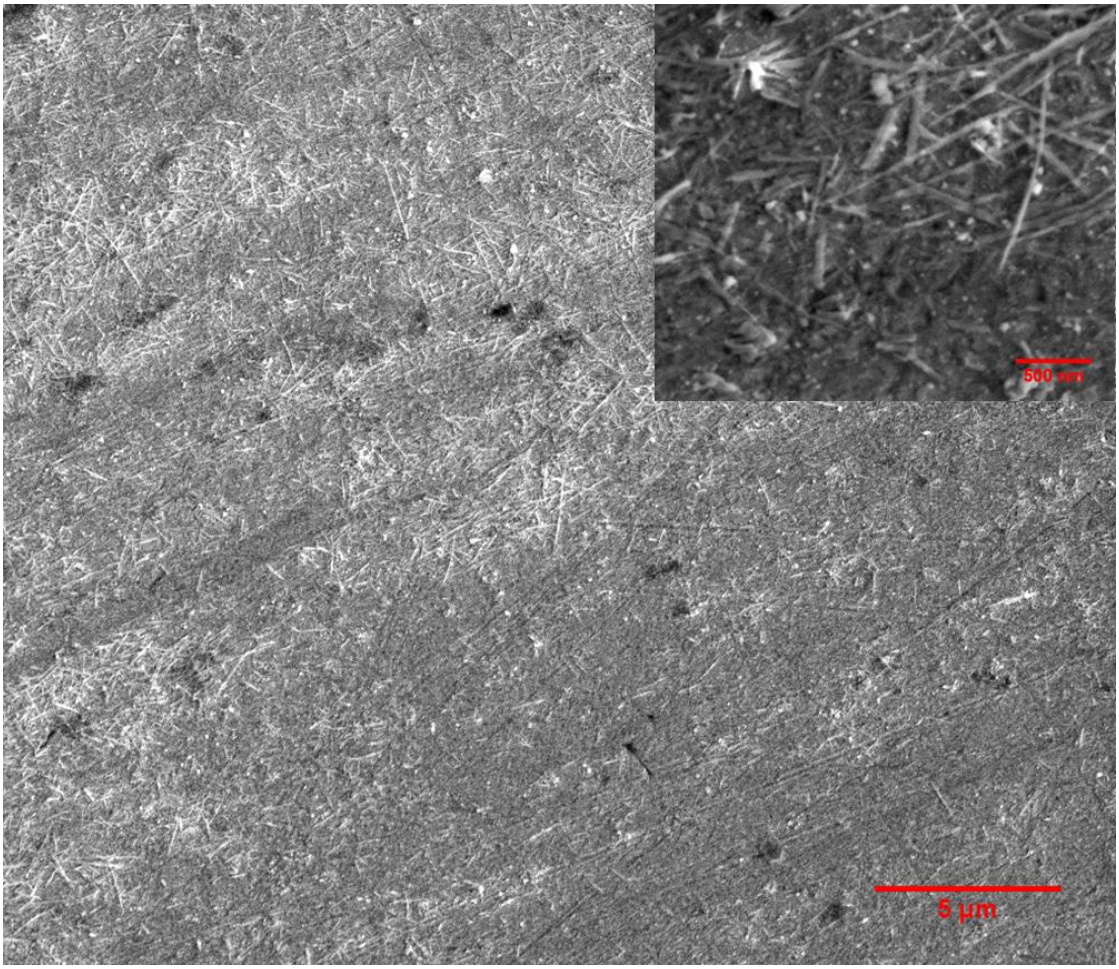

Figure 3-5: SEM view of the oxide film formed at -223 mV $_{SHE}$ at 320 °C in PWR simulated primary water, showing needle- shape oxides and small particles.

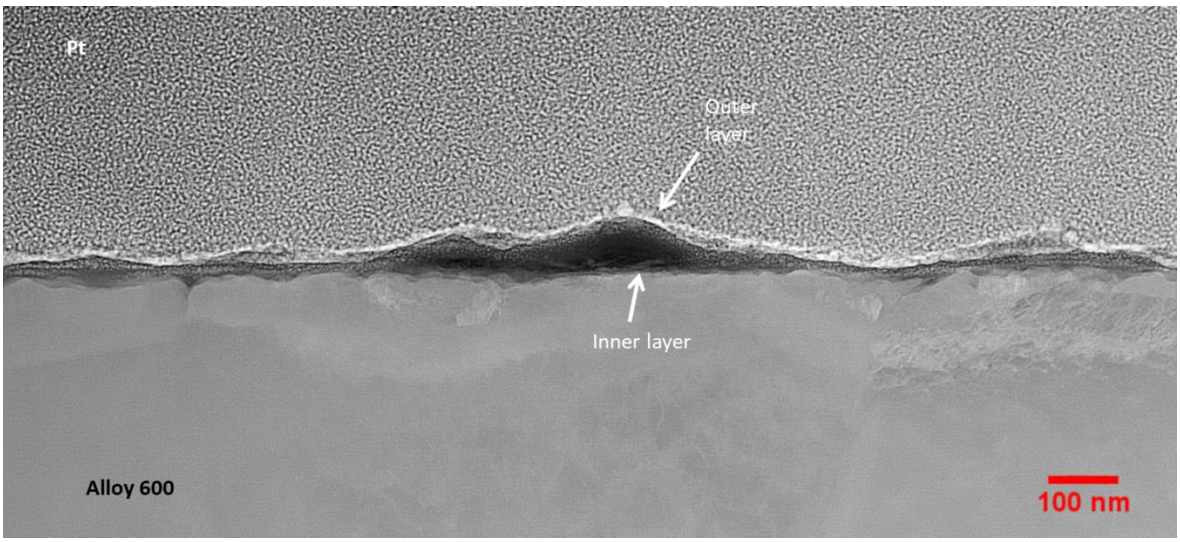

Figure 3-6: TEM cross-section of the oxide film formed at -223 mV $_{SHE}$. In the image, the lower part is the Alloy 600 matrix, whereas the upper part is the deposited Pt layer.

Both the SEM and cross sectional TEM images of the oxide layer shown above indicate that despite the change in outer layer structure with potential, the inner layer remains continuous. The thickness of the inner layer will be measured and discussed in the following texts.

3.2.2 Composition of Passive Layer formed on Alloy 600 in Primary Water

The variations in the composition of films oxidized at different potentials will be discussed in this section. Besides the EDX mapping for different elements, the mass fraction (wt%) of Ni, Cr, Fe, as well as signal counts (%) of O are plotted versus distance from the outer surface. The mass fraction of the metals is balanced with Pt, which is deposited above the sample during the FIB process.

The EDX mapping of the cross-section of the passive film formed at -700 mV $_{SHE}$ is shown in Figure 3-7, in which the shape of the oxides and comparative composition can be identified clearly. The clusters of particles located in the upper half of Figure 3-7 (a) are preliminary segments of whiskers intercepted by the plane of cross section. Besides the possibility of being the particles observed underneath the whiskers in Figure 3-1, the nodule shape particles shown in the TEM picture might also be whiskers oriented such that the axis is perpendicular to the viewing plane. It is hard to distinguish between the discrete particles and whiskers whose axis is perpendicular to the plane of observation, because both features have similar diameters between 20 nm and35 nm. Both the features are referred to as outer layer. It is found through EDS elemental mapping that the outer layer particles are rich in Ni and Fe. The results also indicate that the inner layer of the passive film is rich in Cr and is continuous on the metal surface. With the oxygen map, the inner layer thickness is measured to be on average 10 nm. The location of the interface between the alloy and the inner layer indicates that the inner layer grows predominantly at the alloy/oxide interface; that is, the inner layer grows into the alloy. The change in color intensity for Cr at the interface between the alloy and the inner layer shows a non-continuous Cr-depleted region, which can be caused by selective dissolution of Cr into the oxide.

(a)

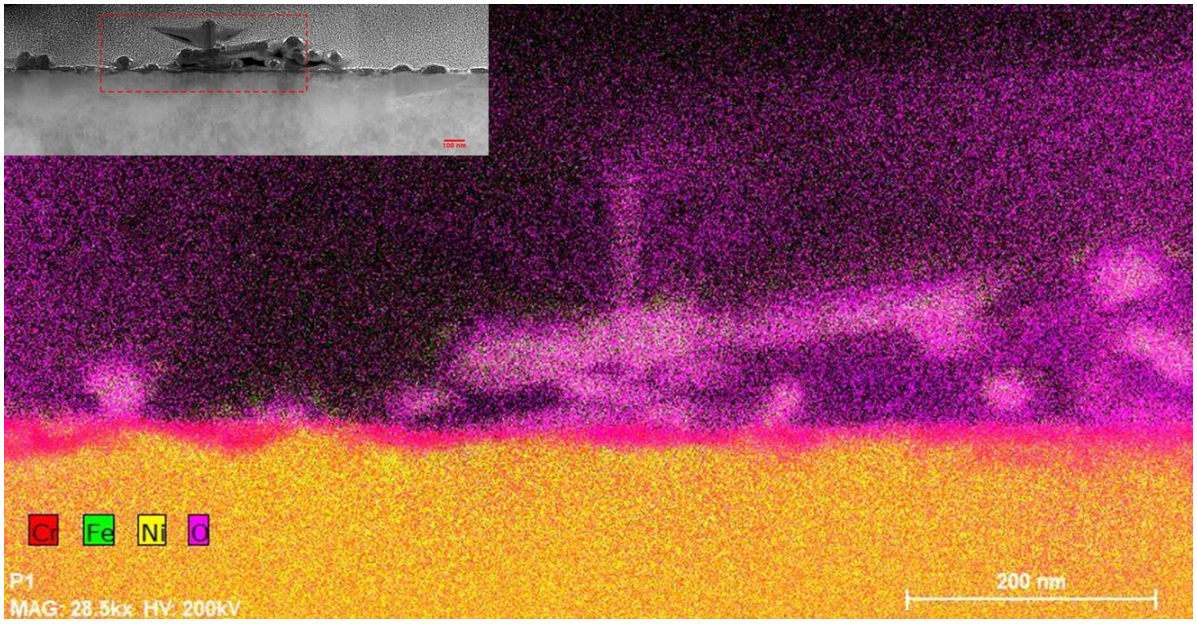

(b)

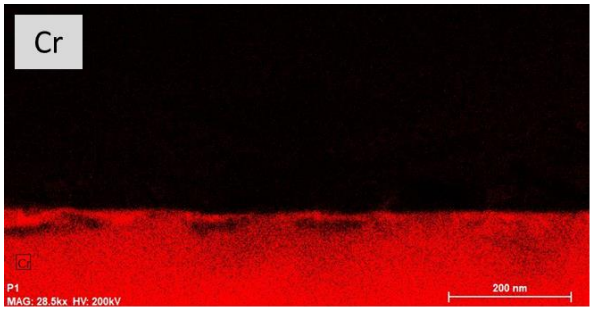

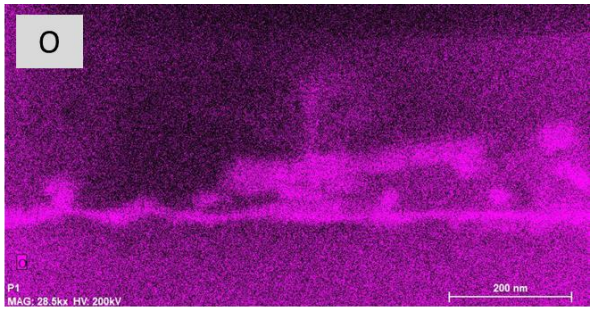

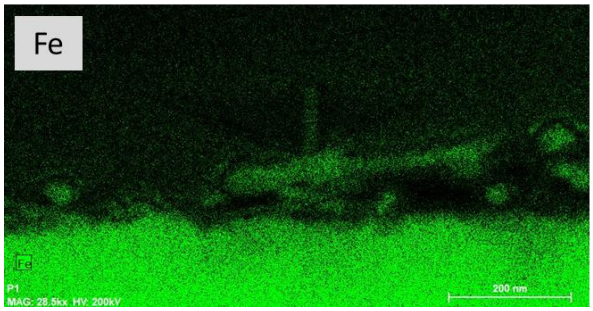

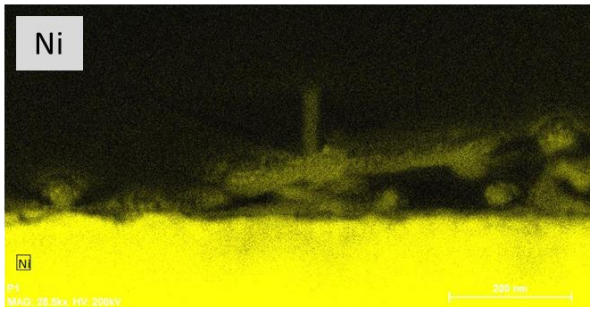

Figure 3-7: EDX mapping of the passive film formed at -700 mV $_{SHE}$ in Zn free primary water. (a) overlaying elemental map. (b) individual elemental maps for Cr, O, Fe, Ni.

Three compositional line scans perpendicular to the alloy/oxide interface are shown in Figure 3-8. Due to the fact that outer layer particles are discrete and are varying in size and shape, signals of Fe, Ni, Cr and Pt are measured to calculate the mass fraction. The mass fraction of Pt is balanced with other elements and not shown in the figures. Since the energy for oxygen scattering is too low that it is hard to measure oxygen concentration accurately, only the relative oxygen signal counts (%) is presented. Information about where the oxides would grow and changes in sample thickness is obtainable from the oxygen scan.

The results in Figure 3-8(b) of line scan #1 indicate that there are stacked outer layer particles (or whiskers) with discrete edges, and the particles are rich in Ni and Fe. These particles contain Ni and Fe with a ratio of between 4:1 and 5:1. The spatial variations of Ni along the line scan almost parallel that of Fe and O, which suggests that these signal variations are caused by spatial variations along the line scan in the size of excited volume for particle/whisker, rather than compositional variation within the oxides. The high value of Ni to Fe ratio suggests that the oxide consist mostly of NiO and a small amount of Fe_xO_y and/or $NiFe_2O_4$. Thermodynamic calculation from Kaufman [35] indicates that there is no Fe^{3+} formed at potential below -500 mV $_{SHE}$ but $FeCr_2O_4$, as is shown in Figure 4-2. Since no Cr is found in the outer layer, the presence of Fe should be attributed to substitution of Ni^{2+} in the NiO phase, as $(Ni_xFe_{1-x})O$. Ignoring the fluctuations that are attributed to fluctuation of the excited volume size during analysis, the relative constant composition of Fe, Ni and O with distance indicates that ion transport in the oxide is rapid and is not the rate determining step in the growth of the outer layer. The EDS results indicate that there is a high concentration of Cr in the inner layer, but the presence of Ni and Fe is not very clear. The line scan shows an increasing concentration of Ni in the inner layer, but the Ni signal might actually come from the alloy rather than from the inner layer. The scanning volume of the electron beam may be larger than the thickness of the inner that the signal overlaps with the alloy matrix or the outer layer. Another cause of Ni uncertainty is the possibility that the normal of the metal/film interface is not perpendicular to the incident electron beam. With a rough calculation comparing the ratio of Ni, Cr and Fe in the alloy matrix with that in the inner layer, it is indicated that the inner layer contains a mixture of Cr_2O_3 and very limited amount of $FeCr_2O_4$. The reason for large Ni content is found to be the electron beam overlapping with outer layer or matrix.

Figure 3-8 (c) presents the spectra of outer layer and of the thin inner layer along line scan #2. It is worth noting that the outer layer particles at distances of 100-210 nm from the inner layer exhibit low oxygen signal, as well as slightly lower values for Ni, Cr and Fe. The low signal in this region is likely due to the reduction in sample thickness or the thinness of the particle compared to the overall thickness of the sample. A similar Ni to Fe ratio of 4-5:1 is observed in the outer layer, which suggests that the particles/whiskers in line scan #2 are dominated by NiO with some Fe-rich spinel. The 12-nm Cr-rich inner layer is found to contain a Ni-to-Cr ratio close to 1:1, indicating a layer composed of Cr_2O_3 with very limited amount of $NiCr_2O_4$ after metal deconvolution.

The path of line scan #3 does not intercept outer layer particles/ whiskers. The composition along scan # 3 is presented in Figure 3-8 (d). The results indicate the inner layer is Cr-rich and approximately 10 nm. It is also suggested that after the deconvolution of matrix Ni/Fe signal in the inner layer, the inner layer is mostly composed of Cr_2O_3, some fluctuation with distance in the inner layer indicates a possible composition of Cr-rich spinel that contains Ni and Fe with similar ratio to the metal matrix.

A 20-nm thick Cr-depleted/ Ni-enriched zone in the alloy beneath the inner layer is present in both line scans #2 and #3, but not in line scan #1. The results suggest that the Cr depleted/ Ni enriched zone is not continuous along the alloy surface. Similar phenomenon is also reported by Panter et al. [18] and this is caused by selective dissolution of Cr and reduction of Ni.

(a)

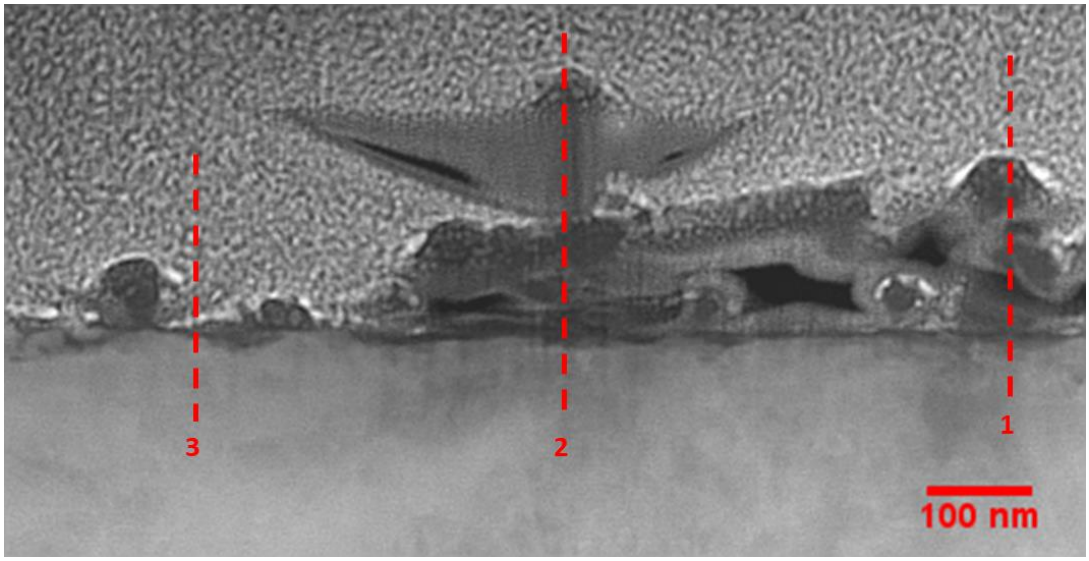
3
2
1
100 nm

(b)

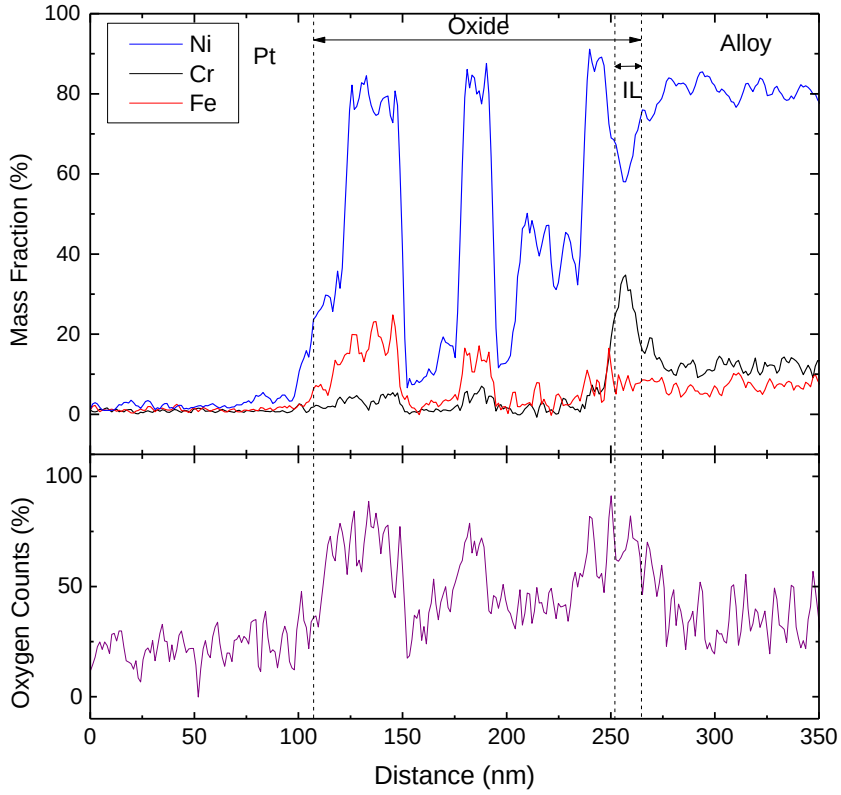
Ni
Cr
Fe
Pt
Oxide
IL
Alloy
Mass Fraction (%)
Oxygen Counts (%)
Distance (nm)
0
20
40
60
80
100
0
50
100
150
200
250
300
350

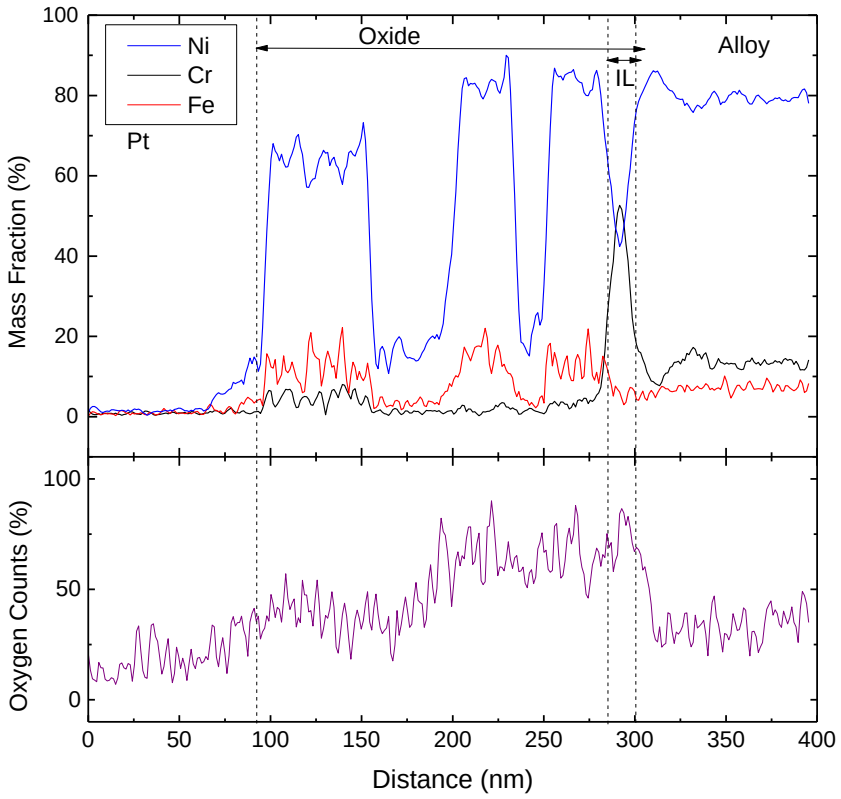
Ni
Cr
Fe
Pt
Oxide
IL
Alloy
Mass Fraction (%)
Oxygen Counts (%)
Distance (nm)
0
20
40
60
80
100
0
50
100
150
200
250
300
350
400

(c)

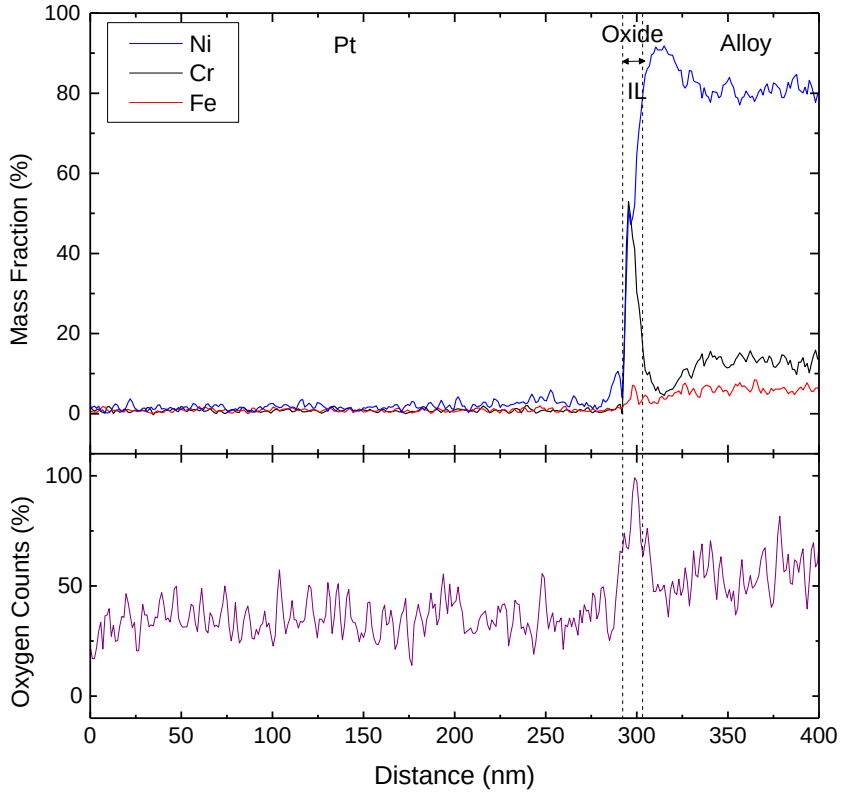

(d)

Figure 3-8: Line scan on different regions of Alloy 600 passive layer oxidized at -700 mV $_{SHE}$ in Zn free primary water. (a) TEM image showing regions of line scans. (b) Line scan of region 1 showing outer layer particles stacking porously and inner layer. (c) Line scan of region 2 showing different orientations of outer layer particles and inner layer. (d) Line scan of region 3 showing some outer layer parts and mostly inner layer.

The oxide film formed at -550 mV $_{SHE}$ is analyzed through EDX and the results are presented in Figure 3-9, in which both the overlaid mapping results and the individual elemental mappings are included. Similar to the mapping results shown in Figure 3-7, the outer layer particles of irregular shapes observed in the cross-sectional TEM represent particles or portions of whiskers of intercepted by the plane of observation. The outer layer is found to be rich in Ni and Fe. The Cr map indicates the inner layer is Cr rich with an average thickness of 8-11nm.

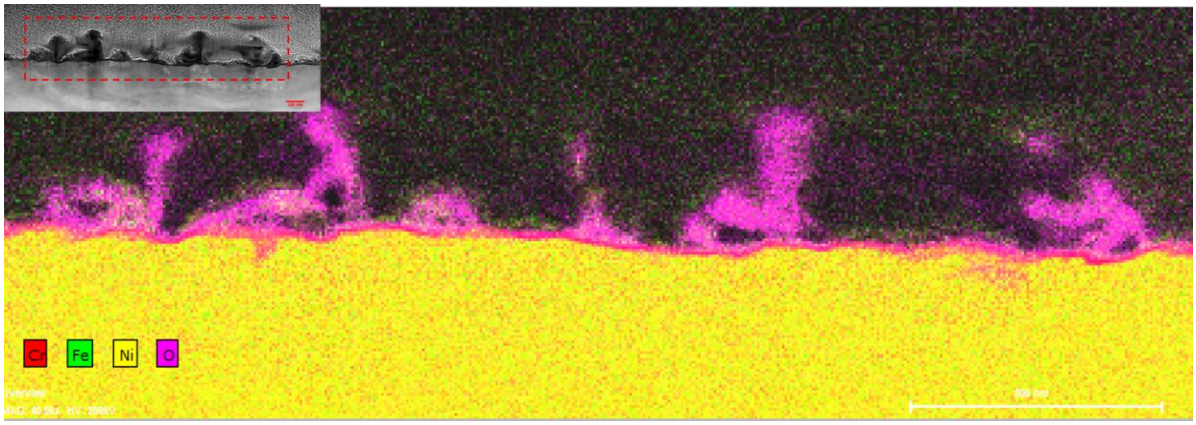

(a)

(b)

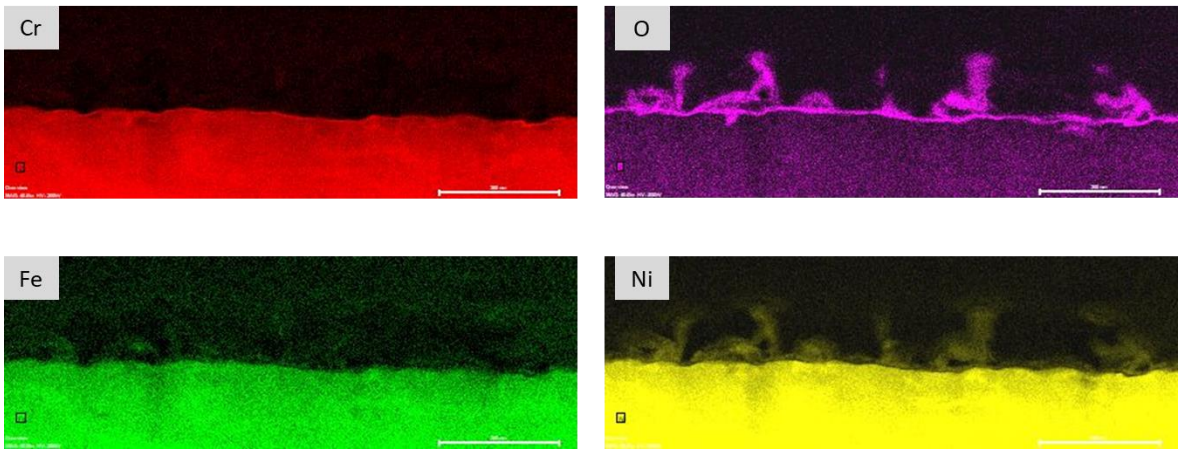

Figure 3-9: EDX mapping of the passive film formed at -550 mV $_{SHE}$ in Zn free primary water. (a) overlaying elemental map. (b) individual elemental maps for Cr, O, Fe, Ni.

EDX compositional analyses along three line scans are presented in Figure 3-10. Figure 3-10 (a) shows the locations of the three line scans perpendicular to the alloy/film interface. Line scan # 1 presented in Figure 3-10 (b) shows the composition of the outer layer and the inner layer. The outer layer is found to contain almost 90% of Ni, with a Ni:Fe composition ratio between 8:1 and 11:1, and the composition can be identified as mostly NiO and very few $(Ni_xFe_{1-x})O$. The inner layer is found to have a large signal of Cr, and the thickness is found to be 9 nm. After the deconvolution of the Alloy 600 matrix, the inner layer consists of Cr_2O_3. Figure 3-10 (c) presents the EDS along line scan #2 that contains mostly inner layer. The 9-nm inner layer is found to contain Cr_2O_3 and $FeCr_2O_4$ after accommodating for the alloy in contribution to the measured counts. Line scan #3 presented in Figure 3-10 (d) indicates that the outer layer particle contains a large concentration of Ni and a small concentration of Fe, and has a similar Ni/Fe ratio to the particle measured by line scan #1. The outer layer of line scan #3 therefore can be NiO with $(Ni_xFe_{1-x})O$. The inner layer is 7.5 nm thick, and consists of Cr_2O_3 and $FeCr_2O_4$. Unlike the EDX results at lower potentials, Cr depleted zone is not found in the alloy oxidized at -550 mV $_{SHE}$.

(a)

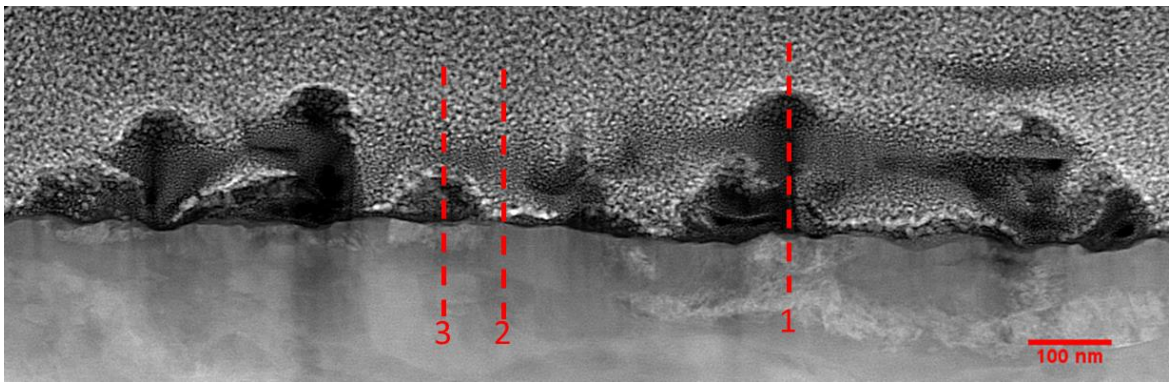

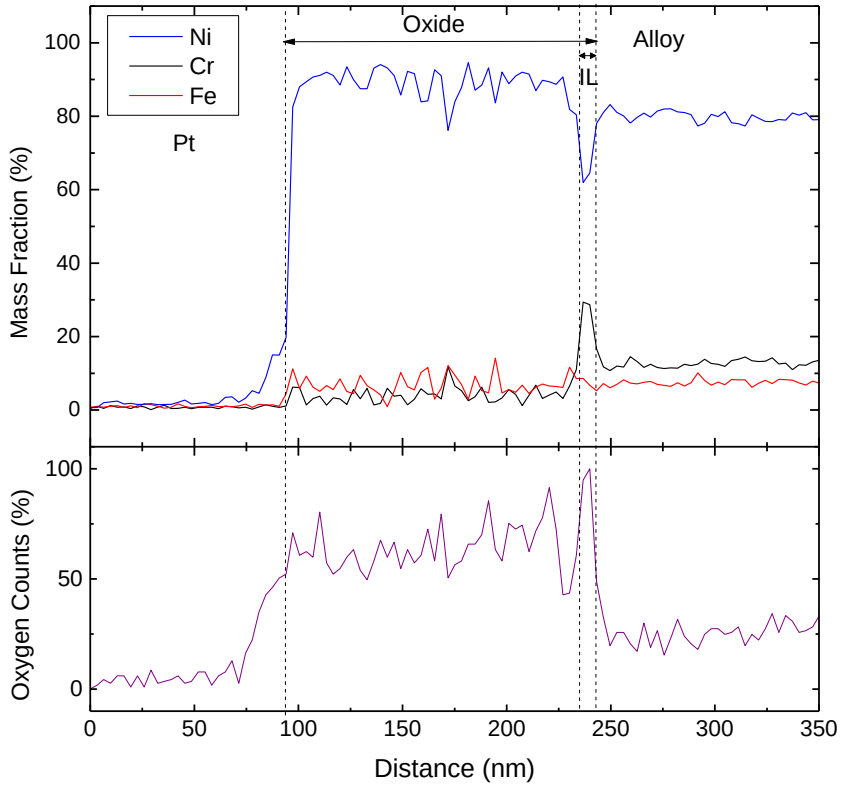
Ni
Cr
Fe
Pt
Oxide
IL
Alloy
Mass Fraction (%)
Oxygen Counts (%)
Distance (nm)
0
20
40
60
80
100
0
50
100
0
50
100
150
200
250
300
350

(b)

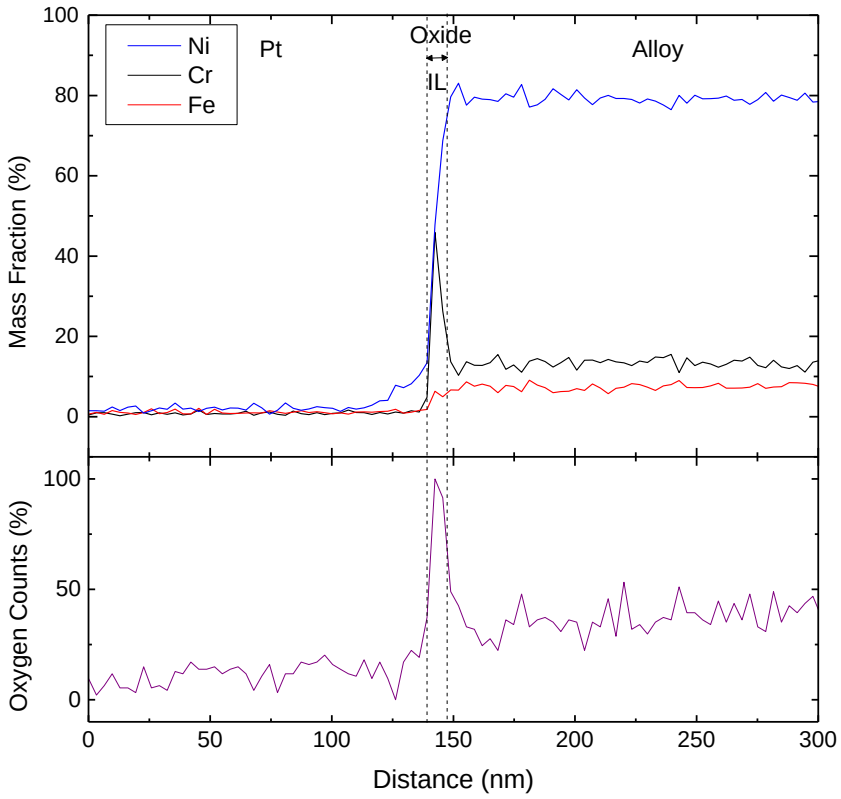
Ni
Cr
Fe
Pt
Oxide
IL
Alloy
Mass Fraction (%)
Oxygen Counts (%)
Distance (nm)
0
20
40
60
80
100
0
50
100
150
200
250
300

(c)

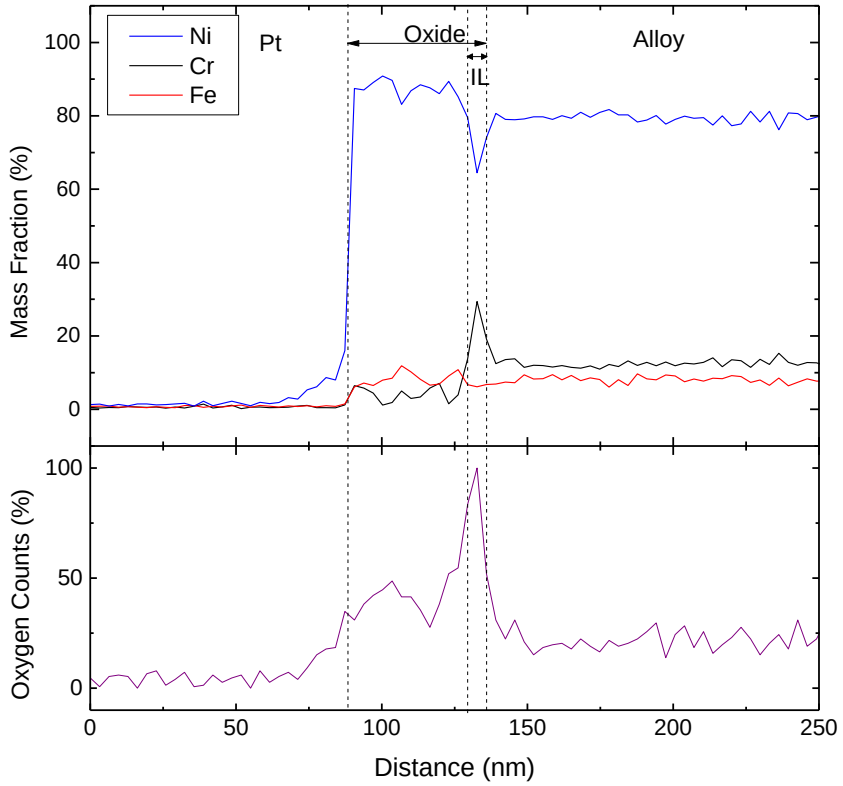

(d)

Figure 3-10: Line scan on different regions of Alloy 600 passive layer oxidized at -550 mV $_{SHE}$ in Zn free primary water. (a) TEM image showing regions of line scans. (b) Line scan of region 1 showing different orientations of outer layer particles and inner layer. (c) Line scan of region 2 showing mostly inner layer. (d) Line scan of region 3 showing porous outer layer particles and inner layer.

Figure 3-11 illustrates the mapping results of the surface oxidized at -223 mV $_{SHE}$. The film is composed of a Ni/Fe-rich outer layer and a Cr-rich inner layer. However, rather than porous particles as observed at lower potentials, the Ni/Fe rich layer is comparatively compact, and has a large contact area with the inner layer. The inner layer is a continuous Cr-rich film, and is measured to be around 11nm using the oxygen map. Comparing the metals and oxygen elemental maps, it is suggested that there are some extra oxide particles, and the composition of the oxides will be discussed below.

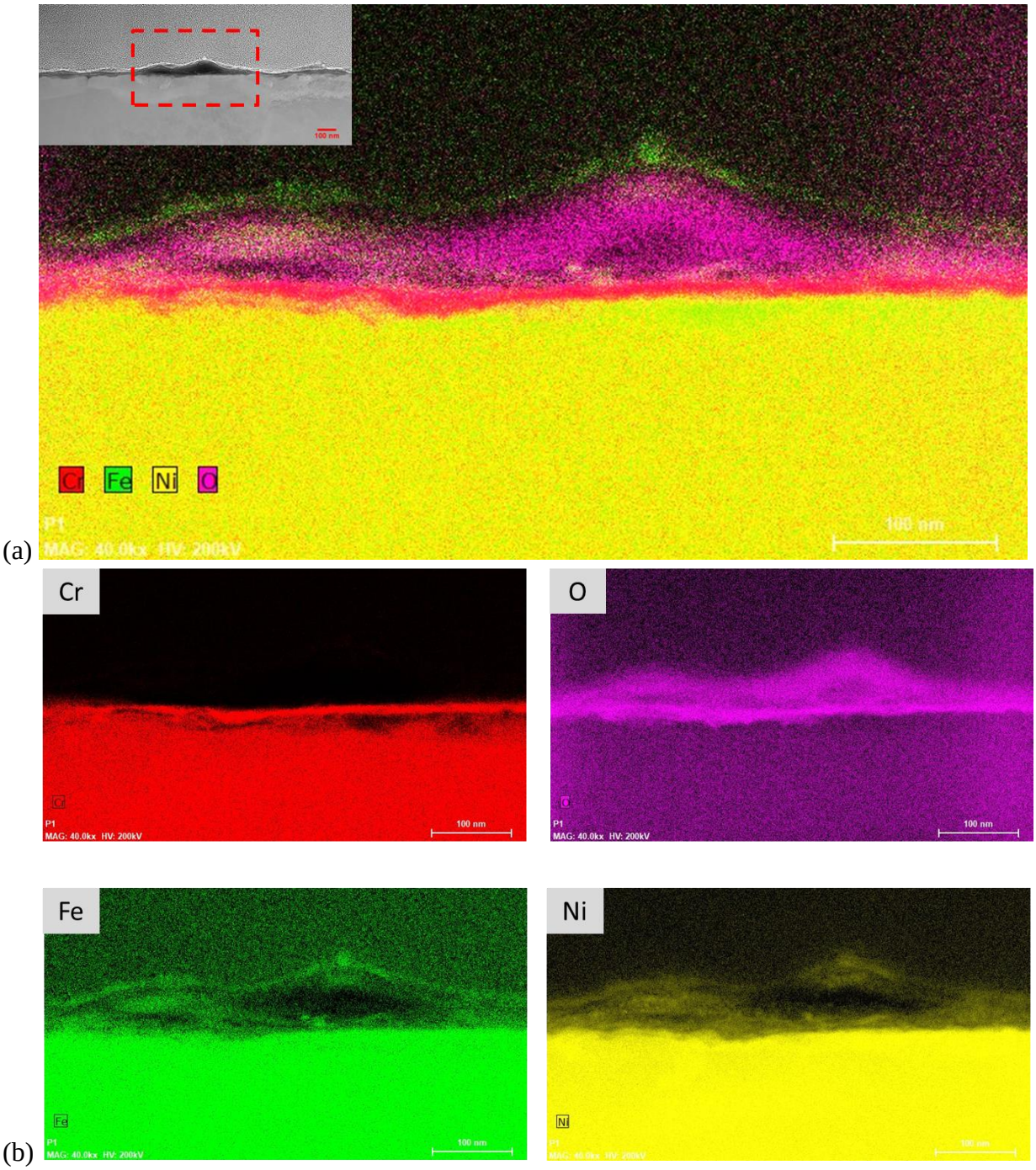

Figure 3-11: EDX mapping of the passive film formed at -223 mV $_{SHE}$ in Zn free primary water. (a) overlaying elemental map. (b) individual elemental maps for Cr, O, Fe, Ni.

Figure 3-12 shows the compositional analyses along two line scans of Alloy 600 oxidized at -223 mV $_{SHE}$, in which Figure 3-12 (a) shows the locations of the line scans. In Figure 3-12 (b), the outer layer is approximately 25nm thick, and composition gradient is observed in the outer layer. The outer part of the outer layer contains 80% Ni, 10%Cr and 10%Fe, whereas the inner layer contains 70%Ni and 20%Cr. Kaufman's thermodynamic calculation predicts that Fe is

only stable in the form of ferrite spinel, so all Fe found at this potential is attributed to MFe_2O_4. Regardless of the composition gradient, it can be concluded that the outer layer consists of NiO with $Ni(Cr_xFe_{1-x})_2O_4$. The change in composition gradient is due to formation of $NiCr_2O_4$. The 9nm thick inner layer is with Cr_2O_3 after deconvolution of metal matrix. It is noted that there is a 40nm thick Cr depletion region in the alloy underneath the inner layer, which can be related to the selective dissolution in the alloy. Figure 3-12 (c) indicates an outer layer that contains two parts of different compositions, a 35-nm-thick region rich in Ni/Fe and a 30-nm-thick area rich in Ni. The Ni/Fe rich part is composed of NiO and $Ni(Cr_yFe_{1-y})_2O_4$ with composition variance along the line scan direction. At the interface between Ni-rich outer layer and Ni/Fe-rich outer layer, high content of Fe and Cr is found, indicating formation of more $NiFe_2O_4$ and $NiCr_2O_4$. The Ni-rich outer layer part contains mostly NiO and small amount of Fe-rich spinel. The inner layer is 10-nm thick and consists of Cr_2O_3 and $NiCr_2O_4$ after the contribution of the alloy to the measured signal. A 25-nm thick Cr depleted zone below the alloy/film interface is also found in this line scan.

(a) 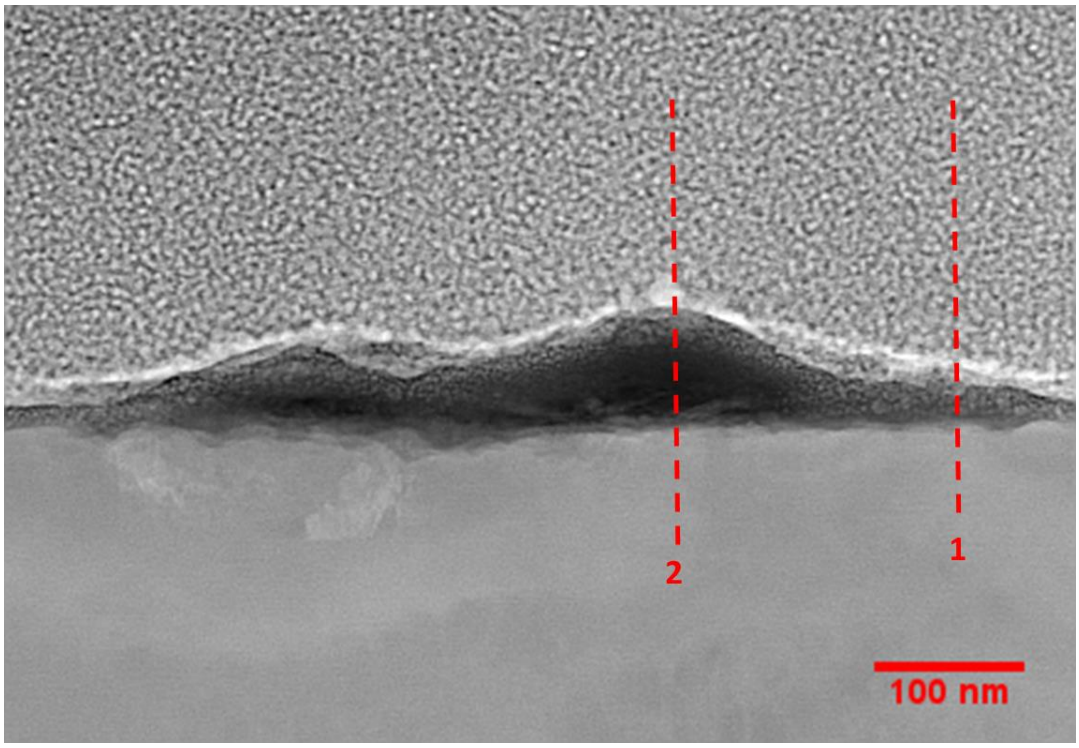

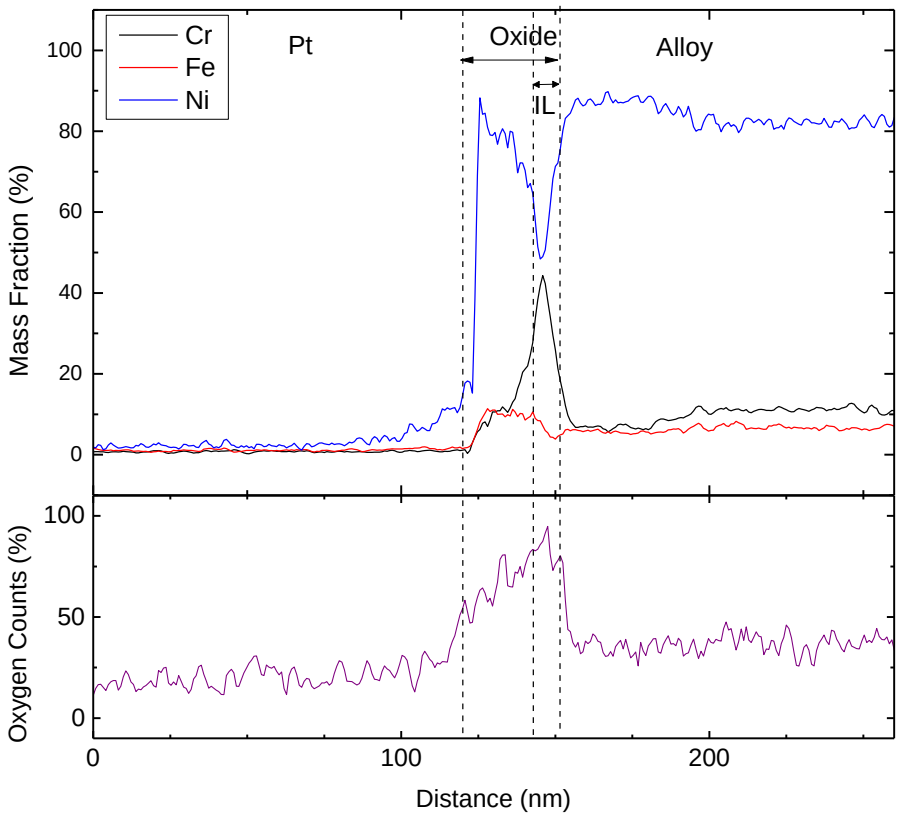
Cr
Fe
Ni
Pt
Oxide
IL
Alloy
Mass Fraction (%)
Oxygen Counts (%)
Distance (nm)
0
20
40
60
80
100
0
50
100
0
100
200

(b)

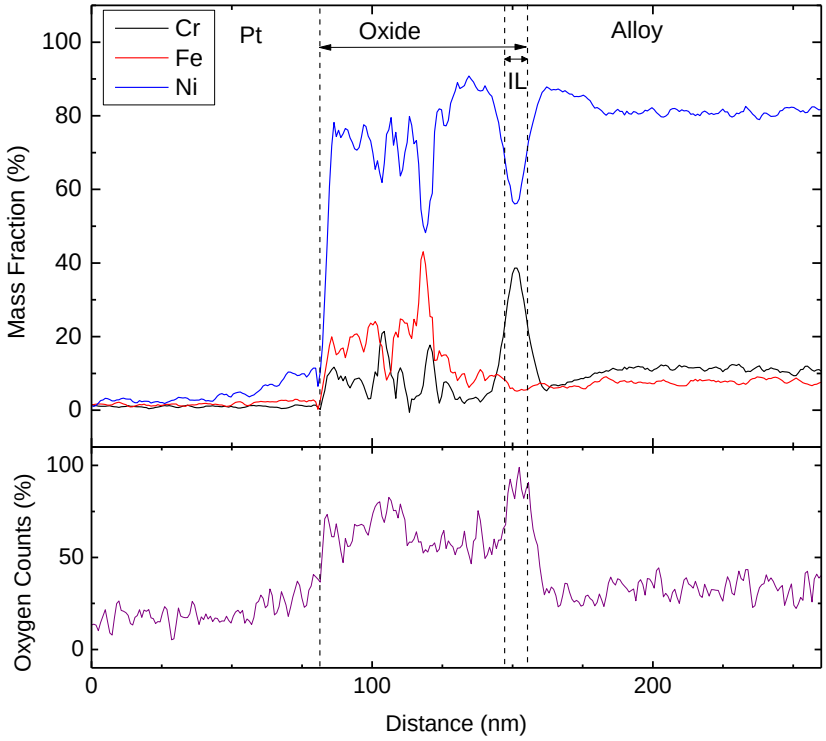

(c)

Figure 3-12: Line scan on different regions of Alloy 600 passive layer oxidized at -223 mV $_{SHE}$ in Zn free primary water. (a) TEM image showing regions of line scans. (b) Line scan of region 1 showing thin outer layer and inner layer. (c) Line scan of region 2 showing both outer layer particle and compact inner layer.

3.2.3 Comparison of Film oxidized at Various Potentials in Zn free Primary Water

Comparing the film compositions oxidized at different potentials, it is found that the outer layer contains over 80% Ni at all potentials. At lower potentials where the surface is partially covered with irregular shape particles that could be either whiskers or particles, the outer layer is composed of NiO and some $NiFe_2O_4$, with higher content of Ni at -550 mV $_{SHE}$. The change in outer layer composition could be related with the rate of metal release from the alloy. Since -700 mV $_{SHE}$ is close to the Ni/NiO potential, more Ni^{2+} cations would be released to the solution at -550 mV $_{SHE}$, thus more likely to precipitate back to the alloy surface. As potential further increases, the passive layer oxidized at -223 mV $_{SHE}$ not only has a different morphology, but also slightly different composition. The fact that Cr and Fe are both observed in the outer layer particles indicates higher rate of Fe and Cr is released into the solution at -223 mV $_{SHE}$ compared to -550 mV $_{SHE}$. Variation of outer layer composition along the outer layer thickness is observed at -223 mV $_{SHE}$, suggesting that the outer layer can be a combination of outer layer films formed at different potentials. The protectiveness of the film cannot be concluded by the outer layer because of scattered distribution, but is more dependent on the compact inner layer. The inner layer contains Cr_2O_3 of 7-12 nm at all potentials, with some Cr-rich spinel observed in some line scans. The thickness of the inner layer does not show a significant change over potentials. Besides, a Cr-depleted/ Ni-enriched zone is observed non-continuous at -700 mV $_{SHE}$ and -

233 mV $_{SHE}$. The formation of the region is related to the selective dissolution / metal reduction, and it will be discussed later in the report.

3.3 Effect of Potential on Passive Film Formation in Zn Containing Solution

3.3.1 Structure of Passive Film Formation Zn Containing Solution

Figure 3-13 illustrates the top-down surface of Alloy 600 oxidized at -700 mV $_{SHE}$ at 320 ºC for 4 hours in high temperature primary water with 0.1ppm Zn addition (added as zinc acetate). Unlike the whiskers that are found on the surface in Zn free primary water, scattered octahedron-shaped particles are observed on Alloy 600. Octahedral oxides are also found by other researchers [18], [34], and these particles are generally categorized as outer layer. A large variation of particle size is observed, that ranges from 80-500 nm along the edge. Small particles are found underneath the large particles, with a more uniform size distribution, averaging around 40 nm in diameter. The TEM cross section of the film oxidized under this condition is shown in Figure 3-14. The outer layer particles are measured with thickness ranging between 80 nm and 300 nm, which agrees with what is found in the SEM image. A continuous inner layer is observed, the chemical composition of which will be discussed in the following text.

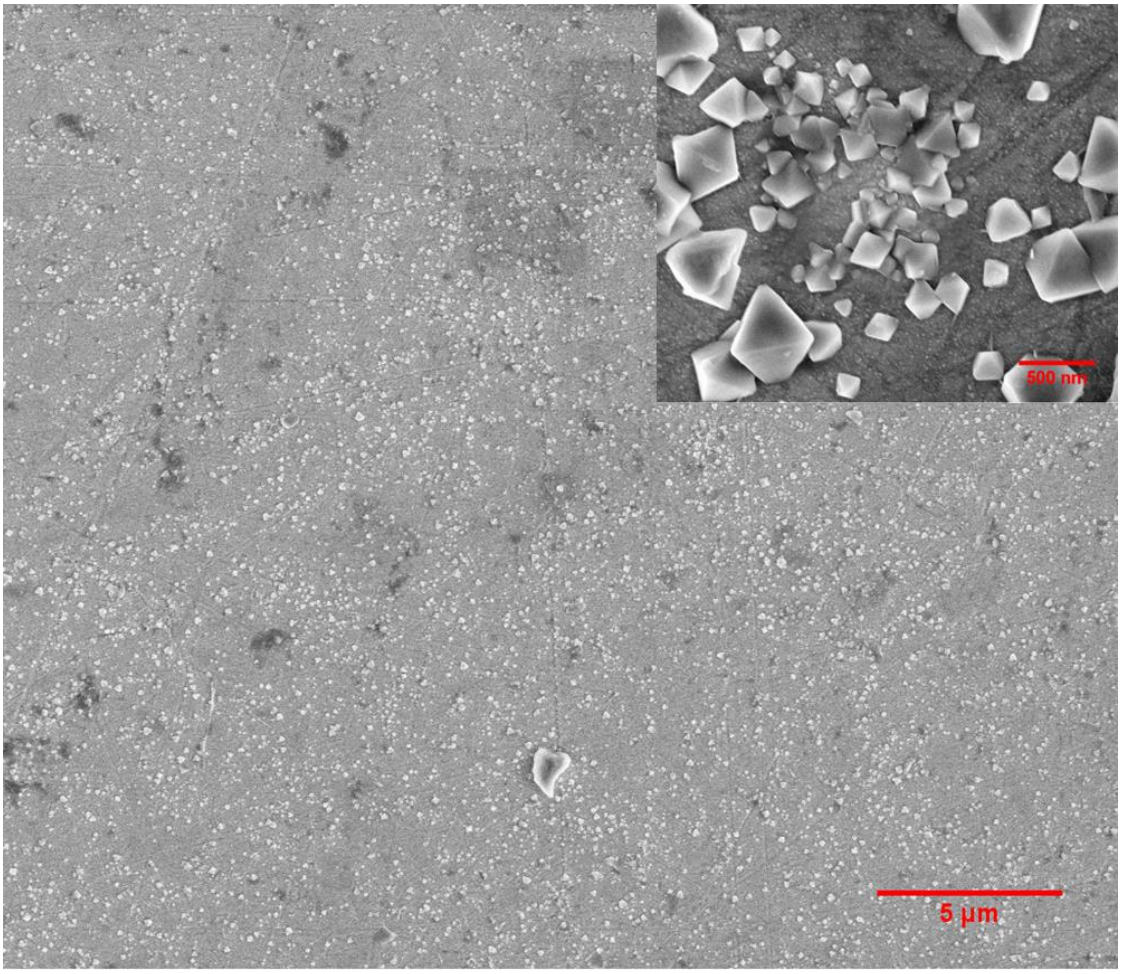

Figure 3-13: SEM view of the oxide film formed at -700 mV $_{SHE}$ at 320 °C in Zn containing PWR simulated primary water, showing octahedral oxides and small particles.

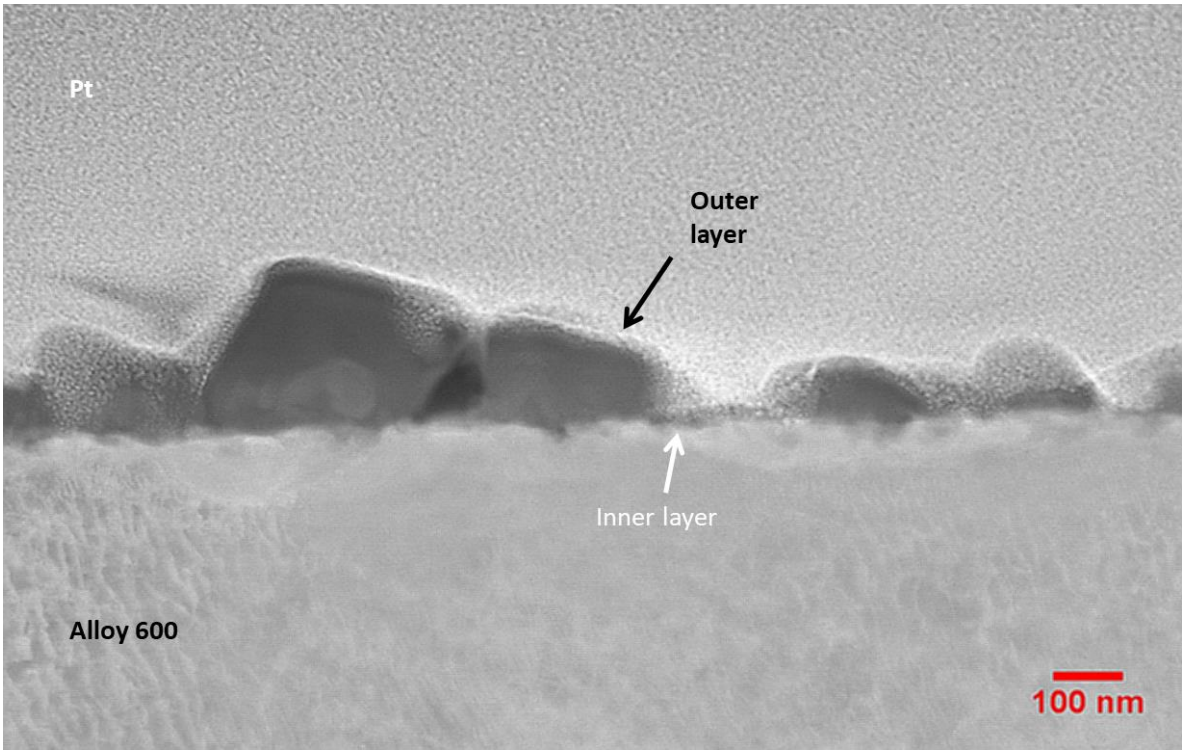

Figure 3-14: TEM cross-section of the oxide film formed at -700 mV $_{SHE}$. In the image, the lower part is the Alloy 600 matrix, whereas the upper part is the deposited Pt layer.

The top-down image showing the morphology of the surface of Alloy 600 oxidized at -550 mV $_{SHE}$ is presented in Figure 3-15. Similar to what is observed in Figure 3-13, octahedron-shaped particles are observed on the metal surface, with a higher density than at -700 mV $_{SHE}$. Particles also have a large variance of size, ranging from 150 nm to 500 nm. Small particles with a uniform size and compact distribution are also found on the sample, and the average diameter of the particles is 55 nm. Figure 3-16 shows the cross-section of part of the film on Alloy 600. It is found that the outer layer oxide particles have a more uniform thickness of 80-120 nm compared with what is observed at a lower potential, and displays a covers more region of the inner layer. The inner layer is found below the particles with a slightly different contrast in the image.

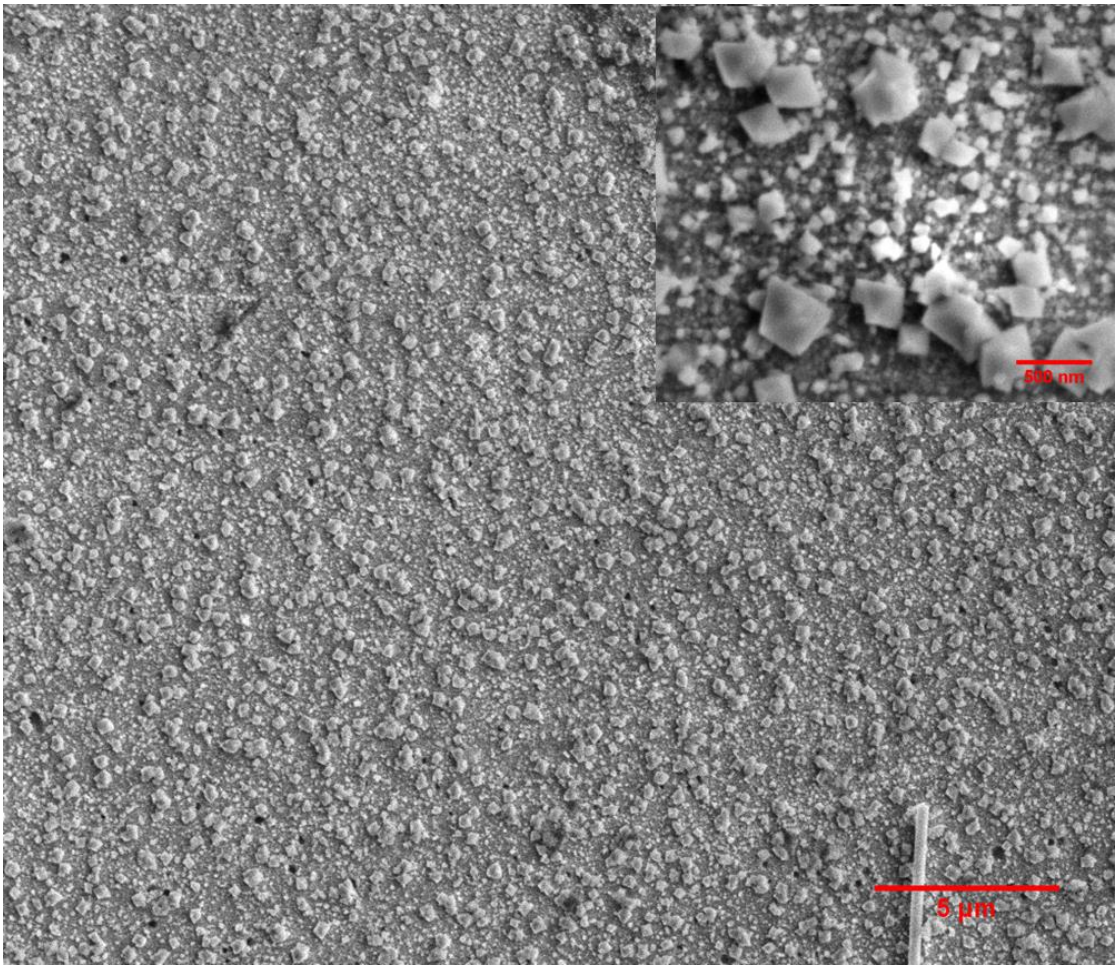

Figure 3-15: SEM view of the oxide film formed at -550 mV $_{SHE}$ at 320 °C in Zn containing PWR simulated primary water, showing octahedral oxides and small particles.

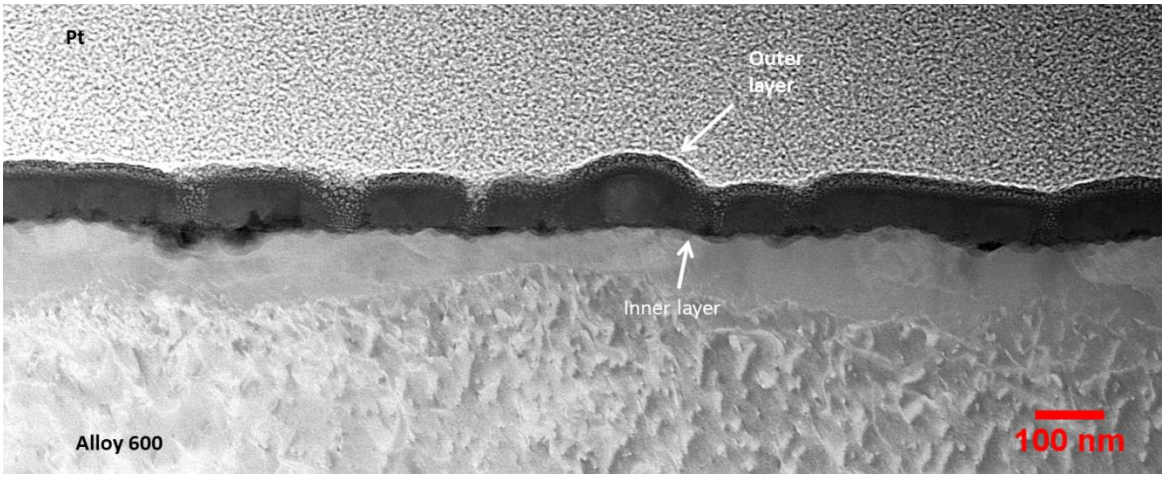

Figure 3-16: TEM cross-section of the oxide film formed at -550 mV $_{SHE}$. In the image, the lower part is the Alloy 600 matrix, whereas the upper part is the deposited Pt layer.

Figure 3-17 presents the surface of the Alloy 600 oxidized at -223 mV $_{SHE}$ in Zn containing primary water. At lower magnification, the alloy displays a surface with uniform morphology. A very thin film is expected, because some scratches can be observed on the surface. Comparing with the surface shown in Figure 3-13 and Figure 3-15, no large particles (>100 nm in diameter) are observed on Alloy 600 in the higher magnification image. The particles are densely packed on the surface, averaging around 70 nm. The cross-section image of this region is shown in Figure 3-18. The outer layer is measured between 20-60 nm thick, and covers most of the inner layer surface.

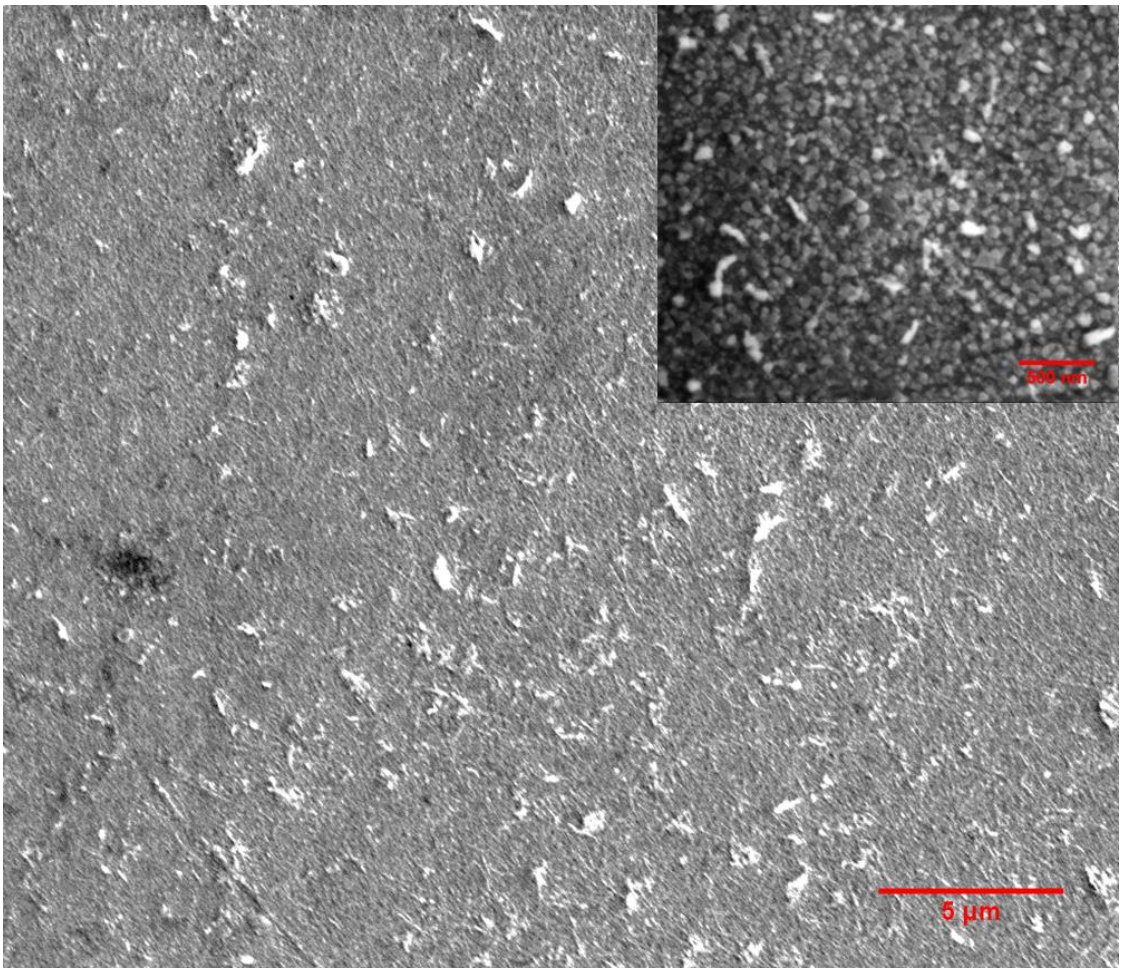

Figure 3-17: SEM view of the oxide film formed at -223 mV $_{SHE}$ at 320 °C in Zn containing PWR simulated primary water, showing small particles.

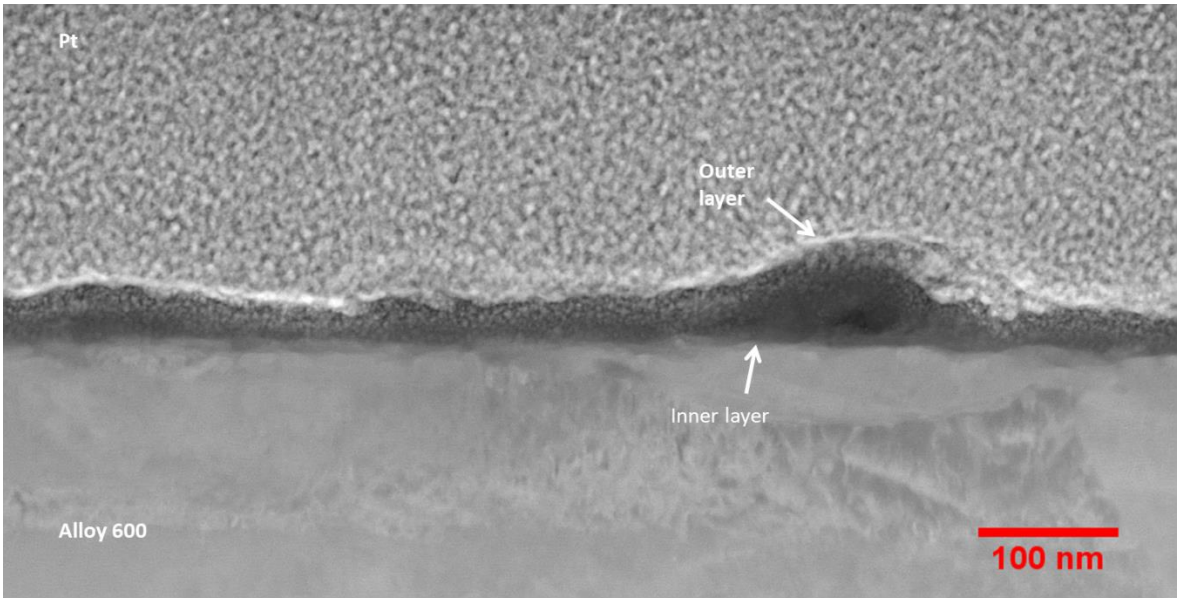

Figure 3-18: TEM cross-section of the oxide film formed at -223 mV $_{SHE}$. In the image, the lower part is the Alloy 600 matrix, whereas the upper part is the deposited Pt layer.

3.3.2 Composition of Passive Layer formed on Alloy 600 in Zn Containing Primary Water

The compositional analyses of the passive film formed at different potentials will be discussed in this section, focusing on concentrations of Ni, Cr, Fe, Zn and O. The mass fractions for Ni, Cr, Fe, and Zn are calculated with balancing Pt%.

The elemental map of the film formed at -700 mV $_{SHE}$ is shown in Figure 3-19 (a). It is observed that the outer layer particles generally contain Zn, Fe and Ni. Based on the color variations, it is indicated that the particles do not have uniform compositions, with some particles rich in Zn and some particles rich in Fe. The continuous inner layer shows high concentration of Cr, which is similar to what is observed in that formed in Zn free solutions. Figure 3-20 (b) confirms the non-uniformity of particle composition, indicating that Fe rich particles grow close to the inner layer interface, whereas Zn rich particles occupy the region closer to the film/solution interface. The Cr-rich inner layer is measured around 10-13 nm along the surface.

(a)

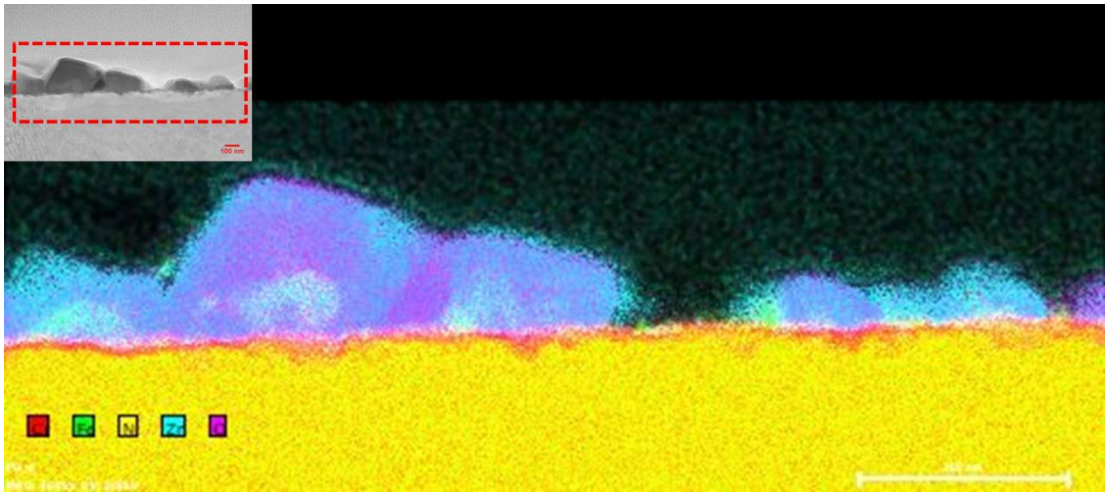

(b)

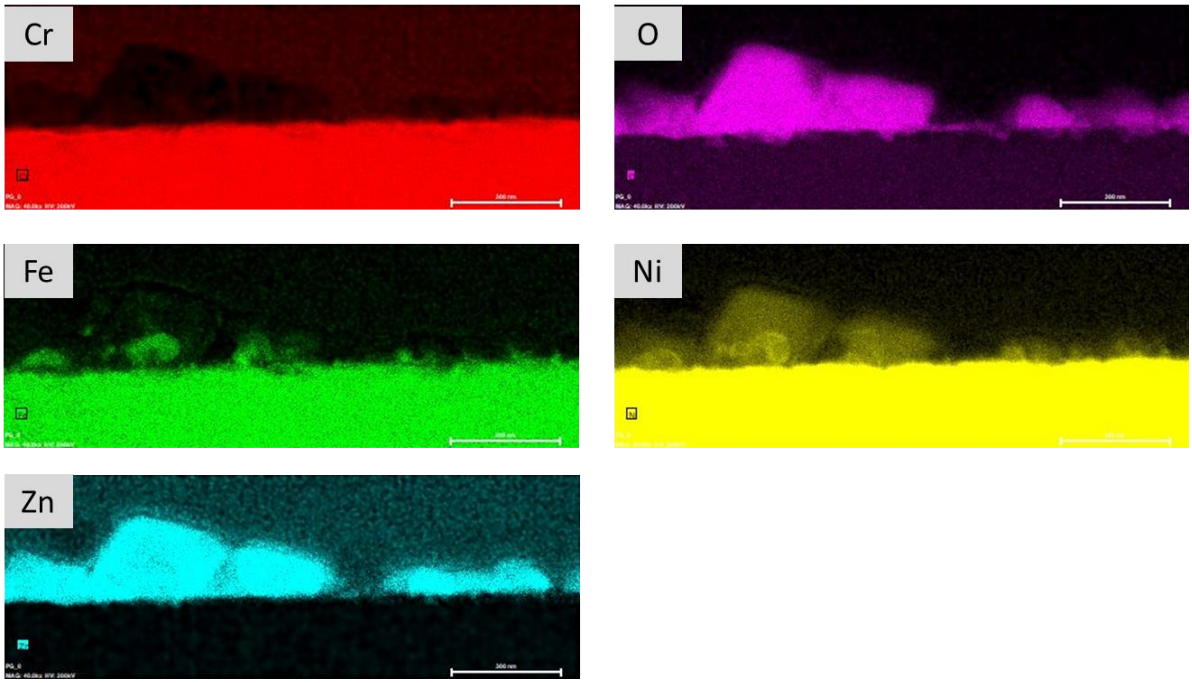

Figure 3-19: EDX mapping of the passive film formed at -700 mV $_{SHE}$ in Zn containing primary water. (a) overlaying elemental map. (b) individual elemental maps for Cr, O, Fe, Ni, Zn.

Figure 3-20 shows the elemental composition along different line scans on the cross-section. In line scan #1, the outer layer particle, inner layer and oxide below inner layer can all be identified. The reason that oxygen concentration is not constant along the outer layer region is due to the change in thickness along the scan. The outer layer particle is composed of mostly Zn and Ni, with the total weight percent of 90%. Fe concentration is measured between 8% and 10% in the outer layer. The composition of the outer layer can be $(Ni_xFe_yZn_{1-x-y})O$. Cr rich inner layer is measured around 16 nm, with a composition of Cr_2O_3 and $(Ni_xZn_{1-x})Cr_2O_4$ after calculating the contribution of metal matrix to the signal. It is also observed that there is a concentration gradient for Zn in the inner layer, indicating that the chromite is located in the outer part of the inner layer, and Cr_2O_3 is located closer to the alloy/film interface. Line #2 scans the area that

does not contain apparent outer layer, but only presents the information of an inner layer. The inner layer is found to be 18nm thick, and it is composed of Ni, Cr, Fe and Zn. The composition of the film is determined to be $(Ni_xZn_{1-x})Cr_2O_4$ and Cr_2O_3. A reduction in Zn content is found from the film/solution interface to the metal/film interface, indicating the direction of Zn transport in the oxide, and that the chromite is located at the film/solution interface. In Figure 3-20 (d), line scan #3 presents the composition along a Zn/Fe-rich outer layer particles and an inner layer. The outer layer consists of $(Ni_xFe_yZn_{1-x-y})O$. The outer part of the outer layer is rich in Zn, and has a similar composition to what is found in line #1, in which Fe concentration is measured around 8-10%. The inner part of outer layer contains less Zn and the Fe concentration increases to 16-18%. The inner layer is around 18nm thick, and is composed of $(Fe_xZn_{1-x})Cr_2O_4$ and Cr_2O_3, with Zn concentration 2-4%.

It can be concluded from the line scans that the Zn deposition in both the outer layer and inner layer creates a composition gradient from the film/solution surface to the alloy/film interface. The difference in Zn rich and Fe rich part of the outer layer particle can be due to the difference in Fe diffusion at different parts on the alloy surface. Although Zn is found incorporated into the inner layer, low concentration is observed, and it can be formed by transport and substitution of inner layer divalent metal ions.

(a)

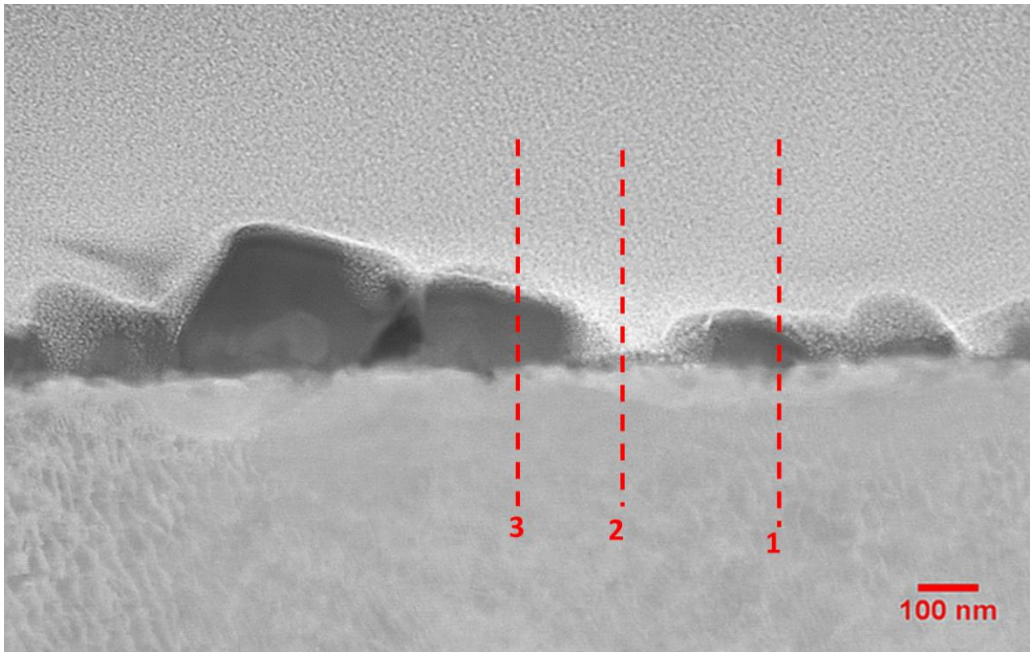

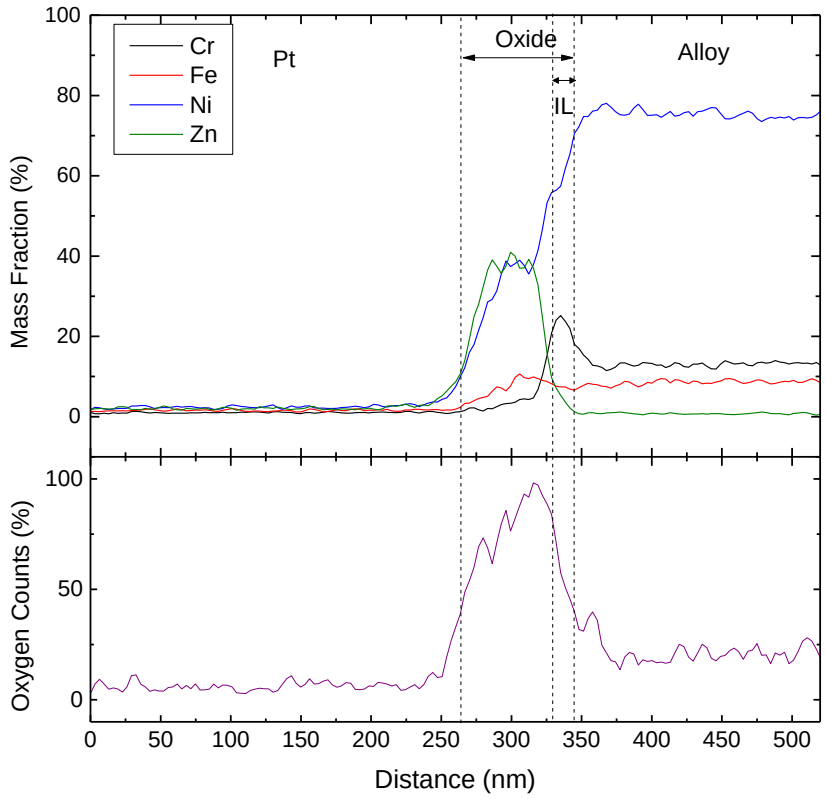
Cr
Fe
Ni
Zn
Pt
Oxide
IL
Alloy
Mass Fraction (%)
Oxygen Counts (%)
Distance (nm)
0
20
40
60
80
100
0
50
100
150
200
250
300
350
400
450
500

(b)

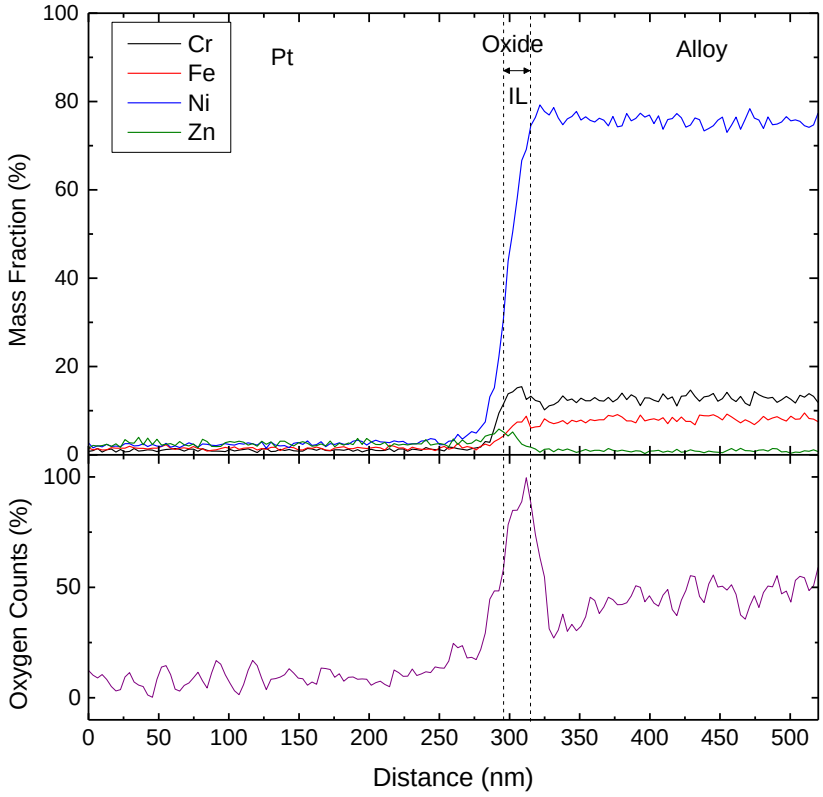
Cr
Fe
Ni
Zn
Pt
Oxide
IL
Alloy
Mass Fraction (%)
Oxygen Counts (%)
Distance (nm)
0
20
40
60
80
100
0
50
100
150
200
250
300
350
400
450
500

(c)

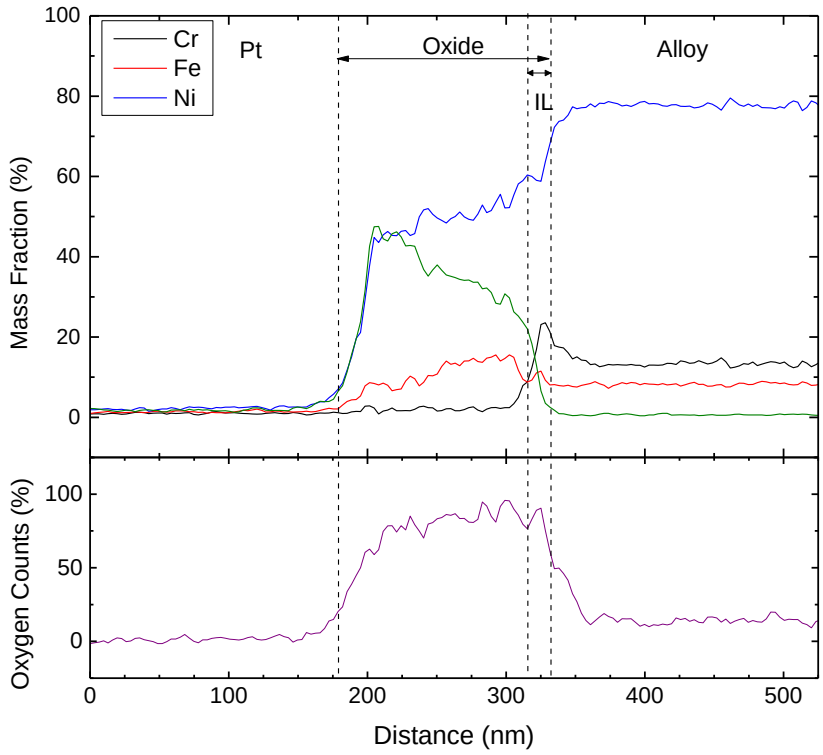

(d)

Figure 3-20: Line scan on different regions of Alloy 600 passive layer oxidized at -700 mV $_{SHE}$ in Zn containing primary water. (a) TEM image showing regions of line scans. (b) Line scan of region 1 showing outer layer, inner layer and oxide below inner layer. (c) Line scan of region 2 showing mostly inner layer. (d) Line scan of region 3 showing outer layer particles and inner layer.

Figure 3-21 shows the elemental mapping of the passive film oxidized at -550 mV $_{SHE}$, and both the outer layer particles and inner layer can be identified. The outer layer particles are rich in Zn, Fe and Ni, similar to what is found at a lower potential. It is also found that the composition of the particles is not consistent along the surface. Fe is found to be richer closer to the inner layer, whereas the Ni and Zn show higher color intensity in various locations in the particles. The inner layer contains high content of Cr and is measured around 7nm. Besides, a few oxides below the inner layer are also observed.

(a) 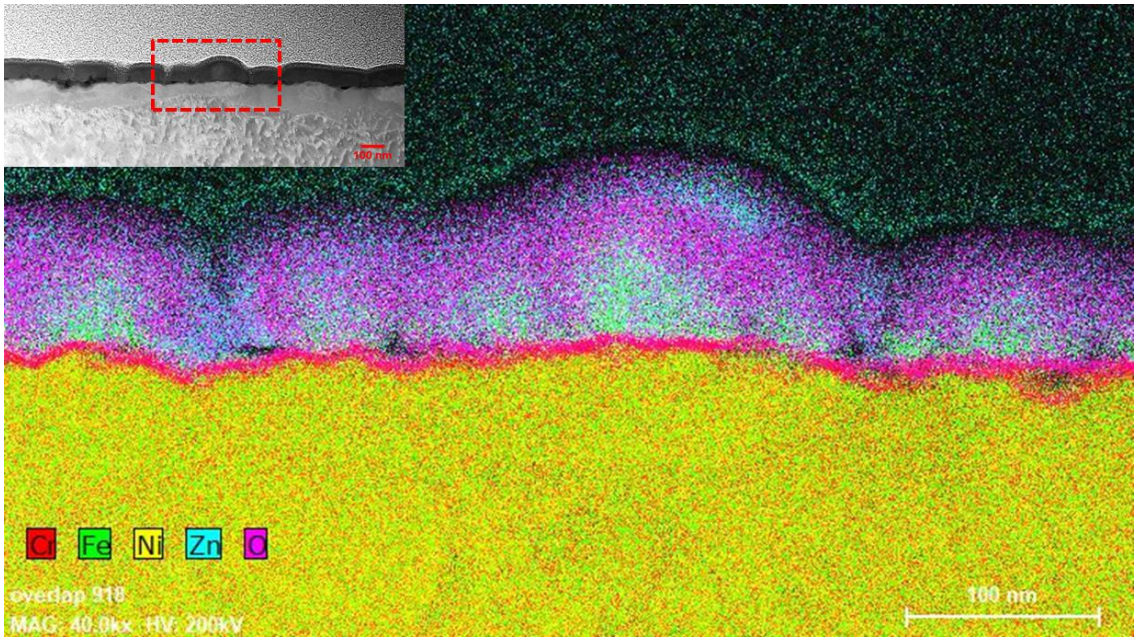

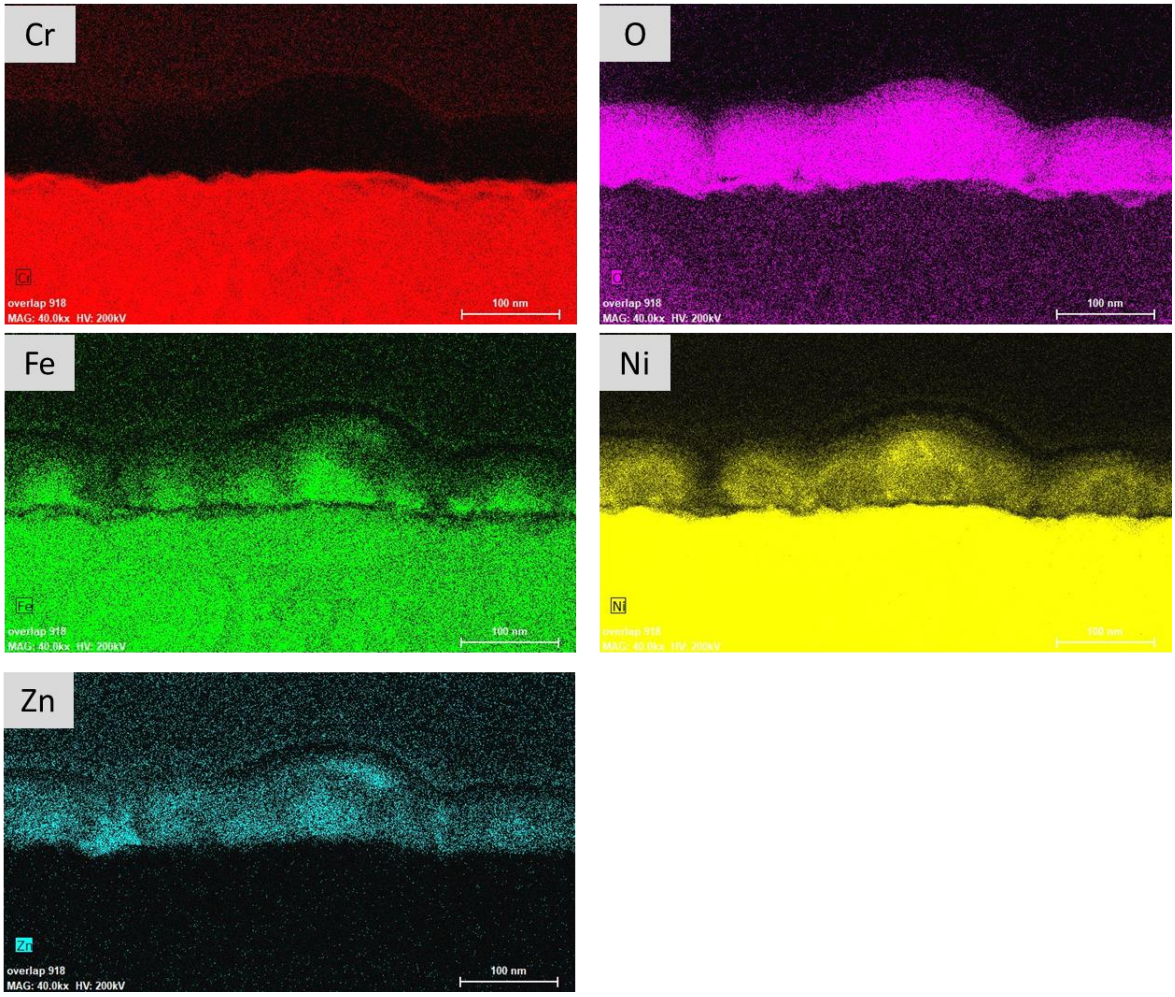

(b)

Figure 3-21: EDX mapping of the passive film formed at -550 mV $_{SHE}$ in Zn containing primary water. (a) overlaying elemental map. (b) individual elemental maps for Cr, O, Fe, Ni, Zn.

The compositional line scans along the thickness of passive film at different regions are shown in Figure 3-22. All three line scans indicate that Zn has a higher concentration in the region closer to the film/solution surface, whereas Fe has a higher concentration closer to the metal/film interface. Regardless of the composition variation within the particle, the outer layer is found to contain $(Ni_xFe_yZn_{1-x-y})O$. The outer part of the outer layer particle contains Fe of 13-16 wt% and a total concentration of Ni and Zn of around 85%, in which Zn content varies between 20% and 30%. The inner part of the outer layer particles is composed of 25-30% Fe, 15-20% Zn and remaining Ni. The inner layer measures around 7nm thick, and contains 2-3% Zn with a concentration gradient along the thickness. The composition of the inner layer is mostly Cr_2O_3 and little $(Fe_xZn_{1-x})Cr_2O_4$. It is worth noting that some internal oxide nodules underneath the alloy/film interface can be identified from line scan #1 shown in Figure 3-22 (b). The composition is calculated to be $NiCr_2O_4$ surrounded by Cr_2O_3 at the periphery. Similar internal oxidation in the alloy is also reported by other researchers on Alloy 600 [34], [36], and this is an illustration proving that oxides are formed at the metal/film interface rather than IL/OL interface.

(a)

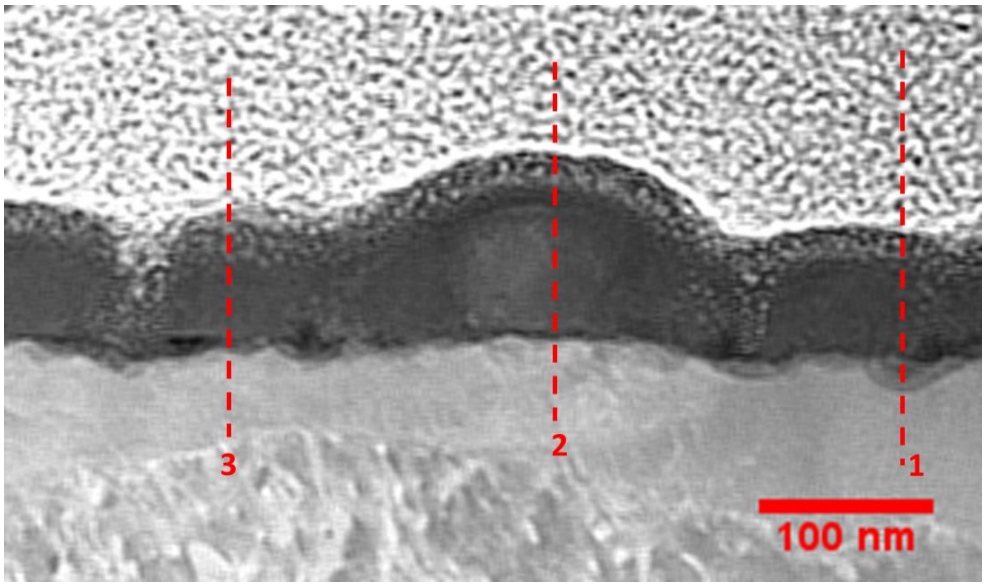
3
2
1
100 nm

(b)

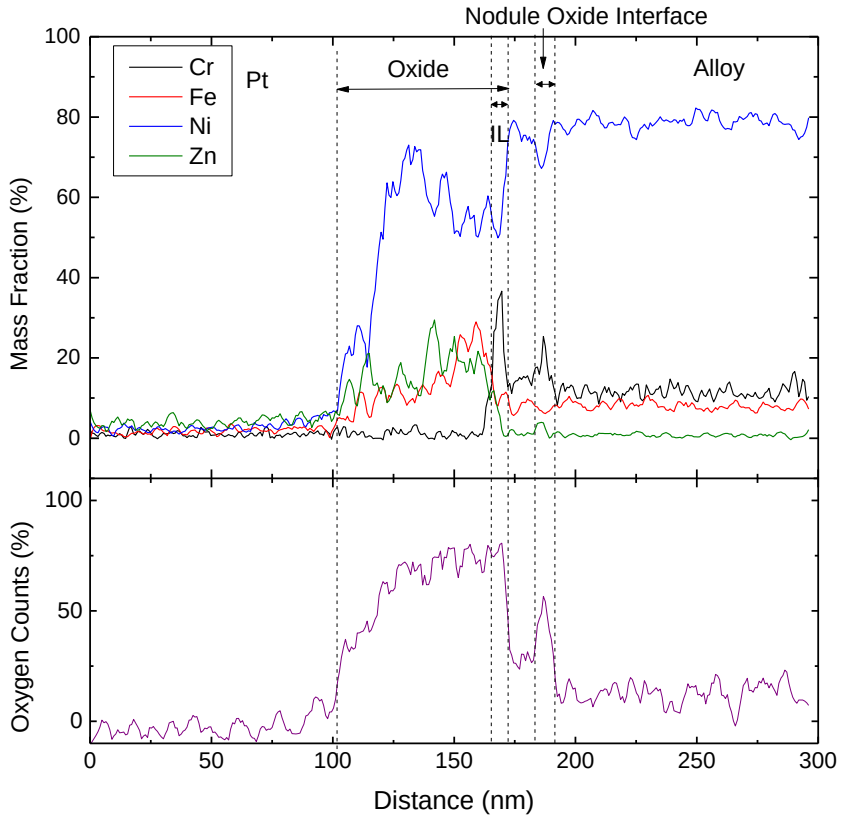
Nodule Oxide Interface
Cr
Fe
Ni
Zn
Pt
Oxide
Alloy
IL
Mass Fraction (%)
Oxygen Counts (%)
Distance (nm)
0
20
40
60
80
100
0
50
100
150
200
250
300

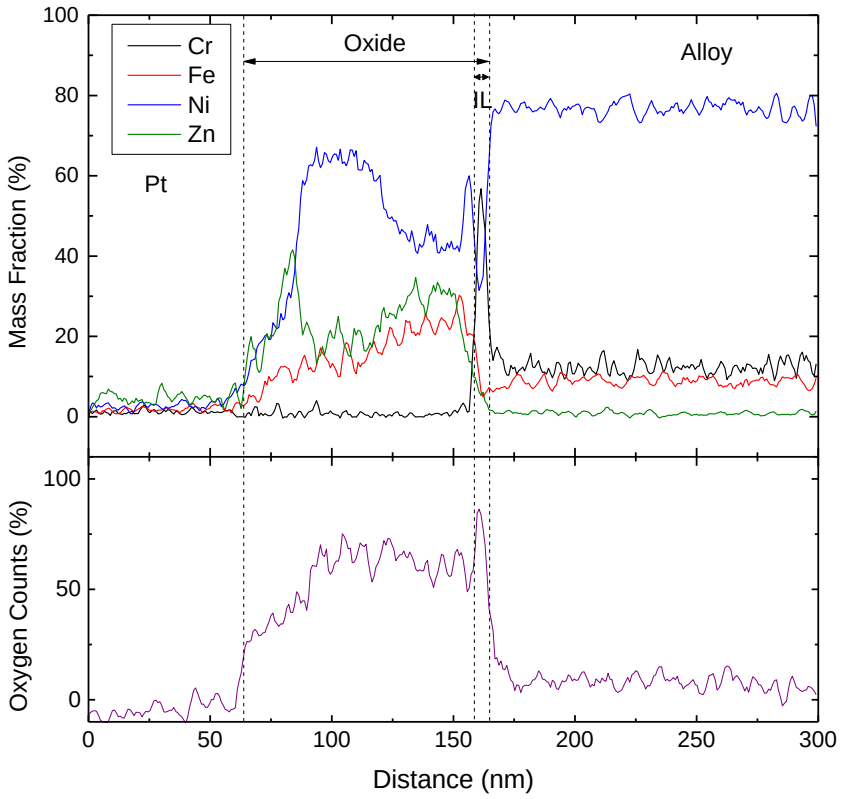
Cr
Fe
Ni
Zn
Pt
Oxide
Alloy
IL
Mass Fraction (%)
Oxygen Counts (%)
Distance (nm)
0
20
40
60
80
100
0
50
100
150
200
250
300

(c)

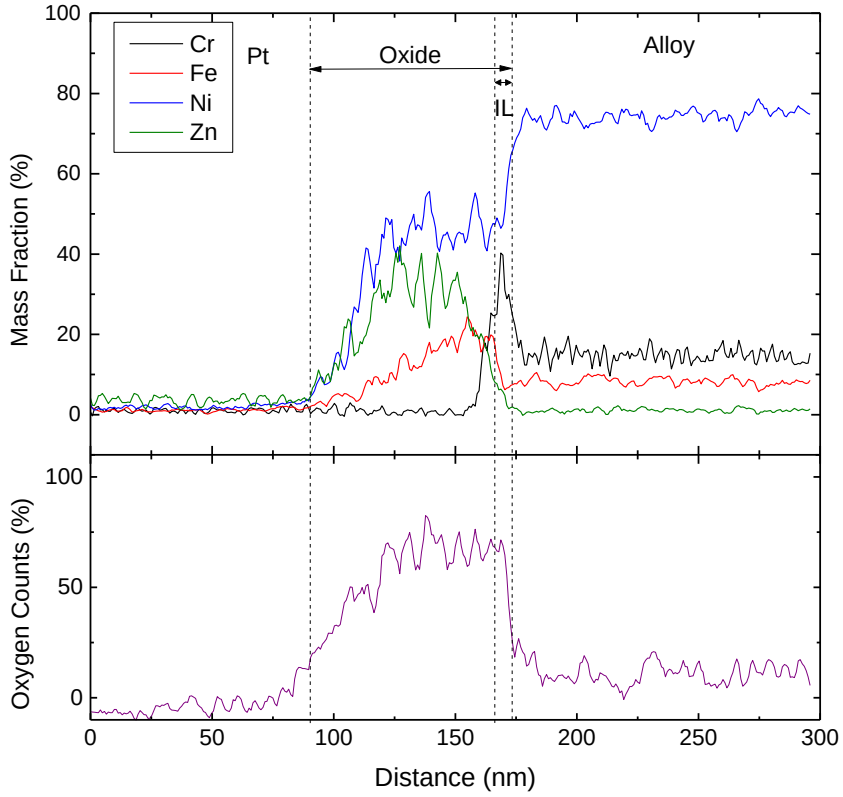

(d)

Figure 3-22: Line scan on different regions of Alloy 600 passive layer oxidized at -550 mV $_{SHE}$ in Zn containing primary water. (a) TEM image showing regions of line scans. (b) Line scan of region 1 showing outer layer, inner layer and oxide below inner layer. (c) Line scan of region 2 showing outer layer particles and inner layer. (d) Line scan of region 3 showing outer layer particles and inner layer.

The mapping analysis for the five elements for the oxide film oxidized at -223 mV $_{SHE}$ is shown in Figure 3-23. In the outer layer region, the particles are more continuous than what is formed at lower potentials. Little Fe and Zn variations are also observed regarding color intensity along the film. The inner layer is measured to be between 7-10 nm thick and consists of high concentration of Cr. Regions of internal Cr rich oxide underneath the inner layer in the alloy as well as Cr depleted zone are also observed in the figure.

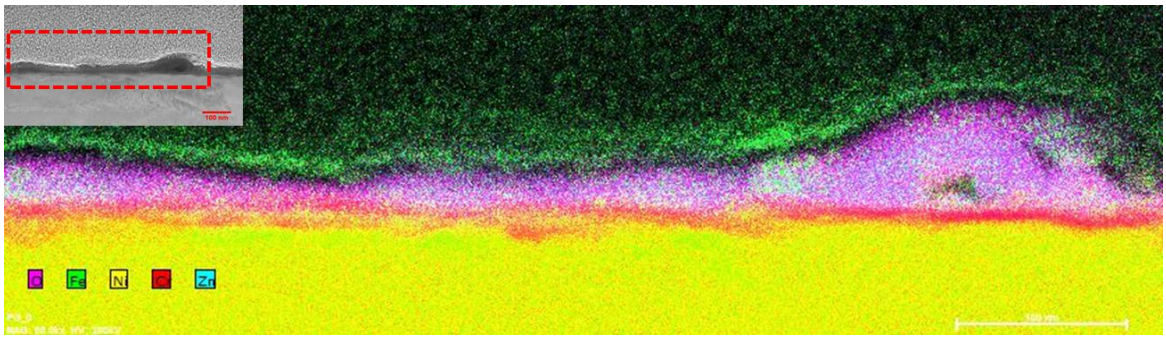

(a)

(b)

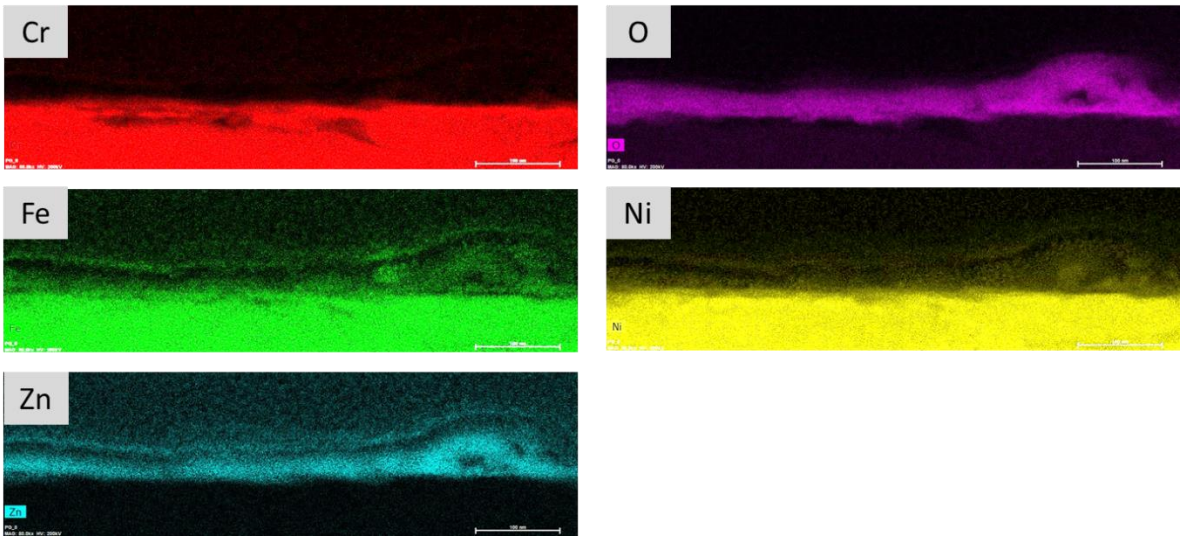

Figure 3-23: EDX mapping of the passive film formed at -223 mV $_{SHE}$ in Zn containing primary water. (a) overlaying elemental map. (b) individual elemental maps for Cr, O, Fe, Ni, Zn.

Two line scans at different locations perpendicular to the surface are presented in Figure 3-24, in which line #1 scans a thicker outer layer and line #2 shows a thinner outer layer. Line scan #1 shows a 45-nm thick outer layer with concentration gradient along the scan direction, which is Zn/Fe rich toward the film/solution interface and is Ni-rich toward the IL/OL interface. An 8-nm Cr-rich inner layer is found underneath the outer layer. The outer layer consists of $(Ni_xZn_{1-x})O$ and $(Ni_xZn_{1-x})Fe_2O_4$, with the x value varyinng along the oxide thickness, and the inner layer is composed of $(Ni_xZn_{1-x})(Cr_yFe_{1-y})_2O_4$ and Cr_2O_3, with most of the spinel located at the IL/OL interface. It is noted that the oxygen signal count decreases in the area where Ni content is high, and this is likely due to the reduction in sample thickness in this region. Line scan #2 presents not only a 20-nm thick outer layer and a 7-nm thick inner layer, but also a 7-nm thick internal oxide and a 15-nm Cr-depleted zone. The outer layer consists of $(Ni_xZn_{1-x})O$ and Cr/Fe-rich spinel, and inner layer consists of $(Ni_xZn_{1-x})(Cr_yFe_{1-y})_2O_4$ and Cr_2O_3. The internal oxide is composed of $NiCr_2O_4$, which is similar to the internal oxide formed at -550 mV $_{SHE}$. The Cr-depleted / Ni-enriched region is caused by selective dissolution or metal reduction.

(a)

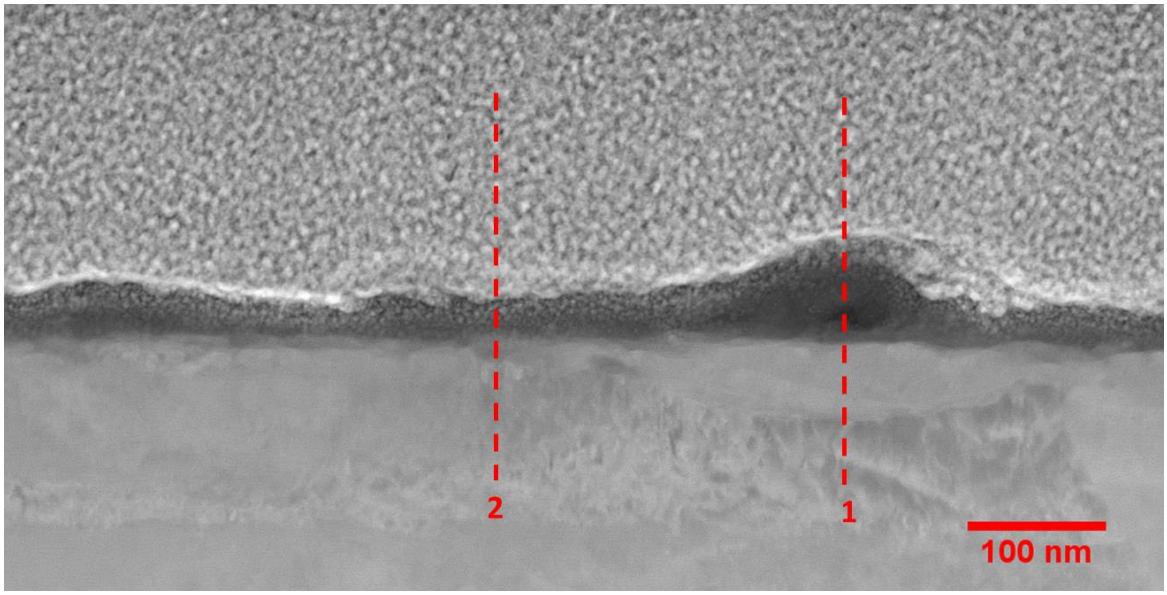
2
1
100 nm

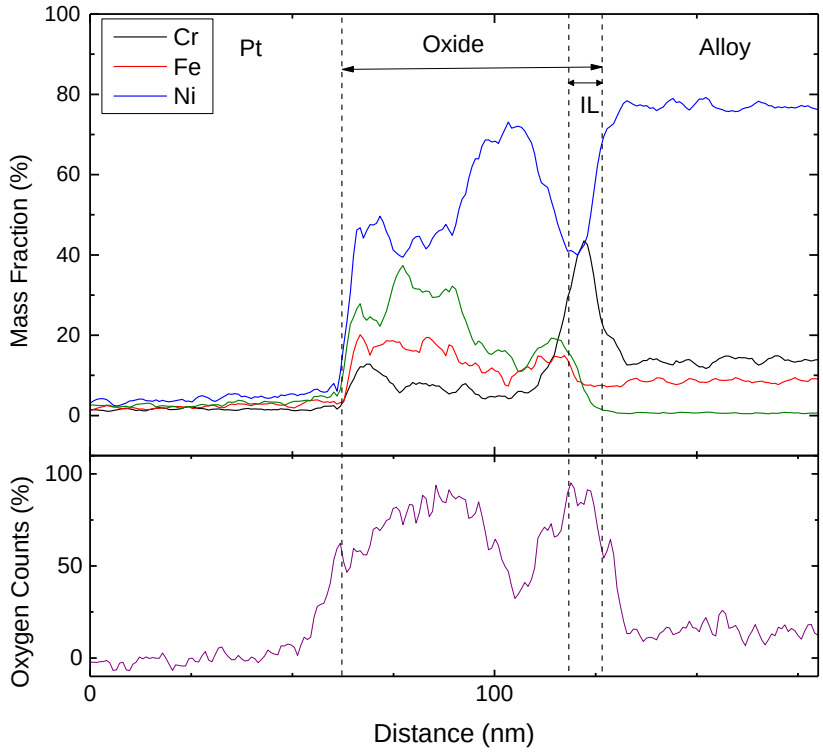
Cr
Fe
Ni
Pt
Oxide
IL
Alloy
Mass Fraction (%)
Oxygen Counts (%)
Distance (nm)
0
20
40
60
80
100
0
50
100
0
100

(b)

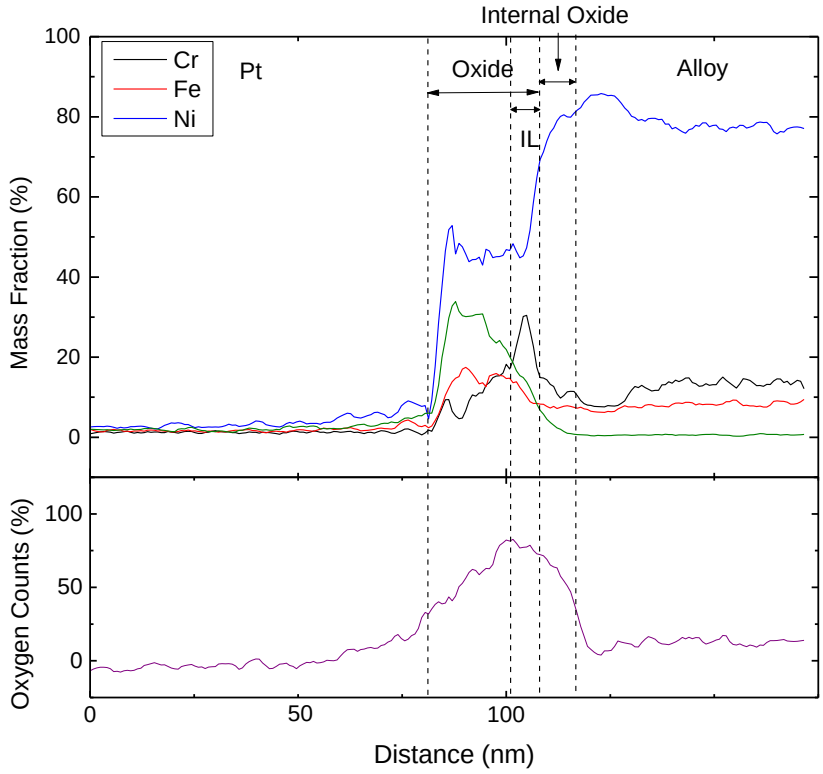

(c)

Figure 3-24: Line scan on different regions of Alloy 600 passive layer oxidized at -223 mV $_{SHE}$ in Zn containing primary water. (a) TEM image showing regions of line scans. (b) Line scan of region 1 showing outer layer and inner layer. (c) Line scan of region 2 showing outer layer particles, inner layer and oxide below inner layer.

3.3.3 Comparison of Film oxidized at Various Potentials in Zn Containing Primary Water

The results indicate that Zn is incorporated in both the outer layer particles and the compact inner layer. The outer layer formed at all potentials consists of Ni/Fe/Zn-rich oxide and Fe-rich spinel. In the outer layer, it is found that the thickness of the oxide particles reduces with potentials. At all potentials, Zn presents a concentration gradient along the thickness of the particles, indicating the direction of transport for Zn.

At -700 mV $_{SHE}$ and -550 mV $_{SHE}$, Fe rich regions are observed close to the inner/outer layer interface. Because both Fe and Ni transport from the metal/inner layer interface and the outer layer is formed through dissolution and precipitation, it is likely that Zn replaces Ni in the film formation and prevents Fe dissolution at the outer layer/inner layer interface. At -223 mV $_{SHE}$, Cr is found in the outer layer, indicating that more outward metal diffusion takes place, and the inner layer may be less protective at this potential. The inner layer thickness is found to decrease from 12-14 nm to 7 nm between -700 mV $_{SHE}$ and -550 mV $_{SHE}$, and increases to 8-10 nm at -223 mV $_{SHE}$, and the change in thickness may be a result of change in rate of oxidation for the alloy.

3.4 Effect of Zn in Passive Film Composition on Alloy 600

Comparing the passive film formed in both Zn free and Zn containing solution, it is found that Alloy 600 always generates a compact inner layer and a porous outer layer. The intensity of the outer layer particles becomes higher when oxidized at a higher potential, and the distribution of the oxides become more uniform. The thickness of the inner layer generally varies between 6-16nm, and is thinnest at -550 mV $_{SHE}$.

The largest difference in morphology between the oxide formed in Zn and Zn free solution is the outer layer oxidized at lower potentials, i.e. -700 mV $_{SHE}$ and -550 mV $_{SHE}$. In Zn free solution, the outer layer consists of whiskers with different orientations, some of which are intercepted by the cutting plan during the TEM sample preparation. In Zn containing solution, rather than whiskers, octahedral particles of various diameters are observed, and as a result, the oxide particles have larger coverage on the alloy surface and create a more homogeneous morphology. At -223 mV $_{SHE}$, the films generated are very similar when observed from SEM and cross-section TEM.

The composition variance of the passive film oxidized at different potentials is shown in Table 3-1. It is shown that in Zn containing solutions, Zn usually substitutes for Ni^{2+} and Fe^{2+} in the oxide that is observed in Zn free solutions. .

Table 3-1: Composition of passive film oxidized at different potentials in both Zn free and Zn containing solutions

	-700 mV $_{SHE}$, -550 mV $_{SHE}$		**-223 mV $_{SHE}$**	
	Outer Layer	**Inner Layer**	**Outer Layer**	**Inner Layer**
Zn free	Mostly NiO, little $(Ni_xFe_{1-x})O$	Mostly Cr_2O_3, little Cr-rich spinel	NiO, $Ni(Cr_xFe_{1-x})_2O_4$	Mostly Cr_2O_3, little $(Fe,Ni)Cr_2O_4$
Zn containing	$(Ni_xFe_yZn_{1-x-y})O$	Mostly Cr_2O_3, little Cr-rich spinel	$(Ni_xZn_{1-x})O$, $(Ni_xZn_{1-x})(Cr_yFe_{1-y})_2O_4$	Mostly Cr_2O_3, little Cr/Fe/Zn containing spinel

Figure 3-25 presents the compositional analysis for different metallic components in the outer layer. Since concentration gradients are found in the outer layer formed in Zn containing solution, Figure 3-25 (b) shows an outer part (S/OL) and an inner part (OL/IL) of the outer layer. The inner layer composition is not shown because the majority of the inner layer is Cr_2O_3. Following the concentration gradient of Zn, chromites/ferrites are found at the OL/IL interface, and will be discussed in the following chapters.

The preference of Zn substitution in the outer layer can be found by comparing the mass fraction of each element at the outer layer . Due to the concentration gradient in Zn-containing solution, only the IL/OL part is compared with the outer layer mass fraction in Zn-free solution. It is found that the concentration of chromium and iron are identical at -700 mV $_{SHE}$ and -223 mV $_{SHE}$, indicating that most of Zn replaces Ni in the oxide. At -550 mV $_{SHE}$, a high Fe content in the outer layer (IL/OL) is found in Zn containing solution, indicating more precipitation of Fe in the outer layer compared to that in Zn free solution. The fact that Zn content is slightly lower at this potential compared to -700 mV $_{SHE}$ also proves that Zn is less likely to substitute Fe^{2+}.

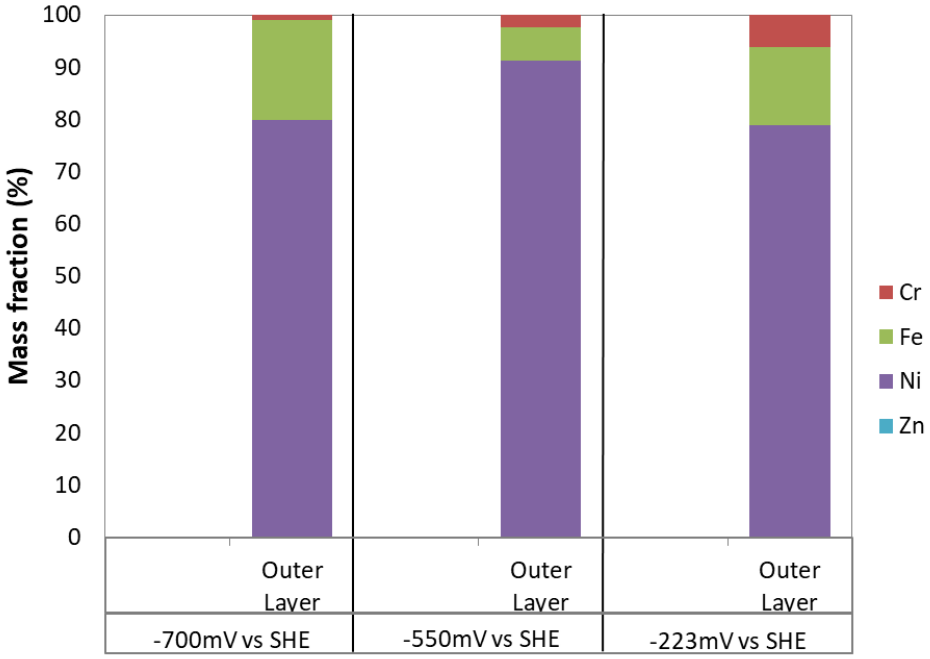

(a)

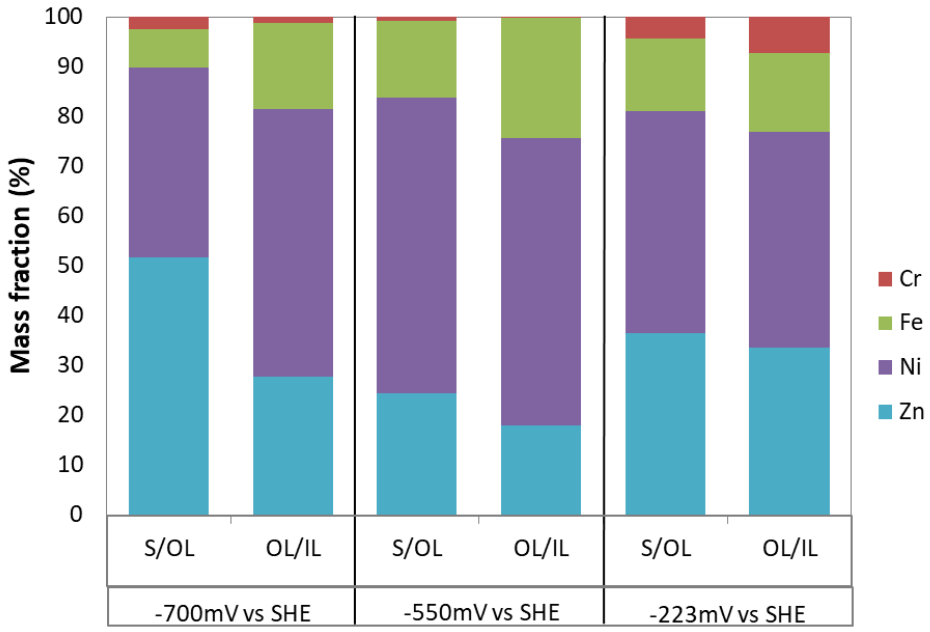

(b)

Figure 3-25: Compositional variance of outer layer on Alloy 600 formed in (a) Zn free solution, (b) Zn containing solution.

Several researchers [26], [37] report that the inner layer governs the passivity of the film formed on Alloy 600. However, with very little change in thickness of the inner layer and in composition of the inner layer with Zn incorporation, it cannot be concluded from the TEM results that Zn makes the inner layer more protective. Zn changes the morphology of the outer

layer by increasing the intensity and homogeneity of outer layer particles, and it may help reducing the overall corrosion rate of the alloy. More analysis on kinetic parameters will be presented in the following chapters.

Chapter 4. Electrochemical Analysis on Alloy 600

4.1 Potentiodynamic Scan on Alloy 600

The most common way of evaluating the electrochemical behavior of a material is to characterize its polarization behavior. The polarization curve of Alloy 600 at 320 º in Zn free and Zn containing solutions are both shown in Figure 4-1. The test was conducted at 1 mV/s and the sample was cathodically polarized at -1.9V $_{SHE}$ during the heating process.

In Zn-free solution, the corrosion potential is observed at -0.751 mV $_{SHE}$, and the current remains below 100 μA/cm^2 until +137 mV $_{SHE}$. Below the corrosion potential, the reduction reaction of $2H_2O + 4e^- = H_2 + 4OH^-$ takes place on the working electrode, given that the solution pH is 7.28. Above the corrosion potential, there is a local maximum of current at -556 mV $_{SHE}$, which could either be related to a change in passive layer or an influence from the reduction reaction. The Pourbaix diagram of Alloy 600 at 320 ºC constructed by Kauffman [35], shown in Figure 4-2, predicts the thermodynamically stable species, and the change in stable species with potential in the Pourbaix diagram may be used to explain the change in current density in the polarization curve. It is observed from Figure 4-2 that at pH ≈ 7.3, $FeCr_2O_4$ and NiO would be stable between -730 mV $_{SHE}$ and -500 mV $_{SHE}$, whereas $NiFe_2O_4$, Cr_2O_3 and NiO are stable oxides between -500 mV $_{SHE}$ and 0 V $_{SHE}$. The local maximum observed in the polarization curve does not agree perfectly with the Pourbaix diagram but lies around 170 mV above the equilibrium potential of NiO and approximately 40 mV above the potential at which iron chromite transitions to a combination of chromium oxide and nickel ferrite. It is assumed that the local maximum is caused by the transition from Fe^{+2} to Fe^{+3}, from which potential Cr_2O_3 becomes more stable than $FeCr_2O_4$. Above 0V $_{SHE}$, Cr^{+3} transforms into Cr^{6+} on the Pourbaix diagram, and that agrees with the onset of transpassive range of Alloy 600 from the polarization curve.

It is noticed that the general behavior of Alloy 600 in Zn containing solution is identical to that in the Zn free solution. The corrosion behavior is observed at around -750 mV $_{SHE}$. Hydrogen reduction reaction is observed below the corrosion potential, whereas oxidation of Ni, Cr, and Fe as well as passivation of the alloy takes place below -31 mV $_{SHE}$. Transpassive behavior is observed at potentials above that potential as current increases.

The current density of Alloy 600 in Zn free and Zn containing solutions are also close to each other. The complete potentiodynamic results of multiple tests are shown in Figure A-1 in the Appendix.

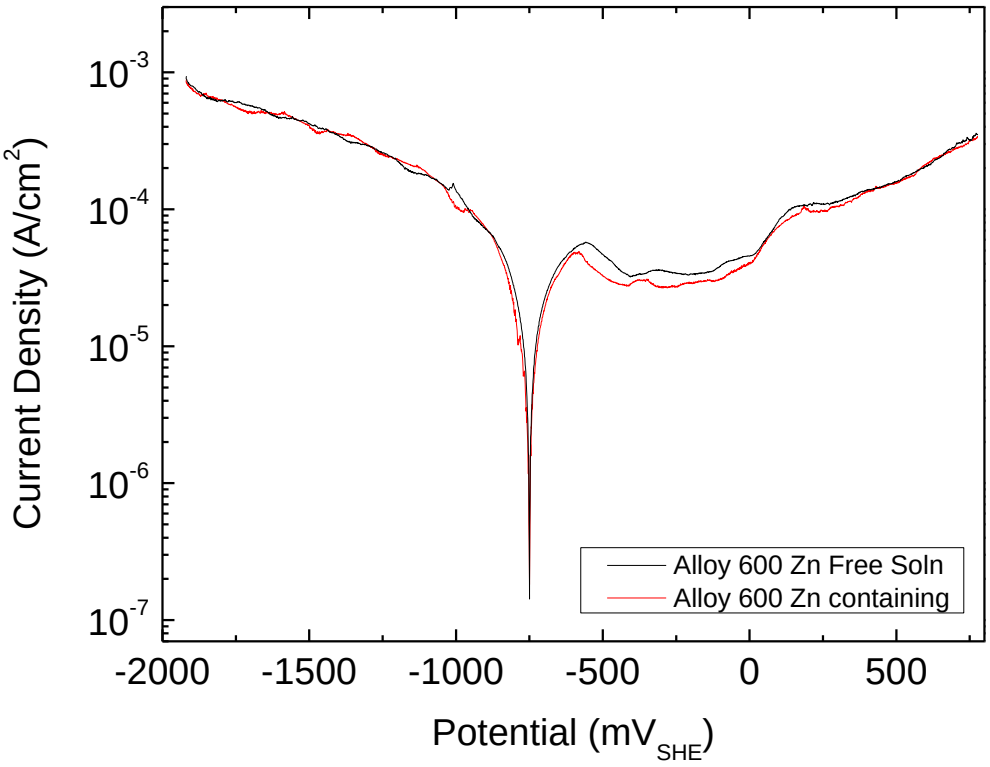

Figure 4-1: Example of polarization of Alloy 600 in both Zn free and Zn containing primary water containing 1200ppm B, 2ppm Li at 320 °C 1800psi. Each test was conducted from low potential to high potential at 1mV/s scan rate. The pH of the solution was calculated to be 7.28 at 320 °C.

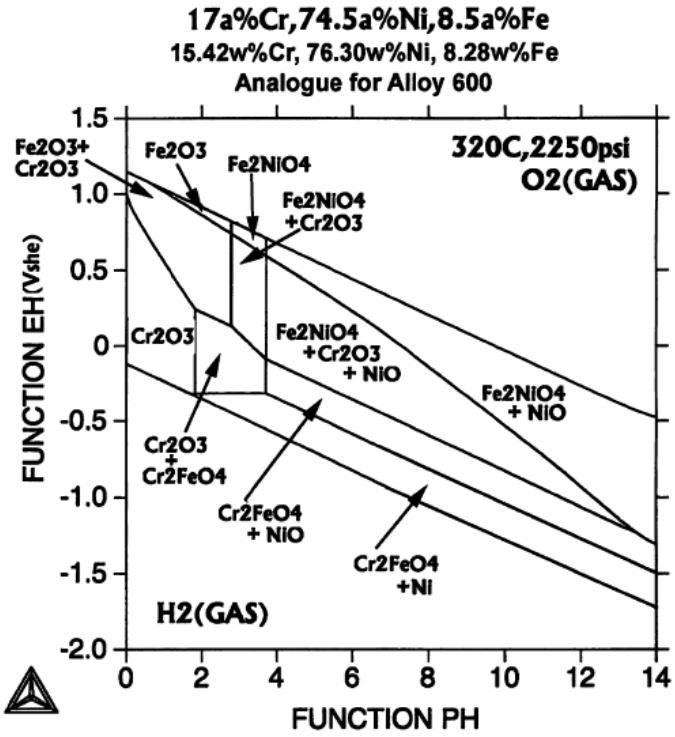

Figure 4-2: Pourbaix Diagram of Alloy 600 at 320°C and 2250psi in water containing H_3BO_3 and LiOH constructed by Kaufman [35].

4.2 Potentiostatic Polarization on Alloy 600

According to the polarization curve and Pourbaix diagram, a range of potentials in the passive region (before Cr^{+3} oxidizes to Cr^{+6} at 0V $_{SHE}$ at pH≈7.3) from the corrosion potential (-750 mV $_{SHE}$) are selected for electrochemical impedance spectroscopy. Each measurement of impedance spectroscopy is conducted at a static potential after polarizing for 4 hrs.

The static current density vs potential plot is shown in Figure 4-3. For both Zn free and Zn containing solutions, the current values are observed to be much lower than the polarization curve shown in Figure 4-1, and that is due to the long polarization time, during which the passive films are becoming more protective. The current density can be divided into three ranges, (1) below -700 mV $_{SHE}$ where the average current density is below 0; (2) from -700 mV $_{SHE}$ to -500 mV $_{SHE}$ where current density stays in a steady low nano-amp/cm^2 range; (3) above -500 mV $_{SHE}$ where current increases dramatically in micro-amp/cm^2 range. In the first stage, negative external current indicates a larger cathodic current compared with the anodic current. In the second stage, the current stays relatively constant, due to the combined effect of a decrease in reduction reaction rate as well as the decrease in oxidation reaction rate. The switch from the second to the third stage may be a result of the change in oxidation of iron from Fe^{+2} to Fe^{+3}.

It is observed that at potentials below -500 mV $_{SHE}$, the current density of the alloy in Zn containing solution is very close to that in Zn free solution, with only a slight decrease in Zn containing solution. This suggests that the film formed in Zn containing solution at this potential

range has a very similar passivity to that formed in Zn free solution. At potentials above -500 mV $_{SHE}$, the current density for Alloy 600 in Zn containing solution is significantly lower than in Zn free solution. Besides, the difference between current density in Zn free and Zn containing solutions gets larger, indicating that the difference in passivity between Zn free and Zn containing increases with potential.

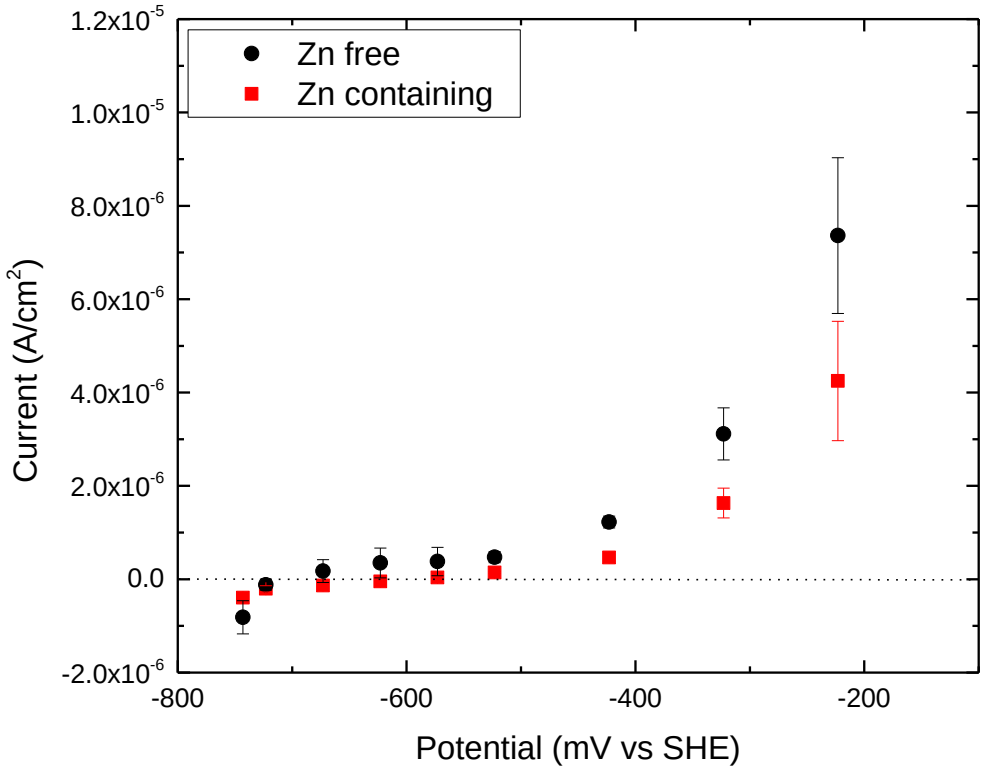

Figure 4-3: I-V relationship for Alloy 600 in Zn containing and Zn free solution oxidized for 4 hrs. at each potential for three different runs. Error bars represent the standard error between three sets of tests at each potential.

4.3 Electrochemical Impedance Spectroscopy for Alloy 600

4.3.1 EIS results and observation in Zn free and Zn containing Solution

The overall electrochemical impedance spectroscopy for Alloy 600 in Zn free and Zn containing solutions from -743 mV $_{SHE}$ to -223 mV $_{SHE}$ is shown in Figure 4-4 and Figure 4-5, in which the Bode plots, phase angle plots and Nyquist plots are all presented.

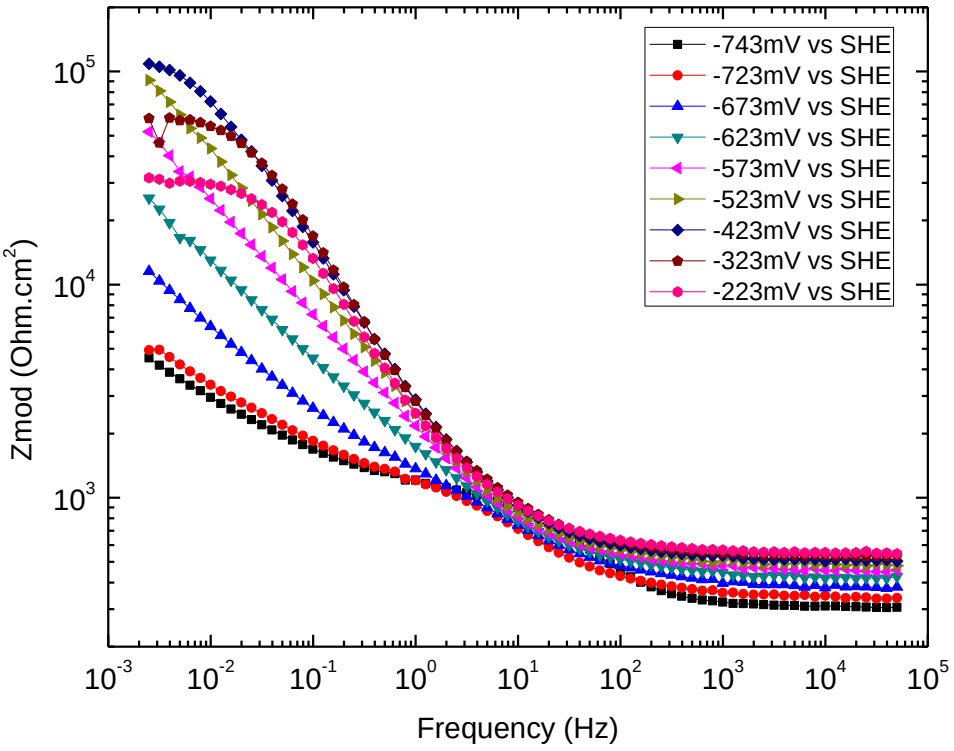
Zmod (Ohm.cm^2)
Frequency (Hz)
-743mV vs SHE
-723mV vs SHE
-673mV vs SHE
-623mV vs SHE
-573mV vs SHE
-523mV vs SHE
-423mV vs SHE
-323mV vs SHE
-223mV vs SHE

a)

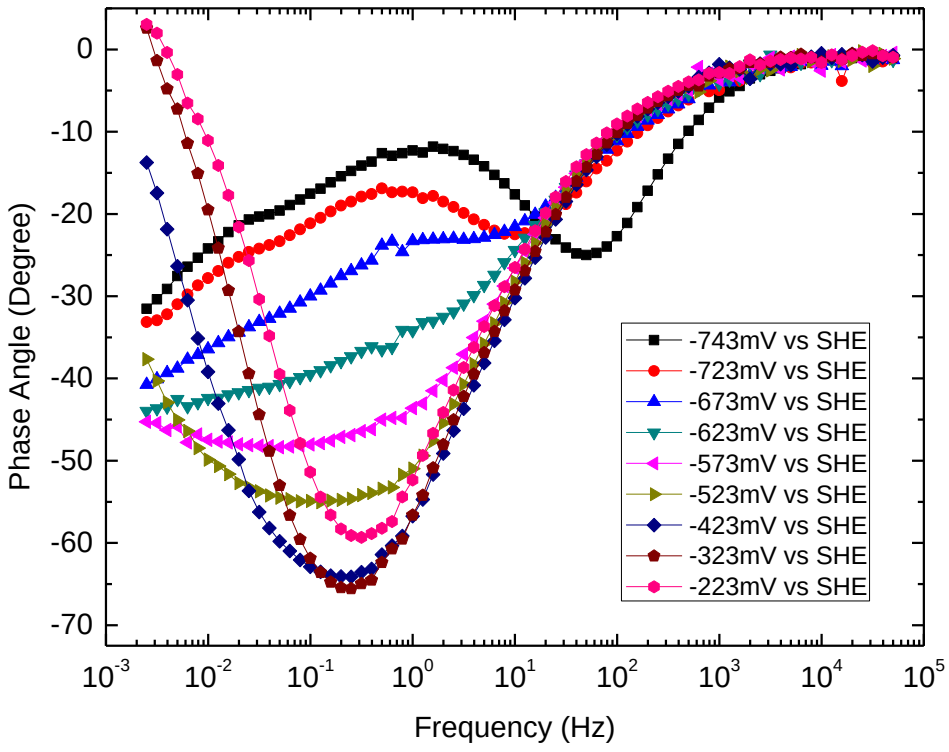
Phase Angle (Degree)
Frequency (Hz)
-743mV vs SHE
-723mV vs SHE
-673mV vs SHE
-623mV vs SHE
-573mV vs SHE
-523mV vs SHE
-423mV vs SHE
-323mV vs SHE
-223mV vs SHE

b)

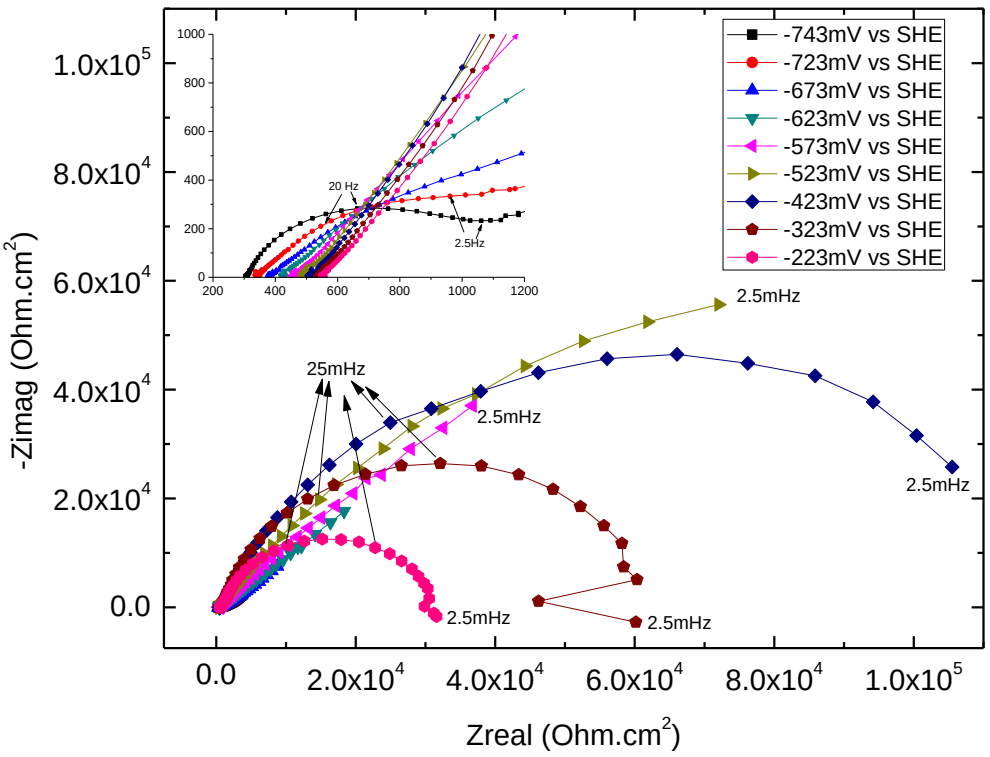

c)

Figure 4-4: a) Bode plot, b) phase angle plot, c) Nyquist plot for Alloy 600 in Zn free solution at 320°C and 1800psi. Each impedance spectrum was obtained after 4-hr. static polarization.

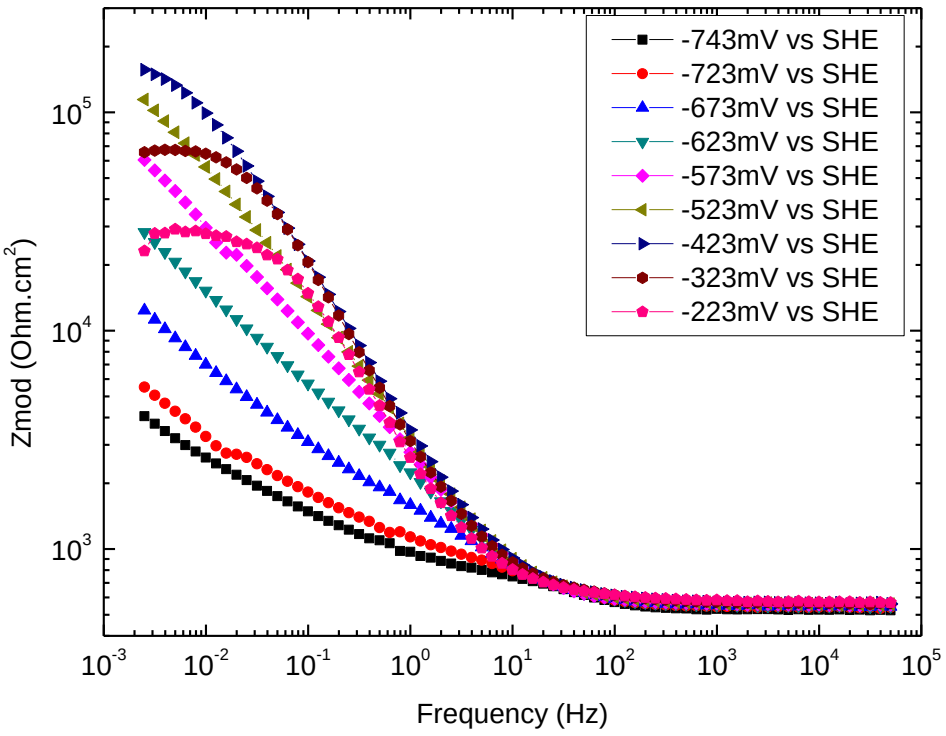
-743mV vs SHE
-723mV vs SHE
-673mV vs SHE
-623mV vs SHE
-573mV vs SHE
-523mV vs SHE
-423mV vs SHE
-323mV vs SHE
-223mV vs SHE
Zmod (Ohm.cm2)
Frequency (Hz)

(a)

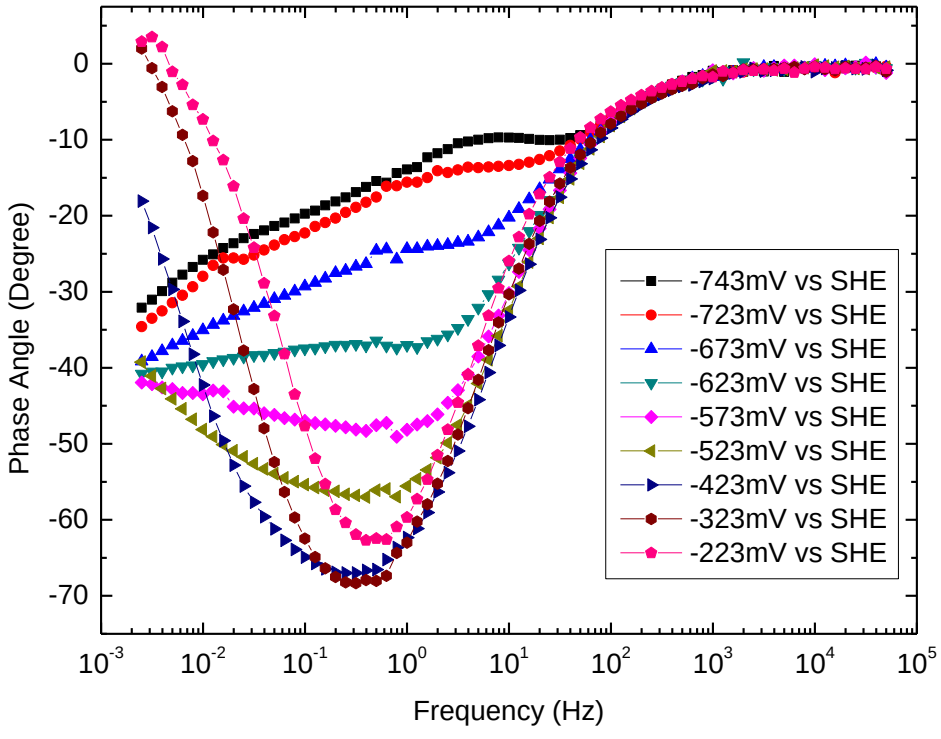
-743mV vs SHE
-723mV vs SHE
-673mV vs SHE
-623mV vs SHE
-573mV vs SHE
-523mV vs SHE
-423mV vs SHE
-323mV vs SHE
-223mV vs SHE
Phase Angle (Degree)
Frequency (Hz)

(b)

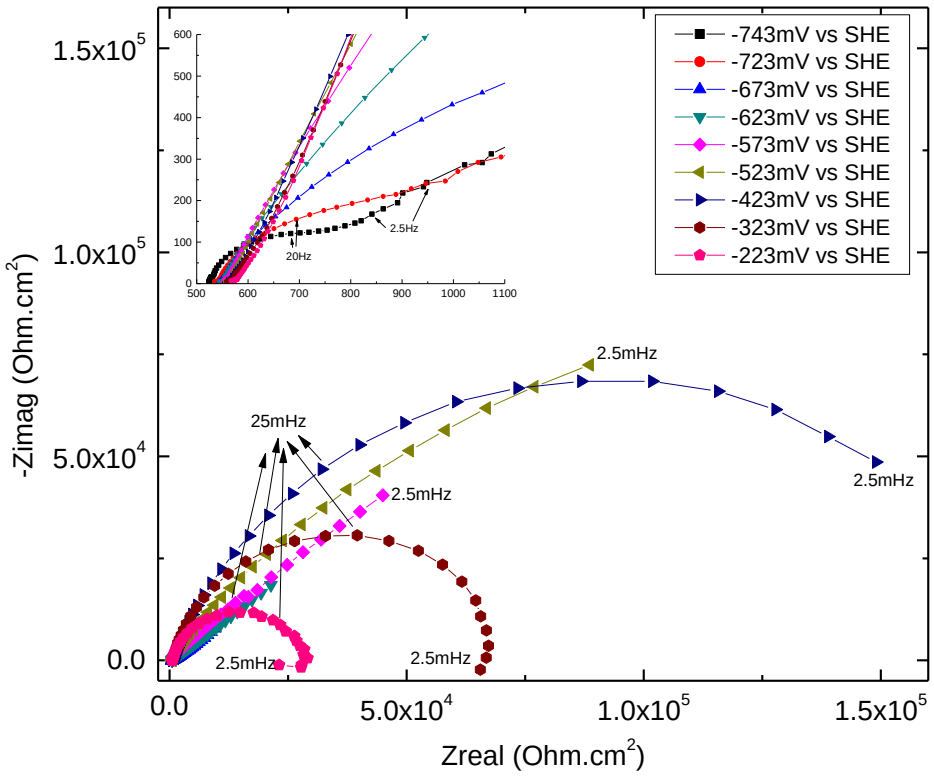

(c)

Figure 4-5: a) Bode plot, b) phase angle plot, c) Nyquist plot for Alloy 600 in Zn containing solution at 320°C and 1800psi. Each impedance spectrum was obtained after 4-hr static polarization.

It is observed that the impedance behavior of Alloy 600 in Zn free and Zn containing solutions are nearly identical with respect to change with potentials and comparative values, suggesting the passivity of Alloy 600 does not change significantly between Zn free and Zn containing solutions with 4 hrs. of oxidation. The effect of Zn on kinetics of the oxidation process will be analyzed through EIS modeling.

Generally, the overall impedance for Alloy 600 increases with potential below -500 mV $_{SHE}$, indicating the film gets more protective with increasing potential. At potentials below -500 mV $_{SHE}$, the Nyquist plots and phase angle plots indicate that the alloy undergoes a general corrosion process, including both capacitive responses from the oxide at higher frequencies and from electric double layer at lower frequencies, and a mass transfer process at low frequencies (given that low frequency phase angles are close to 45º), similar to what is described by several researchers [31], [32], [38]. A capacitive arc is apparent at potentials below -700 mV $_{SHE}$ at frequency above 2.5Hz, and the arc gradually diminishes with potential. This can be associated with hydrogen reduction reaction given the fact that current is below or close to zero in this potential range. Phase angle values increase with potential in mid-frequency range, indicating a more capacitive behavior of the film. The additional phase angle local maxima as well as changes in slopes indicate processes that can be related with the double layer and the film that can have overlapping time constants.

At potentials above -500 mV $_{SHE}$, only the capacitive element related to the film and double layer is observed and no diffusion process at low frequency is observed. Although only one capacitive arc is seen in the Nyquist plot, there may be several time constants that have similar characteristic frequencies that can only be differentiated through modeling indicating different parts of the film. Qiu et al. [32] also indicate that over time, the two capacitive arcs representing the outer layer and inner layer formed on Alloy 600 can merge into one capacitive arc. The decrease in impedance and phase angle maximum with potential indicates that the film becomes less protective, and this is usually related with a further oxidation process which can create more charge carriers. As described in previous sections, further oxidation of iron could lead to higher rate of charge transfer reactions.

It is also noted that at frequencies above 1000Hz, both the Bode plot and Nyquist plot show a consistent change in impedance values with potentials. According to Orazem [39], this impedance behavior contains information about the solution/outer layer behavior. Since the solution chemistry is well-controlled during the experiment, the fact that the impedance modulus in this region increases with potential suggests that there is an outer oxide layer that has a high characteristic frequency that is above the limit of detection range. The capacitance related to the outer oxide is likely to be very small which suggests the outer oxide is very porous.

4.3.2 Validation of Impedance Results

As indicated by several researchers [40], [41], before an impedance data set can be analyzed using linear models or equivalent circuits, four properties of impedance need to be satisfied in order to prove the data is valid: linearity, causality, steady state and finiteness. The impedance results need to be finite and causal, meaning one-to-one correspondence between frequency and measured real and imaginary values. The causality and linearity can be verified by the Kramers-Kronig transformation (KKT), which mathematically calculates the real part from the imaginary part, and vice versa. If KKT is satisfied, it confirms that the system follows the Linear System Theory (LST). Figure 4-6 (a) shows the KKT results conducted with Gamry Echem Analyst software on a sample oxidized at -743 mV $_{SHE}$ for 4 hrs. It is observed that the transformed values have very good agreement with the experimental values, with an error of 0.016‰. All other impedance measurements used in this study are all validated with KKT, in which the errors are kept below 0.5‰.

Although the system is dynamic with the oxide film growing over time, it is important to make sure that the system is under steady state for the impedance to be valid. An assumption is made that the film is at steady state during each impedance measurement, during which film growth is minimal that current density and film thickness are independent of time. One way to verify the steady state of the system is to conduct the impedance measurement from both high frequency and from low frequency, as is described by Lv et al. [42]. Figure 4-6 (b) shows the impedance results from both forward (high frequency to low frequency) and reverse (low frequency to high frequency) scans for Alloy 600 oxidized at -743 mV $_{SHE}$ in Zn containing solution. The results from the two scanning directions agree well with each other, although a better alignment would be achieved with longer oxidation time. Since the alloy has the lowest rate of oxidation at -743 mV $_{SHE}$, oxidation at higher potentials for the same amount of time would form a more steady film, and the system is expected to be at steady state at higher potentials.

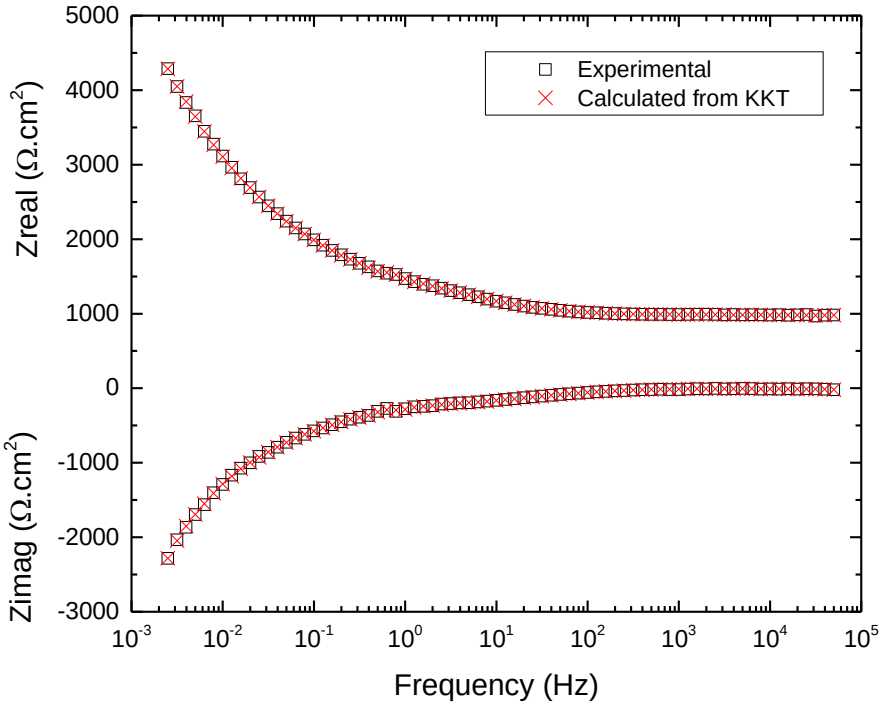
Experimental
Calculated from KKT
Zreal (Ω.cm²)
Zimag (Ω.cm²)
Frequency (Hz)
5000
4000
3000
2000
1000
0
-1000
-2000
-3000
10⁻³
10⁻²
10⁻¹
10⁰
10¹
10²
10³
10⁴
10⁵

(a)

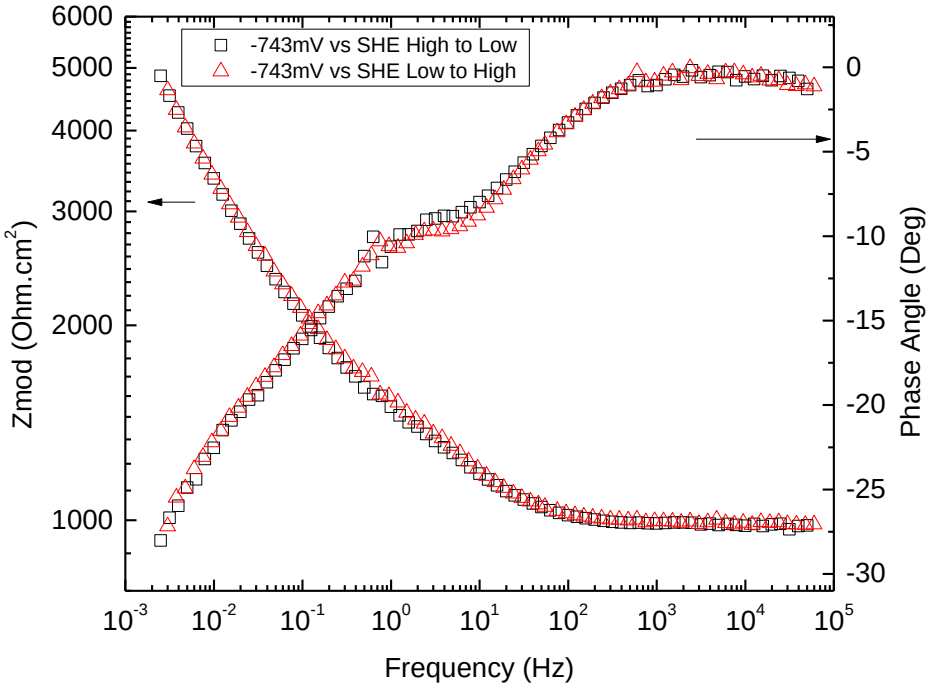

(b)

Figure 4-6: (a) Kramers-Kronig transformation, and (b) results with 2 scanning directions: high-to-low and low-to-high for Alloy 600 oxidized at -743 mV $_{SHE}$ for 4hrs in Zn containing PW water at 320 °C and 1800 psi.

4.3.3 EIS Equivalent Circuit

4.3.3.1 Model Construction

The EIS equivalent circuit is constructed based on the TEM results that are described in the previous chapter. It is observed from the TEM results that a Cr-rich inner layer and a Ni/Fe-rich outer layer are both present on Alloy 600 in both Zn free and Zn containing solutions, so the equivalent circuit has a general form of R_S-Z_{OL}-Z_{IL}.

A parallel RC circuit, a general circuit element, is used for the outer layer [26], [31], [32], [43], [44]. As described in the previous section, the outer layer either contains whiskers that are up to 5-um long in Zn free solution, or particles that may cluster to form a large thickness up to 1.5 um. Therefore, a rough calculation for outer oxide capacitance can be conducted using the equation $C = \frac{\varepsilon_0 \varepsilon_r A}{d}$, in which ε_o is the permittivity of vacuum, ε_r is the relative permittivity of the oxide, A is the effective area on the surface, and d is the thickness of the outer oxide. According to Macak et al. [38], the relative permittivity for oxides grown in high temperature water is used, as ε_r=12. Using the length of the longest whisker measured to be 5um and largest octahedral particle measured to be 500nm, the area normalized capacitance of the outer oxides can be calculated to be 2.1nF/cm^2 for Zn free solution, and 21 nF/cm^2 for Zn containing solution. These values are used as initial numbers for optimization of the data.

The rest of the equivalent circuit is constructed based on reactions that take place on the metal surface. Both the point defect model (PDM) [37], [44], [45] and the mixed potential model (MCM) [46]–[48] describe the reactions that may take place on the passivated alloy. A generalized schematic illustrating the expected process is shown in Figure 4-7, which involves processes of metal oxidation (generating oxygen vacancies), oxygen injection from water molecule (creating metal vacancies and annihilating oxygen vacancies), oxygen transport, oxide dissolution, metal transport, and possible hydrogen reduction reaction. The film formation is related with metal oxidation, oxygen injection and metal dissolution. Because the film is found to be rich in Cr_2O_3, the assumption is made there is only one type of cation vacancy, which is the chromium vacancies.

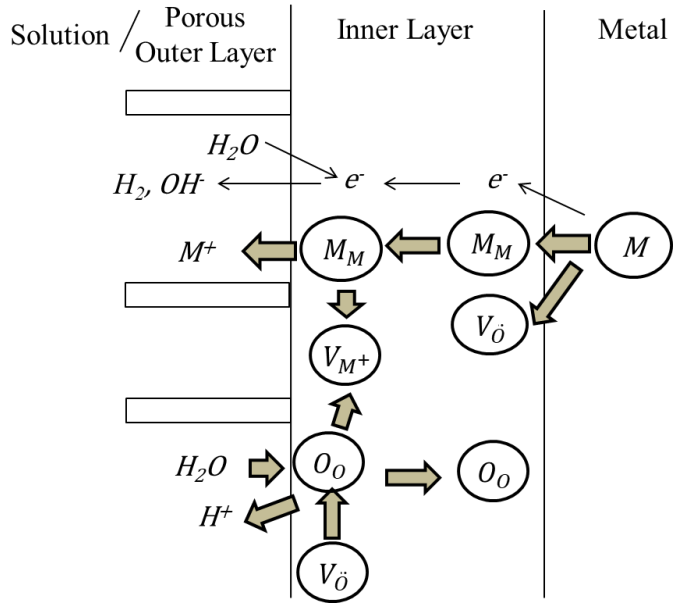

Figure 4-7: Schematic illustration of possible reactions and transport through the passive film based on PDM and MCM.

The impedance of the inner layer is composed of two parts, inner layer/outer layer (IL/OL) interface, where oxygen incorporation and metal dissolution occurs, and alloy/innerlayer (M/IL) interface, where metal oxidation takes place. Diffusion takes place between the two interfaces.

$$Z_{IL} = Z_{OL/IL} + Z_{M/IL} \qquad (7)$$

The general form of the equivalent circuit for the inner layer with the IL/OL interfaces is shown in Figure 4-8 (a). The total current at any potential is the sum of the currents associated with the oxidation and reduction reactions, and charging/discharging of capacitive phenomena at oxide film or double layer,

$$i_{total} = i_{ox} + i_{red} + i_{cap} \qquad (8)$$

As a result, the impedance at any given potential, involves elements Z_{ox}, Z_{red} and Z_{cap} in parallel. It also indicates that the current that goes through the metal/solution interface can either introduce oxygen incorporation/ metal dissolution, reduce the species in the solution, or charge/discharge interface. Both Z_{ox} and Z_{red} are developed through a Randles circuit, a typical

circuit describing an electrochemical reaction involving both the charge transfer resistance representing the Faraday effect and a Warburg element representing the mass transport process. Warburg element is represented with $Z_w = \frac{\sigma}{\sqrt{\omega}}(1-j)$, in which σ is the Warburg coefficient, and ω is angular frequency. The combined inner layer circuit is shown in Figure 4-8 (b).

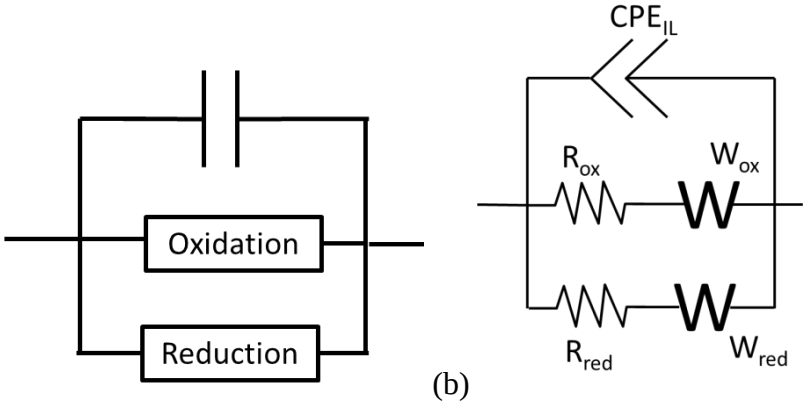

(a) (b)

Figure 4-8: (a) circuit element to start with. (b) Circuit elements representing reactions at the inner layer interfaces and transport through inner layer

Regarding oxygen incorporation/ metal dissolution, R_{ox} represents the total resistance of film formation at the IL/OL interface, including metal dissolution reaction,

$$M_{Cr}^{\delta-} \overset{k_1}{\rightarrow} M_{(aq)}^{(3-\delta)+} + V_{Cr}^{3-} \qquad (9)$$

and oxygen injection,

$$V_o^{2+} + H_2O \overset{k_2}{\rightarrow} O_O + 2H^+ \qquad (10)$$

The total rate related with these two reactions can be a function of rate constants k_1 and k_2, and $i_{ox} = F(ak_1 + bk_2)$, in which F is the Faraday constant, a and b are constants, k_1 and k_2 can be functions of potentials and surface ion concentration. As a result, the resistance R_{ox} related with the film formation at IL/OL interface is inversely related with i_{ox}, i.e., k_1 and k_2. W_{ox} (as well as Warburg coefficient, σ) is associated with ion transport, such as oxygen anion diffusion and cation transport (both through vacancies) through the inner layer associated with the reactions described above.

Hydrogen reduction reaction is associated with the reduction reaction happening in the system,

$$2H_2O + 2e^- \rightarrow H_2 + 2OH^-. \qquad (11)$$

R_{red} is the charge transfer resistance for the reaction, and W_{red} is related with the mass transport for this reaction that can be either H_2 or OH^- transport. As is discussed in the previous chapter, Ni reduction could take place in the oxide at potentials close to the Ni/NiO equilibrium potential, creating a Ni-rich metallic layer, $NiCr_2O_4 + H_2 \rightarrow Ni + Cr_2O_3 + H_2O$. Thus the Warburg coefficient W_{red} is related with H_2 transport.

The constant phase element represents the spatial capacitance of the inner layer. A constant phase element CPE ($Z = \frac{1}{Y_o(j\omega)^{\alpha}}$) is used instead of a perfect capacitor, representing the possible dispersion of time constants at the inner layer, which could be a result of imperfection of the surface.

In this case the total impedance of the IL/OL interface is represented by

$$\frac{1}{Z_{OL/IL}} = \frac{1}{Z_{cap}} + \frac{1}{Z_{ox}} + \frac{1}{Z_{red}} \qquad (12)$$

$$\frac{1}{Z_{OL/IL}} = Y_{o_{IL}}(j\omega)^{\alpha_{IL}} + \frac{1}{R_{ox}+\frac{\sigma_{ox}}{\sqrt{\omega}}(1-j)} + \frac{1}{R_{red}+\frac{\sigma_{red}}{\sqrt{\omega}}(1-j)} \qquad (13)$$

In order to describe the alloy/IL interface, an extra parallel RC element is added in series with the OL/IL interface.

$$\frac{1}{Z_{M/IL}} = \frac{1}{Z_{sc}} + \frac{1}{R_M} \qquad (14)$$

The resistance R_M is associated with the reactions

$$M \overset{k_3}{\rightarrow} M_{Cr}^{\delta-} + \frac{3}{2}V_O^{2+} + (3-\delta)e^- \qquad (15)$$

and

$$M + V_{Cr}^{3-} \overset{k_4}{\rightarrow} M_{Cr}^{\delta-} + (3-\delta)e^- \qquad (16)$$

Similar to what is described for R_{ox}, R_M is inversely related to k_3 and k_4. Z_{SC} is associated with the charging/ discharging of the double layer for the metal oxidation reaction. A CPE is also used for Z_{SC} instead of a perfect capacitor in order to compensate for the dispersion of time constants at the interface, in which Yo_{SC} is the pre-exponential term of the constant phase element, whereas α_{SC} is the exponential term of the constant phase element

$$\frac{1}{Z_{M/IL}} = Y_{o_{SC}}(j\omega)^{\alpha_{SC}} + \frac{1}{R_M} \qquad (17)$$

4.3.3.2 Modification of the Model

Since the impedance behavior for Alloy 600 in both Zn free and Zn containing solutions are similar, results in Zn free solution are used to illustrate the development and general fitting of the equivalent circuit.

4.3.3.2.1 Low Potential Region (-750 mV $_{SHE}$ to -600 mV $_{SHE}$)

Based on the above discussion, the initial impedance model is shown in Figure 4-9 (a). One of the datasets measured at -723 mV $_{SHE}$ in Zn free solution is used to show the fitting results. The fitting result of the Bode plot is shown in Figure 4-9 (b). It can be observed that the fitting curve follows the general trend of the impedance curve, including time constant at around 40mHz.

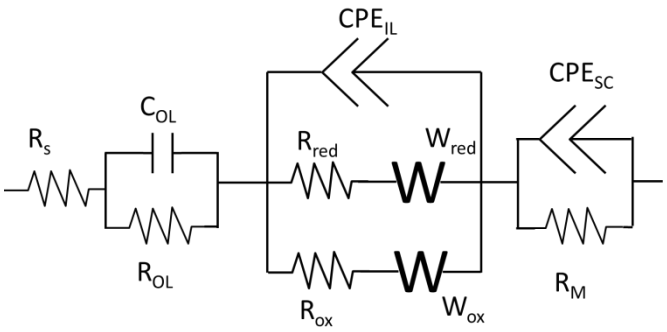

(a)

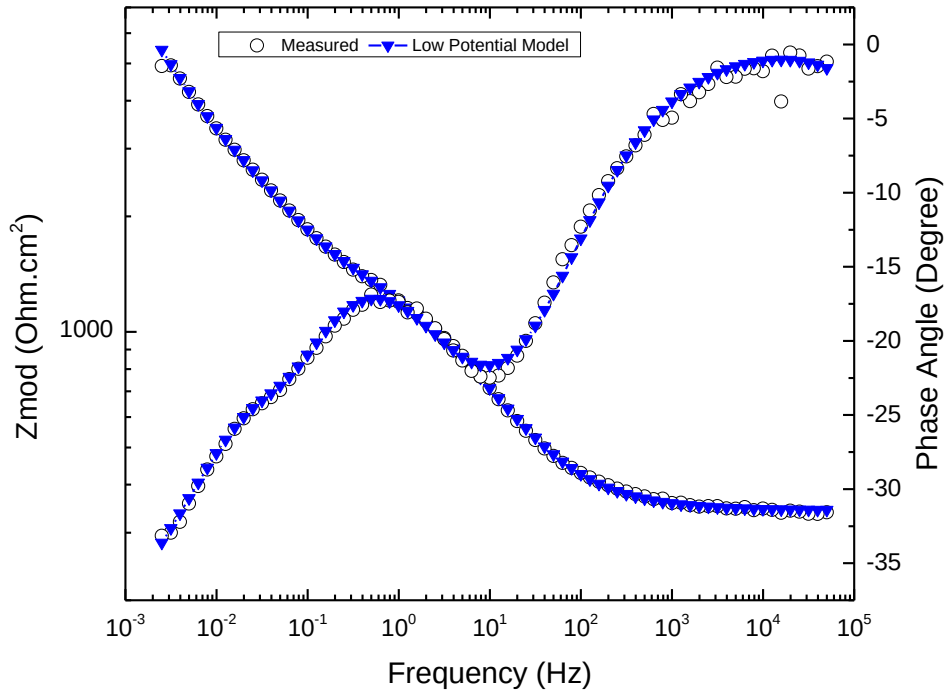

(b)

Figure 4-9: (a) Equivalent circuit for potentials -750 mV $_{SHE}$ to -600 mV $_{SHE}$ (b) Example of fitting results with this model at -723 mV $_{SHE}$

4.3.3.2.2 Mid Potential Region (-600 mV $_{SHE}$ to -500 mV $_{SHE}$)

The equivalent circuit in this potential range is very similar to the one in the low potential region, except that there is no circuit element representing the diffusion process of the reduction reaction (Warburg element). The reason for eliminating the Warburg element is not only to obtain a better fitting, but also because this potential range is at least 150 mV above the corrosion potential. At this potential range, the cathodic current should be very small compared to the anodic current. As the impedance related to the reduction reaction increases exponentially with potential, the impedance related with the diffusion process increases at a lower factor. Eventually, in this potential range when the rate of charge transfer reaction is very low compared

to that for transport process, $Z_{CTR\_red} >> Z_{W\_red}$ and the Warburg element can be eliminated. The resistance related to the cathodic charge transfer reaction is still present in the equivalent circuit because the total current in this range is around the same as the lower potentials in the nano-amp/cm^2 range. The model used is shown in Figure 4-10 (a) and an example of the fitting is shown in Figure 4-10 (b).

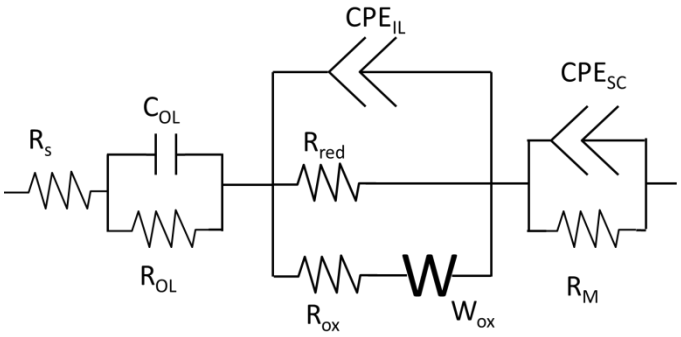

(a)

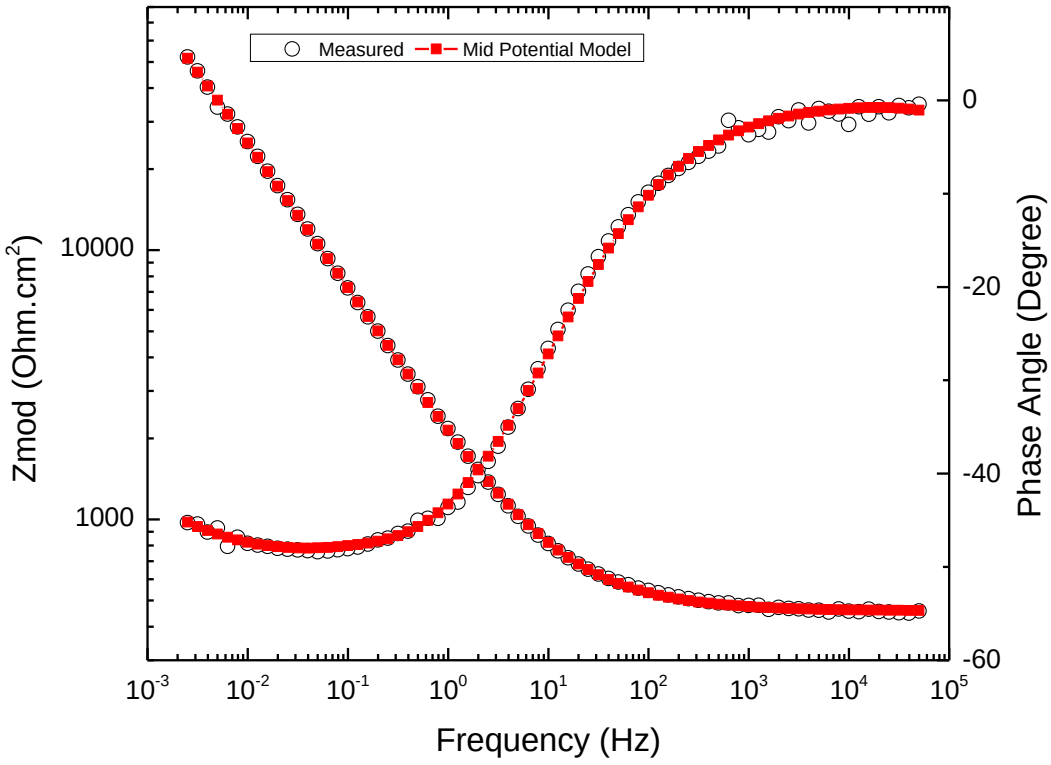

(b)

Figure 4-10: (a) Equivalent circuit model for potentials -600 mV $_{SHE}$ to -500 mV $_{SHE}$. (b) Example of fitting at potential -573 mV $_{SHE}$.

4.3.3.2.3 High Potential Region (-500 mV $_{SHE}$ to -200 mV $_{SHE}$)

There are several changes for the equivalent circuit in the high potential region. Because the potential is so high above the corrosion potential (~-750 mV $_{SHE}$), the rate of cathodic reaction would be so low that it is believed to not have any significant effect on the total current at potentials in this range. Therefore the charge transfer resistance for the hydrogen reduction reaction is removed. As is discussed earlier, no Warburg impedance is observed at low frequency in phase angle plot for this potential range. The inner layer representation becomes a simple RC circuit. Also, instead of having only RC circuit elements for the intermediate layer in the lower potentials' equivalent circuit, extra circuit elements of an inductor and a resistor are added to the circuit in parallel with the original RC circuit. These elements represent the adsorption process taking place at the solution/film interface. According to the Pourbaix diagram of Alloy 600, reactions of $Fe^{2+} \rightarrow Fe^{3+} + e^{-}$ should take place, and thus Fe^{3+} is likely to be adsorbed on the film/solution interface. Besides, the TEM results show that there is a continuous planar film, which can have a continuous double layer that promotes the adsorption of Ni^{2+}, Cr^{3+}, and Fe^{3+} cations on the surface. The circuit is shown in Figure 4-11 (a), and an example of fitting is shown in Figure 4-11 (b).

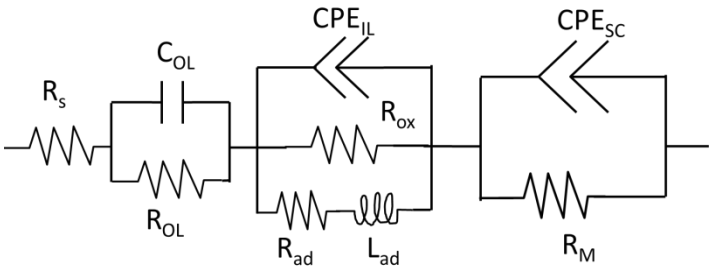

(a)

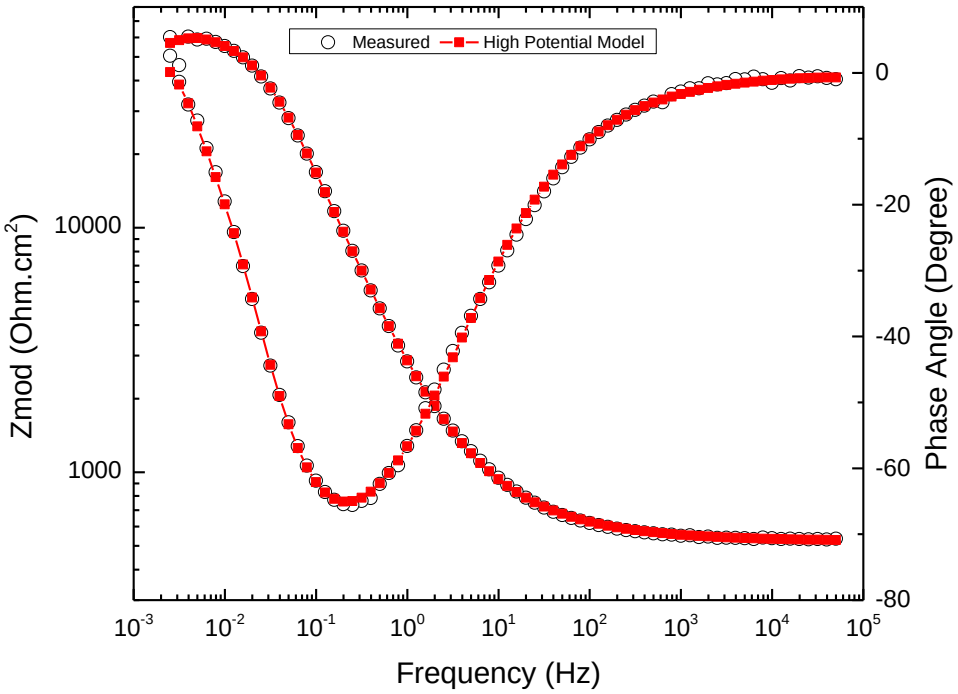

(b)

Figure 4-11: (a) Equivalent circuit model for potentials between -500 mV $_{SHE}$ and -200 mV $_{SHE}$. (b) Example of fitting at –potential 323 mV $_{SHE}$.

4.3.4 Fitting Results for Zn containing and Zn free Solutions

The fitting results of Zn free and Zn containing solutions are shown in Figure 4-12 and Figure 4-13. It is observed that the models described above can fit the data very well. The fitting parameters are shown below in Table 4-1. The goodness of all the fittings are kept below $3*10^{-4}$. It is observed that among all the parameters, the largest difference between Zn free and Zn containing conditions is R_{ox} at low potentials. The parameters will be discussed in the next chapter as well as a proposed film formation mechanism.

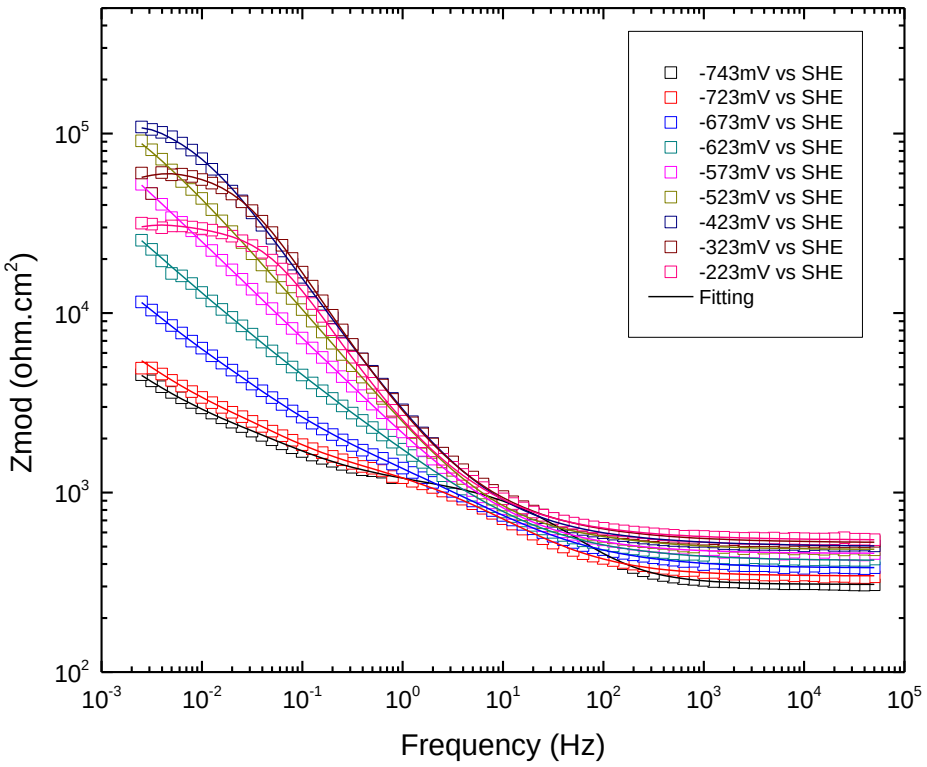
-743mV vs SHE
-723mV vs SHE
-673mV vs SHE
-623mV vs SHE
-573mV vs SHE
-523mV vs SHE
-423mV vs SHE
-323mV vs SHE
-223mV vs SHE
Fitting
Zmod (ohm.cm2)
Frequency (Hz)
10^5
10^4
10^3
10^2
10^-3
10^-2
10^-1
10^0
10^1
10^2
10^3
10^4
10^5

(a)

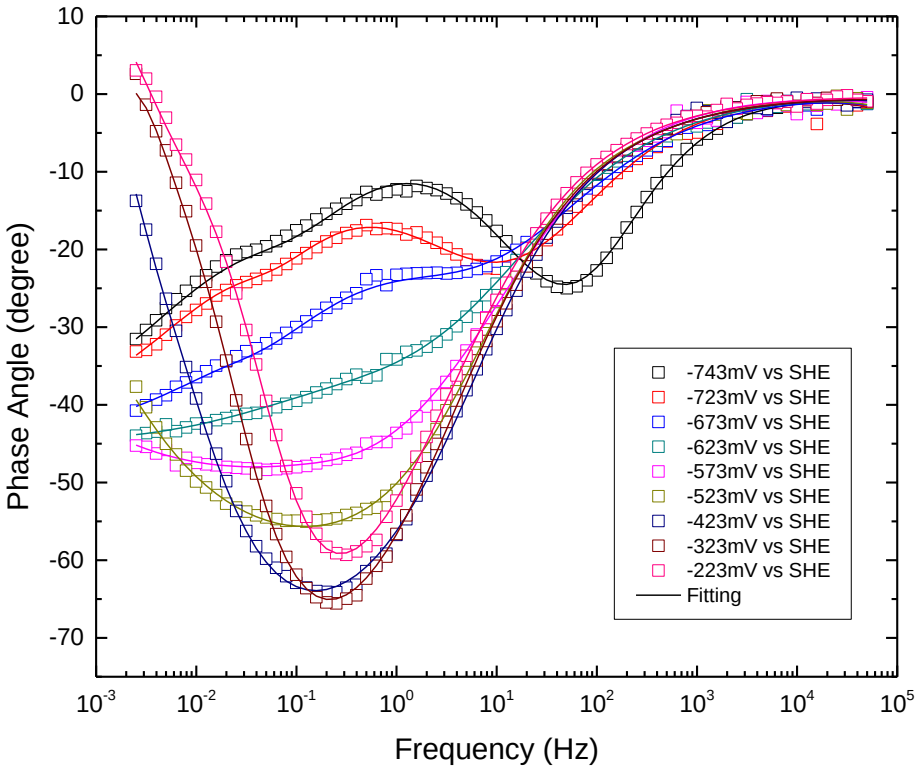

(b)

Figure 4-12: (a) Impedance modulus and (b) Phase angle fitting for Alloy 600 in Zn free primary water at 320 ºC and 1800psi. Points- Experimental values. Solid lines- Curve fitting

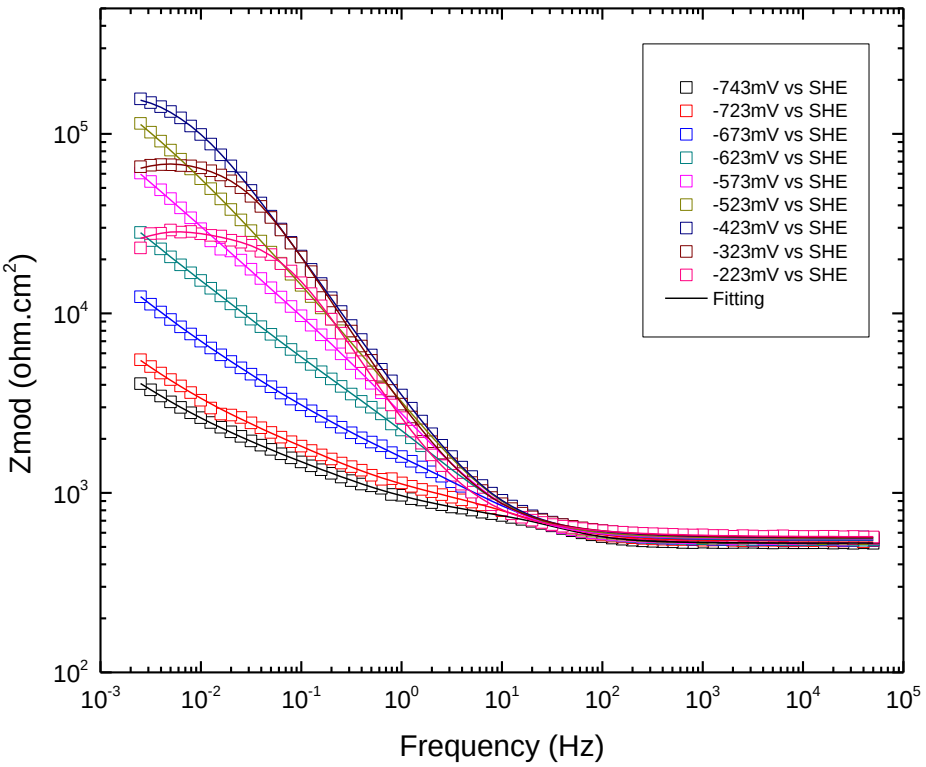
-743mV vs SHE
-723mV vs SHE
-673mV vs SHE
-623mV vs SHE
-573mV vs SHE
-523mV vs SHE
-423mV vs SHE
-323mV vs SHE
-223mV vs SHE
Fitting
Zmod (ohm.cm2)
Frequency (Hz)
10^5
10^4
10^3
10^2
10^-3
10^-2
10^-1
10^0
10^1
10^2
10^3
10^4
10^5

(a)

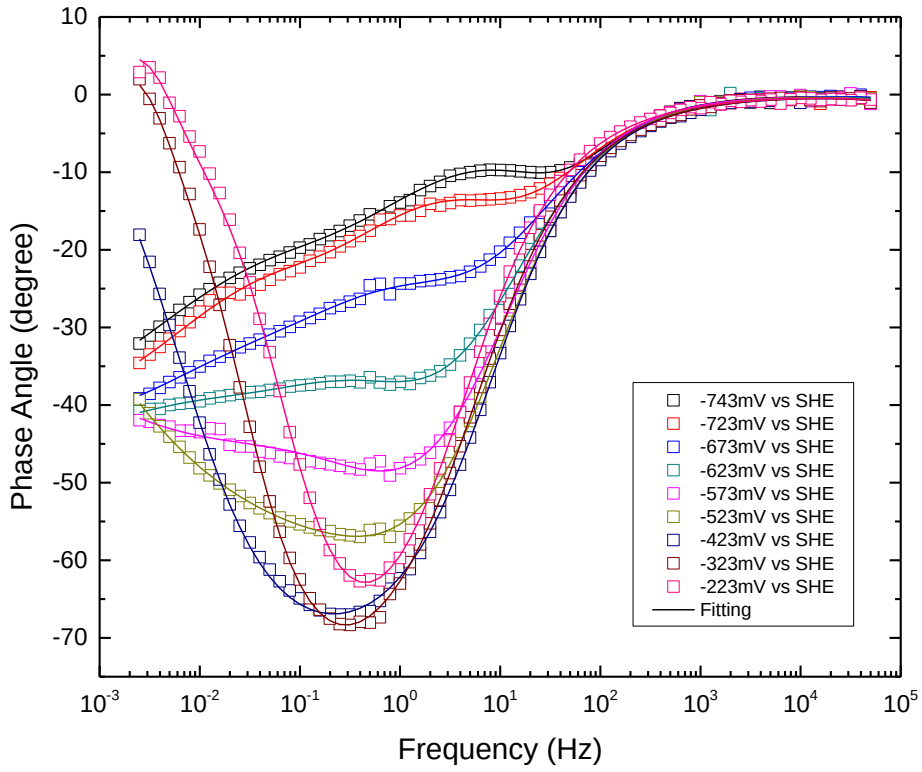

(b)

Figure 4-13: (a) Impedance modulus and (b) Phase angle fitting for Alloy 600 in 0.1ppm Zn containing primary water at 320 ºC and 1800psi. Points- Experimental values. Solid lines- Curve fitting

Table 4-1:One data set of fitting parameters for Alloy 600 in Zn free and Zn containing Solutions. The goodness of fitting for all fittings is kept below all $3*10^{-4}$.

Potential (mV $_{SHE}$)	-743	-723	-673	-623	-573	-523	-423	-323	-223
Zn Free									
Yo_{IL} ($*10^{-6}$ $S.s^a/cm^2$)	21	44	31	45	97	105	502	285	296
α_{IL}	0.82	0.75	0.73	0.70	0.66	0.72	0.46	0.51	0.52
R_{red} ($\Omega.cm^2$)	845	1118	1565	7190	702700	247300			
σ_{red} ($\Omega.s\text{-}1/2.cm^2$)	418	565	1718	8045					
R_{ox} ($\Omega.cm^2$)	1503	54	39	56	140	1460	147900	23870	11540
σ_{ox} ($\Omega.s^{-1/2}.cm^2$)	30628	8643	5643	5171	9794	34650			
R_{OL} ($\Omega.cm^2$)	277	285	313	366	387	339	472	495	513
C_{OL} (pF/cm^2)	307	315	223	108	134	240	39	21	39
R_M ($\Omega.cm^2$)	396	262	222	3298	1081	65	105500	47790	22210
Yo_{SC} ($S.s^a/cm^2$)	0.00504	0.01280	0.02132	0.01396	0.00297	0.00020	$1.1*10^{-4}$	$1.1*10^{-4}$	$1.4*10^{-4}$
α_{SC}	0.83	1.00	1.00	0.56	0.70	0.61	0.85	0.97	0.97
R_{ad} ($\Omega.cm^2$)							122.8	61.19	60.53
L_{ad} ($*10^5$ $H.cm^2$)							10.3	9.6	8.5
Zn Containing									
Yo_{IL} ($*10^{-6}$ $S.s^a/cm^2$)	41	83	100	104	83	78	1792	310	527

α_{IL}	0.88	0.78	0.74	0.74	0.83	0.84	0.44	0.59	0.54
R_{red} ($\Omega.cm^2$)	215	441	2058	8335	520600	412000			
σ_{red} ($\Omega.s\text{-}1/2.cm^2$)	476	644	11815	160359					
R_{ox} ($\Omega.cm^2$)	6682	3384	1278	2778	5917	10310	340400	17120	8227
σ_{ox} ($\Omega.s^{-1/2}.cm^2$)	1568	3487	1575	3445	8865	22999			
R_{OL} ($\Omega.cm^2$)	469	492	514	495	521	528	546	486	528
C_{OL} (pF/cm^2)	52	72	26	48	73	60	60	79	59
R_M ($\Omega.cm^2$)	503	611	964	3031	382	1599	178100	57780	22910
Yo_{SC} ($S.s^a/cm^2$)	0.002054	0.002032	0.002354	0.001589	0.000425	0.000532	$7.1*10^{-5}$	$8.6*10^{-5}$	$9.6*10^{-5}$
α_{SC}	0.60	0.67	0.61	0.63	0.67	0.60	0.82	0.96	0.95
R_{ad} ($\Omega.cm^2$)							2.4	48.7	86.8
L_{ad} ($*10^5$ $H.cm^2$)							2.3	6.7	2.9

Chapter 5. Discussion

5.1 Effect of Zn on the Alloy 600 Oxide Chemistry

5.1.1 Verification of Film Structure with DPA analysis

The combination of SEM, TEM and EDS indicates the surface film formed on Alloy 600 at -700 mV $_{SHE}$ in PWR PW at 320°C consists of a continuous, compact, inner layer of Cr_2O_3 and an outer layer that consists of nanowires/whiskers composed predominantly of NiO and a small amount of spinel. The observations are significantly different from the thermodynamic predictions. In particular, Kaufman indicates that the thermodynamically stable product of the oxidation of Alloy 600 in PWR PW at a potential of -700 mV $_{SHE}$ is a mixture of NiO, which is the dominant phase, and $FeCr_2O_4$. Most notably, Cr_2O_3 is not thermodynamically predicted. [35]

The discrepancy between the observed surface film and the thermodynamically stable oxidation products can be a result of kinetic factors, which in the early stages of oxidation exert a significant effect on the identity of the surface oxide. The influence of kinetics on the construction of the surface oxide is made apparent by diffusion path analyses (DPA) developed by Devine[49]. In particular, the nature of the surface oxide and the role of kinetics in determining its identity can be gleaned by plotting the composition of the alloy, the surface film and the aqueous solution on a pseudo-ternary (Ni, Fe)-Cr-Water phase diagram. The pseudo-ternary phase diagram for Alloy 600 in water at potentials between -750mV $_{SHE}$ and -500mV $_{SHE}$ is shown in Figure 5-1 as well as the results of the DPA analysis. According to TEM results, $(Ni_xFe_{1-x})O$, chromite spinel and Cr_2O_3 are present as oxide film. In order to confirm that the findings are valid kinetically, these three species need to be connected through a diffusion path. As shown in Figure 5-1, a diffusion path is successfully sketched that it starts with the bulk composition of Alloy 600, passes through Cr_2O_3, spinel and NiO, and terminates in the bulk water composition.

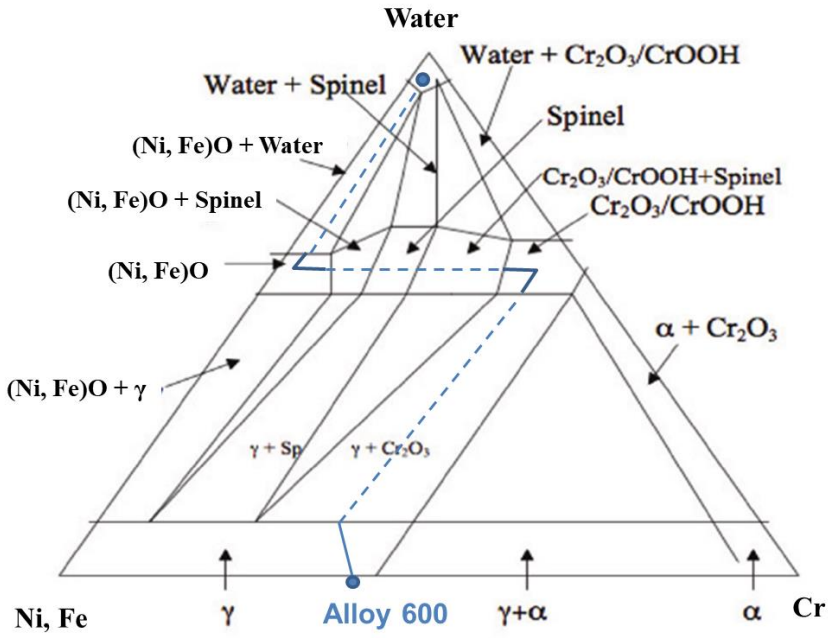

Figure 5-1: DPA analysis of Alloy 600 based on TEM results using (Ni,Fe)-Cr-Water pseudo-ternary phase diagram [49].

The TEM results clearly indicate the presence of the inner layer of Cr_2O_3 and the outer layer of NiO but the evidence for the presence of a layer of chromite spinel (e.g., $NiCr_2O_4$ and/or $FeCr_2O_4$) is subtle. In Chapter 3, the existence of chromite spinel is extrapolated by deconvoluting the signal across the inner layer. The chromite signal can also be found through the change in chromium concentration in the line scans. It is shown in several line scans (eg. Figure 3-8 (b)) at various potentials both in Zn free and Zn containing solutions that the shape of the plot of chromium concentration with distance along the line scan starting at the point of maximum concentration (i.e., in the inner layer) and extending in the direction of the outer layer exhibits two slopes. The first is attributed to the EDS signal emanating largely from the inner layer of Cr_2O_3 and the second is attributed to a separate layer that contains chromium but with a lower concentration than in Cr_2O_3. For instance, the chromium line scans presented in Figure 3-8 (b) were obtained from a sample that was polarized at – 700 mV $_{SHE}$ and exhibit the change in slope that is indicative of an oxide layer that lies on top of the inner layer of Cr_2O_3 and possesses a lower chromium concentration than does Cr_2O_3. The lower chromium-concentration oxide is assumed to be a chromite spinel because of earlier work that measured the Raman spectra of the surface films formed on Alloy 600 under similar conditions [21].

In summary, more than 2/3 of all the line scans at various potentials under different water chemistry exhibit evidence of a thin, lower chromium-concentration oxide layer adjacent to the inner layer of Cr_2O_3.

Besides the DPA analysis, the presence of chromite spinel can also be verified by earlier work measuring the *in-situ* Raman spectrum of the surface film formed on Alloy 600 in PWR PW [21]. Wang and Devine's work on Raman spectrum indicated the passive film consisted of a mixture

of Cr_2O_3 (and possibly NiO) and spinel $FeCr_2O_4$. The Raman spectrum clearly contained a peak at 670 cm^{-1}, which is the most intense peak of the Raman spectrum of a number of spinel oxides. The spinel was identified as $FeCr_2O_4$ rather than $NiCr_2O_4$ because no spinel was detected by Raman spectroscopy in the surface oxides formed on Ni-Cr binary alloys with 10 and 20% Cr.

In summary, the surface film that forms on Alloy 600 after immersion in PWR PW for several hours at potentials of -700 mV $_{SHE}$, -550 mV $_{SHE}$, and -223 mV $_{SHE}$ is significantly different from the thermodynamically stable oxidation products of Alloy 600 at these potentials. The most significant discrepancy is the presence of the inner layer of Cr_2O_3 at potentials below -500 mV $_{SHE}$. Its formation is likely a consequence of the greater reactivity of Cr compared to that of iron and nickel. The preferential oxidation of chromium creates an inner layer of Cr_2O_3 and a chromium-depleted zone in the alloy at the alloy/oxide interface. Continued oxidation of the alloy leads to thickening of the inner layer of Cr_2O_3 and the migration of the other oxidized cations, Fe^{+z} and Ni^{2+}, through the inner layer and into the aqueous solution that contacts the free surface of the inner layer. The iron and nickel cations have very limited solubility in PWR PW, resulting in the precipitation of solid products NiO and $NiFe_2O_4$ onto the surface of the chromite spinel that covers the Cr_2O_3. An overall schematic of the oxide film formed on Alloy 600 in Zn free and Zn containing solutions is shown in Figure 5-2.

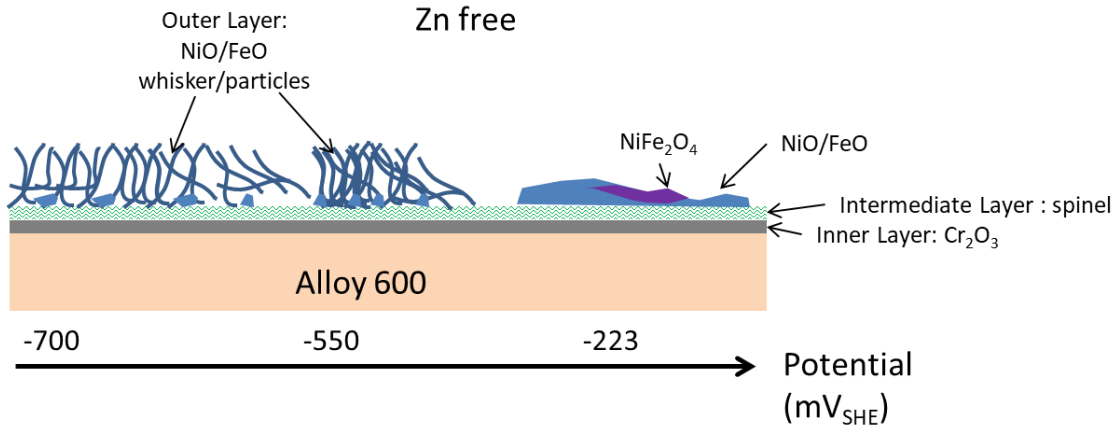

(a)

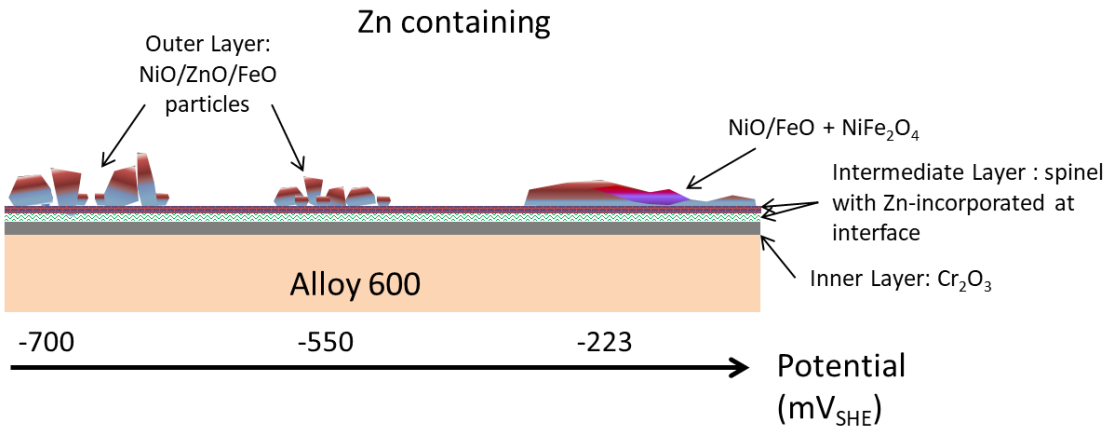

(b)

Figure 5-2: Overall morphology and composition of passive layer formed on Alloy 600 in (a) Zn free and (b) Zn containing solutions. Different colors represent difference in compositions.

5.1.2 Oxide Formation in Zn free Solution

5.1.2.1 Formation of Outer Layer

It is found from the SEM images that the outer layer of the passive film formed on Alloy 600 in Zn free solution is composed of whiskers and a few large particles at lower potentials (-700 to -550 mV $_{SHE}$) and very few needle-like oxides at high potential (-223 mV $_{SHE}$). The outer layer (both the particles and whiskers) may be deformed during the FIBing process, resulting in the irregular shape and orientation of the outer layer observed in the TEM image.

At lower potentials, the outermost particles are likely to be composed of NiO and may contain very few $NiFe_2O_4$, which agrees with the results from Terachi [17]. The whisker-shape outer layer is found to contain mainly NiO. Although a number of articles show that the outer layer consists of $NiFe_2O_4$ spinel [18], [50], it is also found through several articles that needle/filamentous oxide could be formed [16], [17], [34], [36]. Terachi [17] also indicates that needle-shape NiO could be thermodynamically stable when less than 1ppm hydrogen is added to the solution. As is discussed in [17], [36], the outer layer is formed by dissolution and precipitation of metal ions. The possible formation of the needle-like oxide compared to the planar surface of oxide is likely due to the large rate of dissolution compared to precipitation, which may be caused by the dissolved hydrogen [16]. With higher hydrogen concentration at the metal surface, i.e., at lower potential, higher rate of Ni dissolution is found on the metal surface, resulting in lower Ni content in the film and a more porous structure. It is thus suggested that the passive layer formed at -550 mV $_{SHE}$ is more protective than that formed at -700 mV $_{SHE}$, given that it has more defective outer layer and higher Ni content in the outer layer.

In an earlier investigation, Mintz and Devine [33] proposed a mechanism for the growth of the whiskers. Initially, the outer layer of NiO grows with a planar surface. As the rate of oxidation gets higher, the concentration of dissolved Ni^{2+} into the aqueous solution increases. When the $[Ni^{2+}] > [Ni^{2+}]_{eq}$, the planar NiO/water interface breaks down and cellular growth occurs, creating whiskers. The whiskers grow at their tips and their growth rate is controlled by spherical diffusion of OH^- from the bulk of the aqueous solution to the tip of the nanowire.

The higher density of whiskers observed in the sample that was polarized at -550 mV $_{SHE}$ compared to the sample that was polarized at -700 mV $_{SHE}$ is a consequence of the higher oxidation rate at -550 mV $_{SHE}$, which creates a larger amount of Ni^{2+} into the aqueous solution contacting the sample.

It is interesting that there is an absence of whiskers in the sample that is polarized at -223 mV $_{SHE}$, although NiO can still be identified in the outer layer. The absence of whiskers at -223 mV $_{SHE}$ is attributed to the lower oxidation rate at this potential where the impedance measurements, which will be discussed later in this report, indicate the charge transfer resistance of the oxidation reaction at -223 mV $_{SHE}$ is ten times greater than at -550 mV $_{SHE}$ and -700 mV $_{SHE}$. The lower rate of oxidation results in a lower concentration of Ni^{2+} in the water contacting the sample and stabilizes the planar NiO/water interface. It is also found that higher content of Cr and Fe can be identified in the outer layer, indicating that more transport, dissolution and precipitation of Cr^{3+} and Fe^{3+} takes place at -223 mV $_{SHE}$ compared to lower potentials. . Reduction of Ni in the oxide may be a result of Ni recrystallization which will be discussed later.

5.1.2.2 Formation of Inner Layer

The inner layer is found to have similar composition at the three potentials, with comparatively high concentration of Cr, containing Cr_2O_3 and small amount of Cr-rich chromite with Fe and Ni. Several articles agree that the inner layer for Ni alloy is composed of Cr-rich spinel [50] and Cr_2O_3 [20], [51], and most of them indicate that the Ni that is present in the inner layer is in the spinel form. The presence of Fe in the inner layer in this study indicates the transport process of Fe through the inner layer of Cr_2O_3, verifying the process described by Mathieu [52] and agrees with the result found by Wang [21].

Selective dissolution of metal, or oxide reduction reactions (Reactions (18)) may take place [16], [17] that is observed in several line scans at -700 mV $_{SHE}$. At low potentials where the potentials are close to the Ni/NiO equilibrium potential, the increase in hydrogen content, i.e. reduction in potential, could lead to a reduction in Ni content in the oxide, as suggested by Peng et al. [16]. The reduction reaction of nickel-rich spinel is listed below:

$$NiCr_2O_4 + H_2 \rightarrow Ni + Cr_2O_3 + H_2O \qquad (18)$$

The reduction reaction of spinel oxide could either lead to metal enrichment in the Cr_2O_3 oxide, or selective re-oxidation of metal to release into the solution/outer layer. The possible re-oxidation reactions suggested by Peng et al. [16] are,

$$Ni + 2H^+ \rightarrow Ni^{2+} + H_2 \qquad (19)$$

5.1.3 Oxide Formation in Zn containing solution

5.1.3.1 Formation of Outer Layer

It is generally reported in literature that in Ni-rich alloys, a Zn/Ni/Fe-rich spinel outer layer is formed when the alloy is immersed in Zn containing solution, and the thickness of the layer is much smaller compared to that formed in Zn free solution, which is a Ni/Fe-rich spinel outer layer [23], [25], [26]. It is found that the incorporation of Zn does not change the structure of the spinel, instead, Zn^{2+} takes the tetrahedral sites of the spinel outer layer. In the present research,

however, according to the EDS results, the outer layer particles are composed of normalized total concentration of over 80at% for Zn and Ni, indicating mostly MO type oxides rather than spinels. The formation of the MO type oxides agrees with what is found by Huang [34] and Zhang [53], and the crystalline morphology is similar to what is found by Terachi [17] under 2.75ppm DH.

The octahedral outer layer is formed through precipitation process by pickup of aqueous species, including Zn^{2+}, Fe^{2+}, Ni^{2+}, and OH^-. The morphology of outer layer formed in Zn containing solution is different from that formed in Zn free solution, although the outer layers in both solutions are identified as MO type. As is discussed in the previous sections, whisker formation in Zn free solution is a result of a high rate of cation dissolution compared to rate of precipitation, leading to a high cation concentration in the solution (high $[M^{\delta+}]$). This phenomenon is not observed in Zn containing solution. The formation of octahedron-shaped crystals is associated with high rate of precipitation, and implies a higher ratio of precipitation to dissolution rate of cation induced by Zn^{2+} addition. In other words, a low cation concentration is observed in the solution (low $[M^{\delta+}]$). A crystallized outer layer also indicates a more protective film compared to an outer layer with whiskers, as is described by Terachi et al. [17], so the outer layer formed in Zn containing solution is more protective than that in Zn free solution.

The composition of outer layer oxide formed in both Zn free and Zn containing solution at -700 mV $_{SHE}$ is shown in Figure 3-25. According to the EDS analysis, the expected formation of the outer layer could be MO at potentials below -550 mV $_{SHE}$. While NiO is formed through precipitation process, ZnO would not form either through hydrolysis reaction because Zn^{2+} does not reach the solubility limit of ZnO [54], or through ion exchange reaction with NiO in Ni^{2+} saturated solution. With the lack of evidence, one possibility of the incorporation of Zn^{2+} in the oxide could be related with Zn^{2+} adsorption on the NiO surface followed by solid diffusion process.

As is discussed earlier, the concentration gradient of Zn in the outer layer from the outer part (S/OL) to the inner part (OL/IL) represents the direction of transport of ions, and the content of ion replacement in Fe and Ni.

At -550 mV $_{SHE}$, the increase in Fe content in the outer layer indicates higher rate of precipitation or lower rate of dissolution than at lower potential. Thus, a lower overall corrosion rate at the outer layer is expected, although lower Zn concentration is also observed. Besides the possibility that Zn is less likely to replace Fe than Ni, reduction in Zn content may be due to the increase in electric field that moves against the direction of transport of Zn^{2+} ions.

Similar to what is found at -223 mV $_{SHE}$ in Zn-free solution, the planar oxide morphology of the outer layer indicates that similar film structure (MO and $M(Cr,Fe)_2O_4$) is achieved in Zn-containing solution. Substitution of Ni^{2+} with Zn^{2+} in the film is also observed in the film. Besides the reactions shown above, Zn^{2+} also substitutes Ni^{2+} in spinel. Both reactions can be verified based on the fact that zinc chomite and zinc ferrite have more negative energy of formation than nickel chromite and nickel ferrite at 300 ºC [26]. The fact that $ZnFe_2O_4$ and $ZnCr_2O_4$ have lower solubility than $NiFe_2O_4$ and $ZnCr_2O_4$ [24] also predicts that Zn would incorporate into the spinels.

$$Zn^{2+} + NiFe_2O_4 \rightarrow ZnFe_2O_4 + Ni^{2+} \qquad (20)$$

$$Zn^{2+} + NiCr_2O_4 \rightarrow ZnCr_2O_4 + Ni^{2+} \qquad (21)$$

The reduction of Ni content at -223 mV $_{SHE}$ compared to -550 mV $_{SHE}$ and -700 mV $_{SHE}$ could be associated with Ni recrystallization into metal matrix.

5.1.3.2 Formation of Inner Layer

In the current study, low content of Zn^{2+} is observed in the inner layer at all three potentials, with reduction gradient of Zn content from IL/OL interface, indicating the direction of Zn^{2+} transport in the oxide. The inner layer is found to be composed of Cr_2O_3 and MCr_2O_4. It is reported by several researchers that Zn is incorporated in the inner layer, substituting Ni^{2+} and Fe^{2+} tetrahedral sites in the spinel form [23], [25], [26]. As is discussed by Huang et al. [26], $ZnCr_2O_4$ has a more negative energy of formation than other chromites, so possible reactions for Zn incorporation in the inner layer can be

$$Zn^{2+} + NiCr_2O_4 \rightarrow ZnCr_2O_4 + Ni^{2+} \qquad (22)$$

$$Zn^{2+} + FeCr_2O_4 \rightarrow ZnCr_2O_4 + Fe^{2+} \qquad (23)$$

It is also suggested by Kawamura [23] that the incorporation of Zn in the inner layer would lead to an increase in Cr content in the oxide film, which is the controlling factor for suppressing SCC initiation. Although it is difficult to quantify it from the EDS results, it will be discussed in the following section on kinetic parameters based on EIS results.

5.2 Discussion of EIS in the Context of Results of TEM and SEM

5.2.1 Overview

A summary of equivalent circuit used for EIS analysis is shown in Figure 5-3. The circuits contains elements describing reactions taking place at the solution/outer layer interface, outer layer (OL), the interface between outer layer and inner layer (IL) and the interface between inner layer and alloy (M/IL). The details of each parameter are described in 4.3.3.1.

Potential range (mV vs SHE)	Impedance model for Zn free solution
-750 to -600	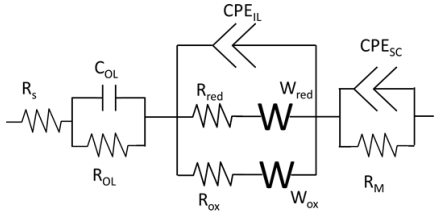
-600 to -500	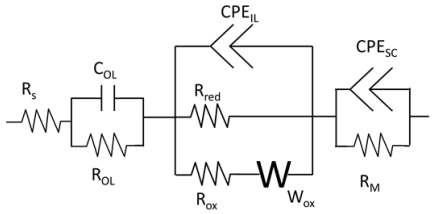
-500 to -200	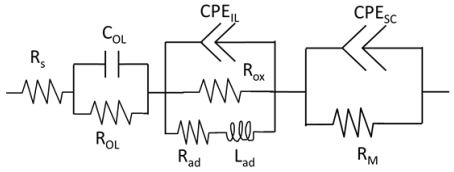

Figure 5-3: Summary of impedance equivalent circuits for Alloy 600

In the present study the combination of SEM, TEM and EDS indicate that the film formed on Alloy 600 at 320 ºC in PWR PW with no zinc addition at potentials of -700 mV $_{SHE}$ and -550 mV $_{SHE}$ consists of an inner layer of Cr_2O_3 and a layer of $(Ni_xFe_{1-x})O$ whiskers, which behave as a highly porous layer. The combination of a protective inner layer and a porous outer layer is common to many surface films formed on transition metal and transition metal alloys, in particular Fe-Cr and Ni-Cr alloys. An intermediate layer of MCr_2O_4 is confirmed from DPA and Raman experiments conducted in an earlier study. Similarly, the oxide formed at -223 mV $_{SHE}$ consists of a NiO and $NiFe_2O_4$ planar outer layer, $NiCr_2O_4$ intermediate layer and a Cr_2O_3 inner layer. The addition of Zn affects the outer layer and intermediate layer by substituting Ni^{2+} and Fe^{2+} in the oxide, and does not have a strong effect on inner layer thickness.

The spinel intermediate layer is also associated with the OL/IL part of the equivalent circuit besides the Cr_2O_3 inner layer, because this compact chromite is formed through direct oxidation and diffusion process, rather than dissolution and precipitation process. The reactions associated with oxygen injection, metal dissolution, mass transport, and hydrogen reduction all take place at this intermediate layer.

5.2.2 Comparison of fitting parameters

The results of equivalent circuit fitting for seven data sets (3 sets in Zn free solution and 4 sets in Zn containing solution) are compared in this section. Due to the limited number of experiments conducted, it is hard to perform statistical analysis on the parameters. Therefore, all the data obtained are presented to show the range of fitting values. The fitting results are scattered between different sets due to the dynamic nature of electrochemical process. However, the

general trend of potential and water chemistry effect on the fitting parameters can still be identified.

5.2.2.1 CPE_{sc}, R_M, and the Alloy/Film Interface

Figure 5-4 shows the fitting results of circuit elements associated with the alloy/film interface, i.e. resistance associated with oxidation of Ni, Cr and Fe (R_M), and capacitance (CPE_{SC}, Yo_{SC}, α_{SC}) associated with the double layer for this reaction. The relationship between each parameter is described in Eq. (17). The values in both Zn free and Zn containing solutions show similar change over the potential range from -743mV $_{SHE}$ to -223mV $_{SHE}$. No effect of zinc is observed because EDS results show that there is no zinc in the inner layer of Cr_2O_3 and, in particular, there is no zinc at the interface between Cr_2O_3 and the alloy, which is the site of the metal oxidation.

The exponential term of α_{SC} for double layer capacitance shown in Figure 5-5 (b) is associated with dispersion of time constants, i.e., dispersion of current along surface. The value of α_{SC} decreases with potential at below -500 mV $_{SHE}$ and increase with potential at above -500 mV $_{SHE}$. A number of reasons could account for the appearance of CPE, including (1) distribution of time constants, which are associated with the movement (displacement and rotation) of charges in response to the applied, cyclic electric field of the EIS measurement, (2) surface roughness, and (3) a non-uniform distribution of current or potential. TEM results show that the Cr_2O_3/alloy interface is very uneven, indicating non-uniform oxidation of the alloy. Hence, one possible cause of the CPE behavior of the double layer is non-uniform current flow. The exponential term α would increase when the interface is more uniform. As a result, the reduction of α_{SC} at potentials below -500mV $_{SHE}$ is due to the non-evenness of Cr_2O_3/alloy interface, which indicates an increasing non-uniformity of current. The increase of α_{SC} at potentials above -500mV $_{SHE}$ shows that a more uniform alloy/film interface is obtained.

The pre-exponent term of the double layer Yo_{SC} (presented in Figure 5-5 (a) show a slight increase below -650 mV $_{SHE}$, followed by a sharp reduction at potential below -400 mV $_{SHE}$ and a comparative constant value above -400 mV $_{SHE}$. The values of Yo_{SC} (10^{-4} ~10^{-2} $S.s^{\alpha}/cm^2$) and α_{SC} (0.5~1) agree with the range of low frequency and electric double layer capacitance reported by [26], [32], [55]. Since it is generally believed that the inner layer grows at the metal/film interface where oxygen vacancy is generated [37], [56], this capacitance reveals information related to the electronic properties of the inner layer. Since there is a large variation in the exponential term α_{SC}, an effective capacitance needs to be calculated in order to review the relationship. The effective capacitance can be calculated using the equation developed by Harrington and Devine [57],

$$C_{SC\_eff} = Y_o^{\frac{1}{\alpha}}(R_s^{-1} + R_M^{-1})^{\frac{\alpha-1}{\alpha}} \qquad (24)$$

The resulting $C_{SC\_eff}^{-2}$ versus potential is plotted in Figure 5-5 (c). The large dependence of this capacitance on potential suggests that the inner layer is a n-type semiconductor between potentials below -500 mV $_{SHE}$, and is an p-type semiconductor above -500 mV $_{SHE}$ as agrees with the findings suggested by Bojinov [48]. TEM results show that Cr_2O_3 is present at potentials from -743 mV $_{SHE}$ to -223mV $_{SHE}$, and Cr_2O_3 is a p-type semiconductor. One possible reason for the n-type semiconductor at potentials below -500mV $_{SHE}$ could be associated with the formation of CrOOH.

The resistance R_M associated with metal oxidation (related with k_3 and k_4) is relatively consistent below -500 mV $_{SHE}$ despite the variation of values. This indicates that the overall rate constant of metal oxidation does not change over potential in this range. The jump in R_M at -500 mV $_{SHE}$ for both solution conditions is likely associated with the formation of Fe^{3+} that increases the rate of oxidation.

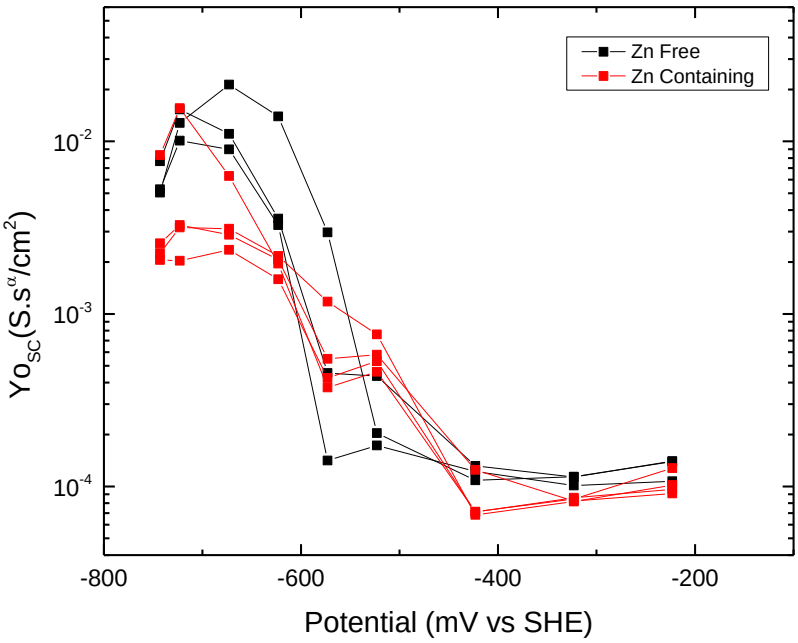

(a)

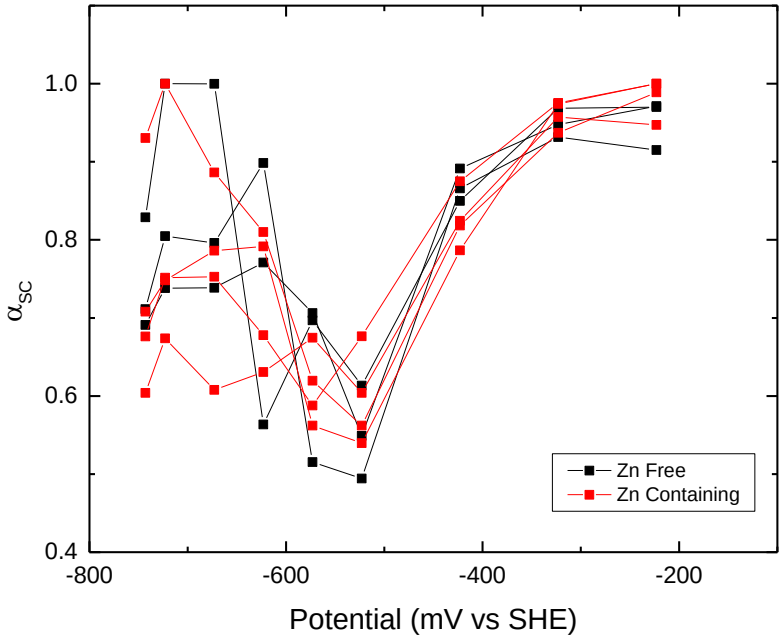
1.0
0.8
0.6
0.4
α_{SC}
-800
-600
-400
-200
Potential (mV vs SHE)
Zn Free
Zn Containing

(b)

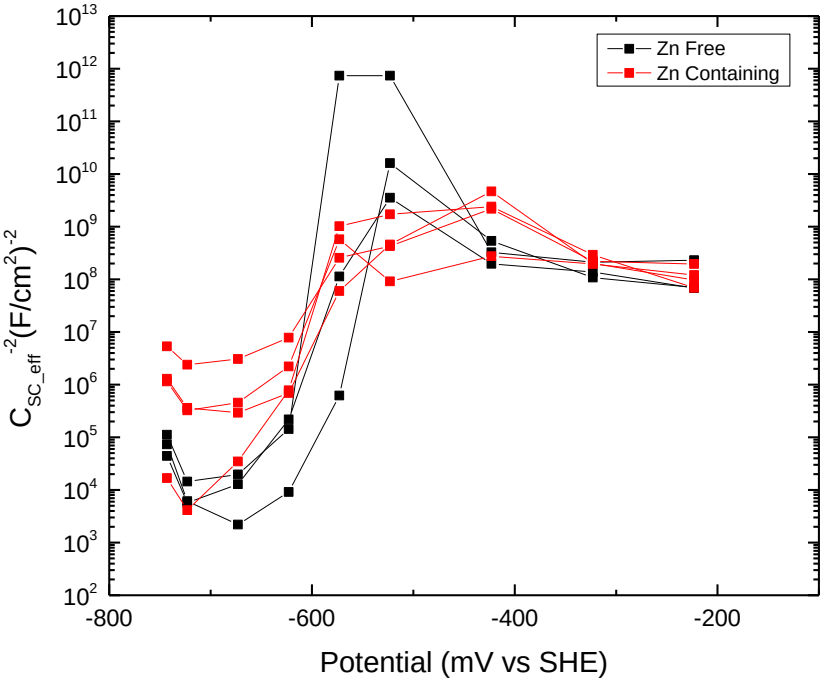
10^{13}
10^{12}
10^{11}
10^{10}
10^{9}
10^{8}
10^{7}
10^{6}
10^{5}
10^{4}
10^{3}
10^{2}
$C_{SC\_eff}^{-2}(F/cm^2)^{-2}$
-800
-600
-400
-200
Potential (mV vs SHE)
Zn Free
Zn Containing

(c)

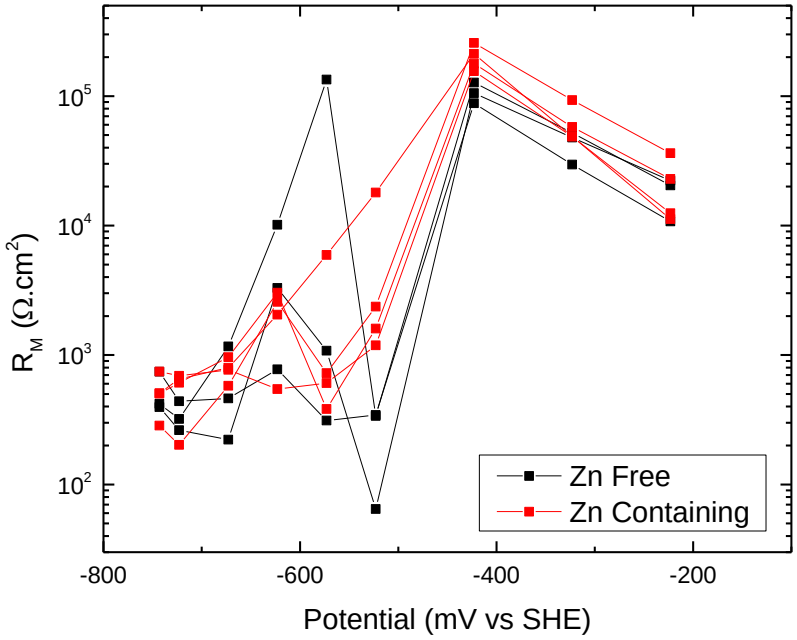

(c)

Figure 5-4: Fitting results of seven different tests (three tests in Zn free solution and four tests in Zn containing solution) for (a) Yo_{SC}, (b) α_{SC}, (c) $C_{SC\_eff}^{-2}$ and (d) R_M representing the alloy/Cr_2O_3 interface. Each line shows one sample oxidized at different potentials from -743mV $_{SHE}$ to -223mV $_{SHE}$.

5.2.2.2 R_{ox}, Z_{W_ox}, CPE_{IL} and the Inner Layer of Cr_2O_3 and MCr_2O_4

The fitting results of parameters associated with the inner layer/intermediate layer formation are shown in Figure 5-5. The relationship of these parameters with the total impedance is presented in Eq. (13). The parameters associated with the hydrogen reduction reaction will be discussed in the next section. The growth of Cr_2O_3 and chromite is associated with injection of oxygen into the oxide film, transport of metal and oxygen through Cr_2O_3, and the geometric capacitance of the inner layer. A Zn effect is observed for changes in R_{ox} at potentials below -500 mV $_{SHE}$, whereas other parameters are not affected by the addition of Zn into the solution.

Yo_{IL} and α_{IL} are associated with the capacitance of Cr_2O_3/MCr_2O_4, and the double layer at the IL/OL interface, and it is hard to distinguish between these using the current equivalent circuit. It is found that he exponential term α_{IL} remains between 0.7 and 1 at potentials below -500 mV $_{SHE}$, and significantly reduces to values around 0.5 at potential above -500 mV $_{SHE}$. The change in Yo_{IL} would be associated with the change in thickness across the inner layer as well as the capacitance of double layer at IL/OL. The value of Yo_{IL} ranges between 10 and 100 $\mu S.s^{\alpha}/cm^2$ at potentials below -500mV $_{SHE}$, and it agrees with the range of double layer capacitance calculated by Bojinov et al. [46]. A maximum value of Yo_{IL} is observed at -423mV $_{SHE}$, above which the value lies between 100 and 1000 $\mu S.s^{\alpha}/cm^2$. Both Yo_{IL} and α_{IL} undergo a change at -423mV $_{SHE}$, and it is likely to relate to the process of Fe^{2+} oxidation to Fe^{3+} at the IL/OL interface.

As is described in 4.3.3.1, R_{ox} is associated with oxygen injection and metal dissolution (k_1 and k_2) at IL/OL interface (Reaction (9), (10)). At this interface, an oxygen anion is incorporated in the inner layer from water, annihilating an oxygen vacancy; a metal cation dissolves into solution, creating a metal vacancy. No significant potential dependence is observed at potentials below -550 mV $_{SHE}$, and the value of R_{ox} does not change significantly over this potential range. This observation indicates that there is no significant change in rate constants for k_1 and k_2 with increasing potential below -550 mV $_{SHE}$. At higher potentials, the sudden increase of R_{ox} at around -500 mV $_{SHE}$ suggests that further charge transfer reaction would take place at this potential, likely associated with the oxidation of Fe^{2+} to Fe^{3+} predicted by thermodynamic calculation and confirmed by TEM results.

Note that at low potentials (i.e., potentials ≤ -573 mV $_{SHE}$) R_{ox} is nearly 100 times higher for tests conducted in zinc containing water (0.1 ppm Zn) than for tests conducted in zinc-free water. The strong effect of zinc occurs despite the fact that EDS indicates there is no zinc in the inner layer of Cr_2O_3. The fact that σ_{ox} is not affected by the presence of Zn indicate that transport of oxygen through the inner layer is not influenced by Zn addition in the solution, i.e., the combination of concentration and diffusivity of metal and oxygen in Cr_2O_3. Consequently, the effect of zinc in dramatically decreasing the rate of metal oxidation must be the result of a zinc effect on the formation of O^{2-} at the outer surface of Cr_2O_3.

With immersion in aqueous solution, oxygen anion O^{2-} is created on the surface of an oxide such as Cr_2O_3 by the dissociation of water into hydronium ions and hydroxide ions: $2H_2O \rightarrow H_3O^+ + OH^-$ The hydronium ions are adsorbed on the oxygen ions in the surface of the oxide and hydroxide ions are adsorbed on the metal cations (i.e., Cr^{3+}) in the surface of the oxide. In a mildly alkaline solution such as PWR primary water (PW), the higher concentration of OH^- in the water results in OH^- combining with H^+ that is adsorbed on O^{2-} in the oxide surface so that H_2O is adsorbed on the O^{2-} in place of adsorbed H^+. Zinc ions in the water are hydrated and might attach to the adsorbed OH^-. The attachment of aqueous zinc cations to the adsorbed hydroxide, which is the source of O^{2-} that diffuses to the alloy/Cr_2O_3 interface and grows the Cr_2O_3 into the alloy, might decrease the rate of formation of O^{2-} at the outer surface of Cr_2O_3 and thereby explain how zinc ions in the water decrease the metal oxidation rate.

In addition, hydrated zinc ions might react with hydroxide that is adsorbed on the outer surface of Cr_2O_3:

$$Zn \cdot nH_2O^{2+} + OH^-_{ads} \rightarrow OZn_{ads} + nH_2O + H^+ \quad (25)$$

The bonding of Zn^{2+} to the O^{2-} might prevent the migration of O^{2-} from the outer surface of Cr_2O_3 to the Cr_2O_3/alloy interface and thereby provide a second method by which aqueous zinc ions decrease the oxidation rate of Alloy 600 (i.e., increase R_{ox}).

Cr_2O_3 is generally a protective film that inhibits further oxidation of the alloy. At potentials less than -573 mV $_{SHE}$ R_{ox} in the zinc-free solution is significantly smaller (by almost two orders of magnitude) than R_{ox} in the zinc-containing solution. That is, the passive film formed in the zinc-free solution is less protective than the passive film formed in the zinc-containing solution. The difference in R_{ox} helps to explain the large quantity of NiO (in the form of whiskers) that is formed in the zinc-free solution and the smaller amount of NiO (in the form of a planar, porous

layer) that is formed in the zinc-containing solution. The influence of the NiO whiskers and the planar, porous NiO on the impedance spectra is discussed below after first considering the spinel layer and its effect on impedance.

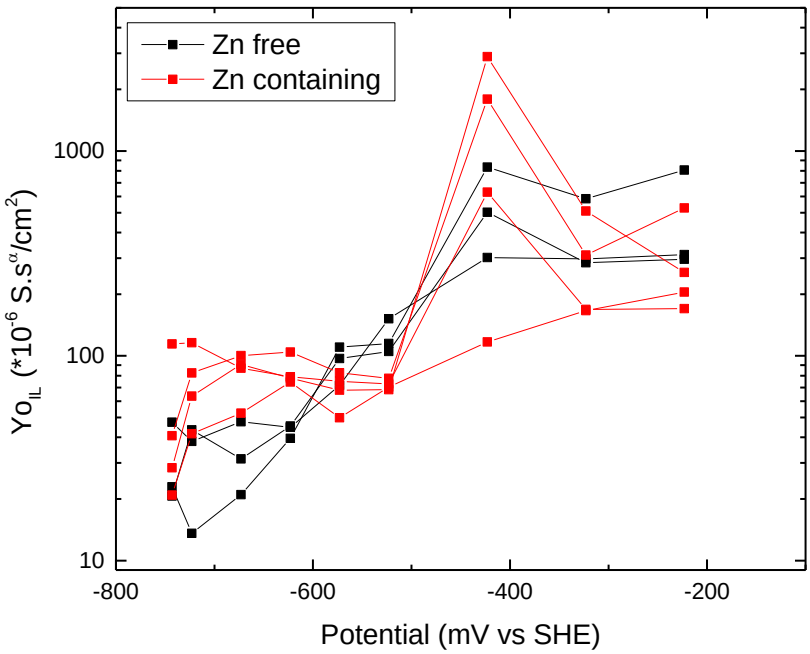

(a)

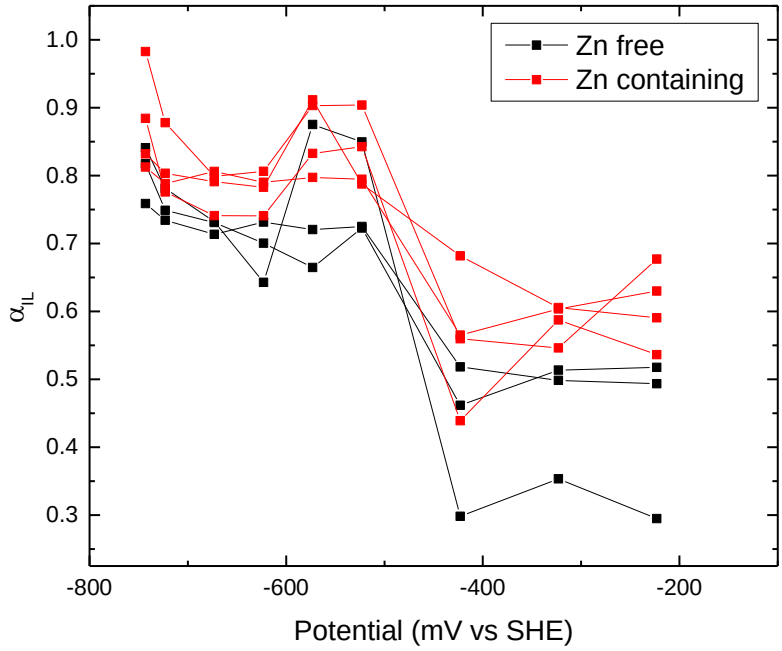
Zn free
Zn containing
α_{IL}
1.0
0.9
0.8
0.7
0.6
0.5
0.4
0.3
-800
-600
-400
-200
Potential (mV vs SHE)

(b)

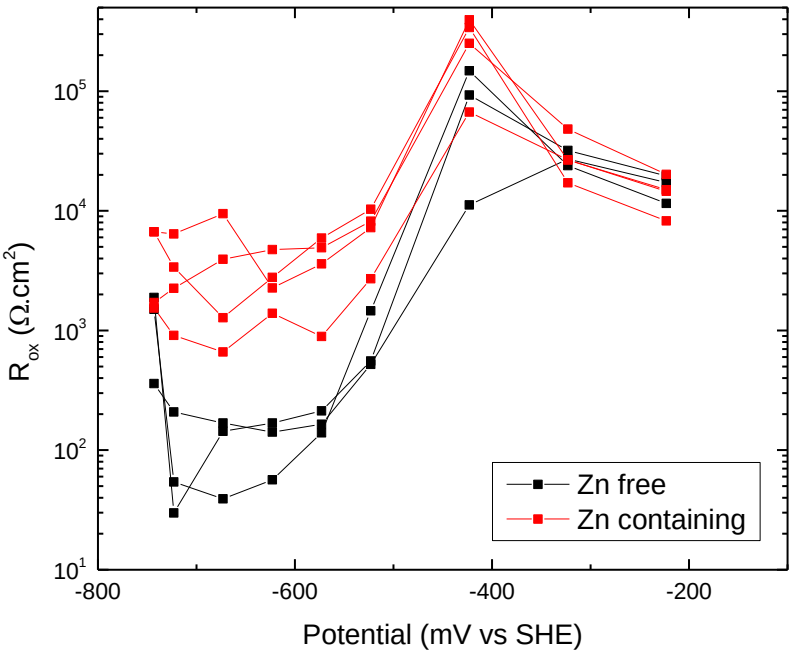
Zn free
Zn containing
R_{ox} (Ω.cm^2)
10^5
10^4
10^3
10^2
10^1
-800
-600
-400
-200
Potential (mV vs SHE)

(c)

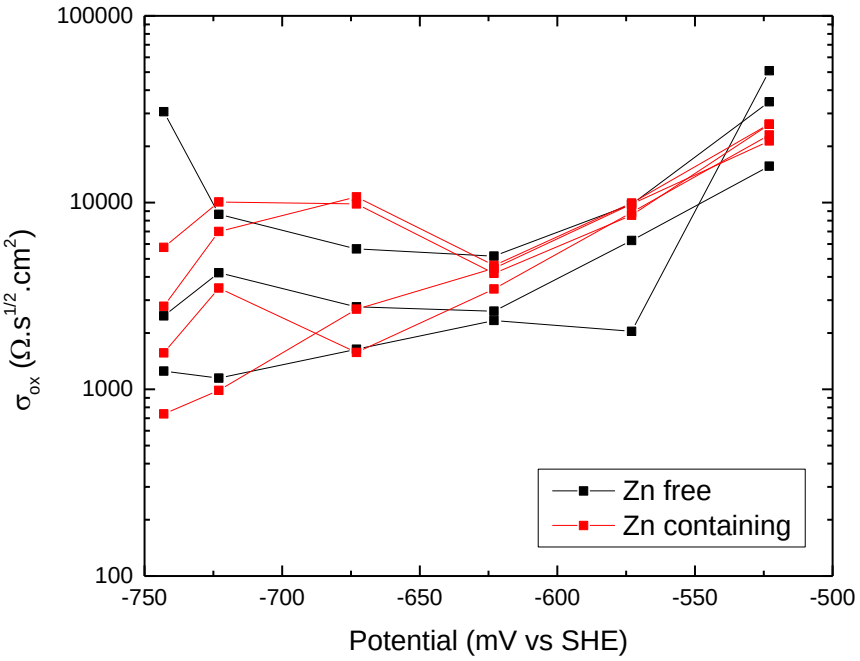

(d)

Figure 5-5: Fitting results of seven different tests (three tests in Zn free solution and four tests in Zn containing solution) for (a) Yo_{IL}, (b) α_{IL}, (c) R_{ox} and (d) σ_{ox} representing the Cr_2O_3, MCr_2O_4 and IL/OL interface. Each line shows one sample oxidized at different potentials from -743mV $_{SHE}$ to -223mV $_{SHE}$.

5.2.2.3 R_{red}, Z_{Wred} and Reduction of Hydrogen

The hydrogen reduction reaction is observed at potentials below -500 mV $_{SHE}$. The fitting results associated with hydrogen reduction reaction is shown in Figure 5-6, and it is suggested by the plots that Zn does not have an effect on hydrogen reduction reaction as well as hydrogen transport inside Cr_2O_3/chromite. Given that the reaction is not associated with Zn, and that no Zn is present in the inner layer, Zn does not influence the hydrogen reduction reaction on Alloy 600.

The existence of hydrogen reduction reaction is confirmed by the static polarization current that lies close to 0A.The exponential increase of R_{red} agrees with the prediction according to the Butler-Volmer equation, as the rate of reduction reaction decreases exponentially with potential. As a result, the transport process associated with hydrogen in the inner layer gets more difficult with potential.

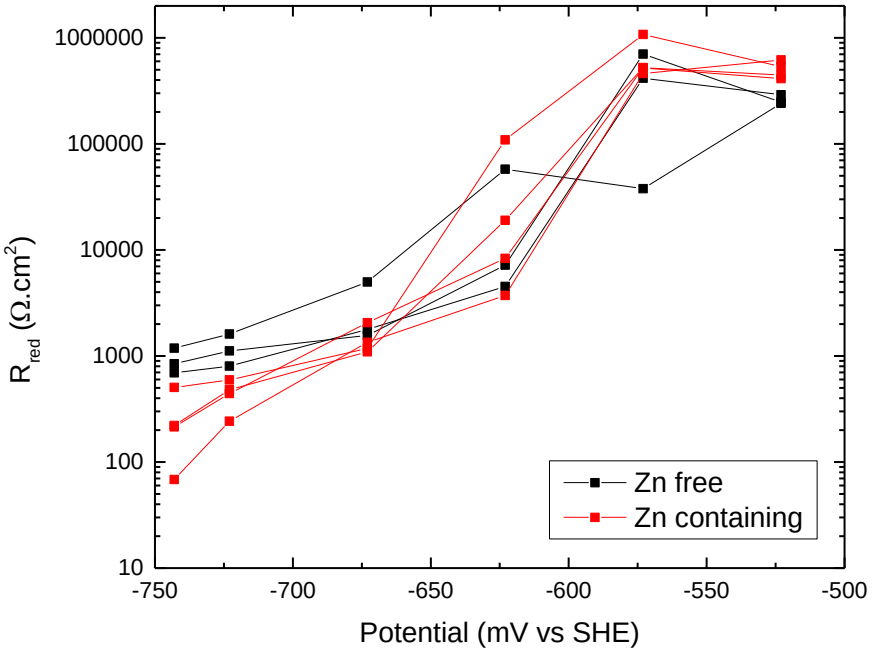
1000000
100000
10000
1000
100
10
R_{red} (Ω.cm^2)
-750
-700
-650
-600
-550
-500
Potential (mV vs SHE)
Zn free
Zn containing

(a)

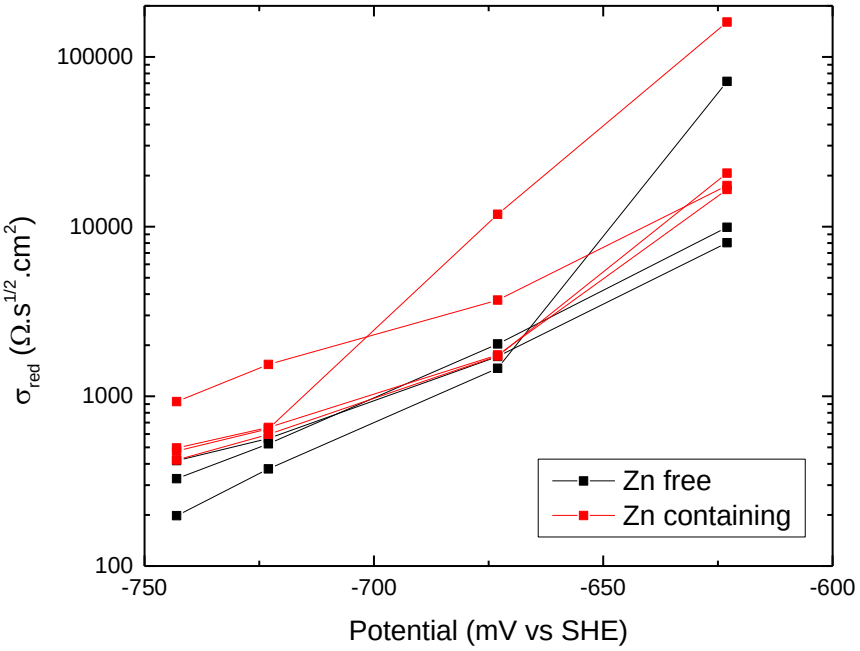

(b)

Figure 5-6: Fitting results of seven different tests (three tests in Zn free solution and four tests in Zn containing solution) for (a) R_{red} and (b) σ_{red} representing the hydrogen reduction reaction at IL/OL interface. Each line shows one sample oxidized at different potentials from -743mV $_{SHE}$ to -223mV $_{SHE}$.

5.2.2.4 R_{OL}, C_{OL}, and Porous NiO

It is interesting to note from the Nyquist plots that the imaginary component of EIS, -Im(Z), of Alloy 600 at -700 mV $_{SHE}$ and at -550 mV $_{SHE}$ at low frequencies is much greater than that of Alloy 600 at -223 mV $_{SHE}$. One possible explanation is that the whiskers that cover the surface at -700 mV $_{SHE}$ and -550 mV $_{SHE}$ increase Im(Z) at low frequency. That is, the absence of whiskers at -223 mV $_{SHE}$ results in a significantly lower Im(Z) at low-frequency at this potential. According to this hypothesis the collection of whiskers acts as a porous surface film and increases impedance by inhibiting transport. Unfortunately the hypothesized influence of the nanowires on EIS at low frequency is not supported by the EIS of Alloy 600 in zinc-containing PWR PW. In particular, the low frequency Im(Z) at -700 mV $_{SHE}$ and -550 mV $_{SHE}$ of Alloy 600 in zinc-free PWR PW, in which whiskers cover the surface, are nearly identical to the low frequency Im(Z) of Alloy 600 in zinc-containing water, in which the surface is completely free of whiskers. The results indicate that whiskers have no effect on the low frequency Im(Z).

The fact that the NiO whiskers have no effect on low frequency impedance is consistent with the proposed chemical mechanism of whisker formation. That is, NiO whiskers form as a consequence of the breakdown of the planar NiO/aqueous solution interface [33]. The breakdown is driven by the concentration of Ni^{2+} exceeding the equilibrium concentration of Ni^{2+}. The formation of NiO nanowires has no effect on low frequency impedance because the whiskers form by a chemical (i.e., non-electrochemical) mechanism. Of course, the charge

transfer oxidation reaction, which generates metal cations including Ni^{2+}, is an electrochemical reaction and its impedance contributes to the overall impedance of Alloy 600 immersed in PWR PW and anodically polarized at -700 mV $_{SHE}$, -550 mV $_{SHE}$, and -223 mV $_{SHE}$. However, the results show that the formation and growth of the NiO whiskers do not contribute to the electrode's impedance. As already mentioned, that the formation and growth of whiskers does not contribute to the impedance of Alloy 600 is understandable in that the reactions are non-electrochemical.

The whiskers do increase the high frequency impedance as a consequence of the pore resistance. For this reason, as clearly seen in the Bode plots (Figure 4-4 (a)), the high frequency impedance of Alloy 600 in zinc-free PWR PW increases with increasing potential (i.e., with increasing amount of NiO nanowires). In contrast, the high frequency impedance of Alloy 600 in zinc-containing PWR PW (Figure 4-5 (a)) is independent of potential because nanowires are not formed.

In Zn free solution, R_{OL} and C_{OL} shown in Figure 5-3 are components of the impedance of the water that fills the space between NiO nanowires that form the outer layer. Accordingly, $R_{OL}\cdot C_{OL}$ of the surface film formed at -223 mV $_{SHE}$ must be very different from $R_{OL}\cdot C_{OL}$ of the surface films formed at -700 mV $_{SHE}$ and -550 mV $_{SHE}$, which is attributed to the fact that the presence of whiskers is almost eliminated at -223 mV $_{SHE}$.

The SEM and TEM results performed at samples oxidized at -700 mV $_{SHE}$ and -550 mV $_{SHE}$ indicate an effectively porous outer layer composed of NiO whiskers covers the surface of Alloy 600. In contrast, SEM and TEM images indicate there are no NiO whiskers on the surface of Alloy 600 polarized at -223 mV $_{SHE}$. Instead, at -223 mV $_{SHE}$, the TEM results show that the outer layer consists of a relatively compact 20-40nm thick layer of NiO with inconsistent thickness along surface. Presumably, the absence of whisker is associated with a low concentration of Ni^{2+} that stabilizes the planar NiO/water interface, so a planar but porous layer of NiO is formed rather than NiO whiskers.

In Zn containing solution, a planar, porous layer of NiO/ZnO is formed at potentials from -743 mV $_{SHE}$ to -223 mV $_{SHE}$ rather than NiO whiskers according to the SEM result, and a low $[Ni^{2+}]$ is present at these three potentials in the solution. The parameters of R_{OL} and C_{OL} presented in Figure 5-3 are also associated with the water that fills in the space between two particles.

If the proposed characterization of the outer layer at -700 mV $_{SHE}$ and -550 mV $_{SHE}$ and the outer layer at -223 mV $_{SHE}$ is correct then the product of $R_{OL}\cdot C_{OL}$ should exhibit approximately the same value at -700 mV $_{SHE}$, -550 mV $_{SHE}$ and -223 mV $_{SHE}$ for EIS conducted in both zinc-containing and zinc-free PWR PW. R_{OL} and C_{OL} can be calculated with:

$$R_{OL} = \frac{\rho l}{A} \qquad (26)$$

$$C_{OL} = \frac{\varepsilon \varepsilon_o A}{l} \qquad (27)$$

where A is the area between whiskers/ particles that is filled with water, l is the length of the outer layer whiskers or the thickness of particles, ρ is the resistivity of the solution, ε is the dielectric constant of the solution and ε_o is the dielectric constant of vacuum.

Therefore,

$$R_{OL} \cdot C_{OL} = \rho \varepsilon \varepsilon_o \qquad (28)$$

The result of $R_{OL} \cdot C_{OL}$ is shown in Figure 5-7. The results indicate that the value of the product $R_{OL} \cdot C_{OL}$ is the same for most water chemistry- potential combination. The only instance in which the product is not between 30-100 nsec is found at potentials above -423mV $_{SHE}$ in zinc-free water.

The result for the constant product of $R_{OL}.C_{OL}$ is justified with the fact that the parameters associated with the solution, i.e. ρ and ε does not change with potential or the change with solution chemistry. It is found in previous studies that the maximum solubility of Zn in ZnO at 300 ºC at pH=7.3 is 200ppb [54], and the maximum solubility of NiO is 0.9ppb Ni [58] at the same condition, and the solubility of these species are not affected by potential. Compared to the bulk solution containing 1200ppm B and 2ppm Li, the effect of Zn^{2+} and Ni^{2+} on solution resistivity and dielectric constant is minimal. As a result, $R_{OL}.C_{OL}$ is a constant regardless of the two solution chemistry conditions.

The products of $R_{OL}.C_{OL}$ at potentials above -423mV $_{SHE}$ in Zn free solution are different from the rest of the potential-water chemistry conditions. It is likely due to that there is a different process than oxide formation happening that the $R_{OL}C_{OL}$ circuit element does not describe. Possible processes may be associated with charge transfer associated with whisker dissolution.

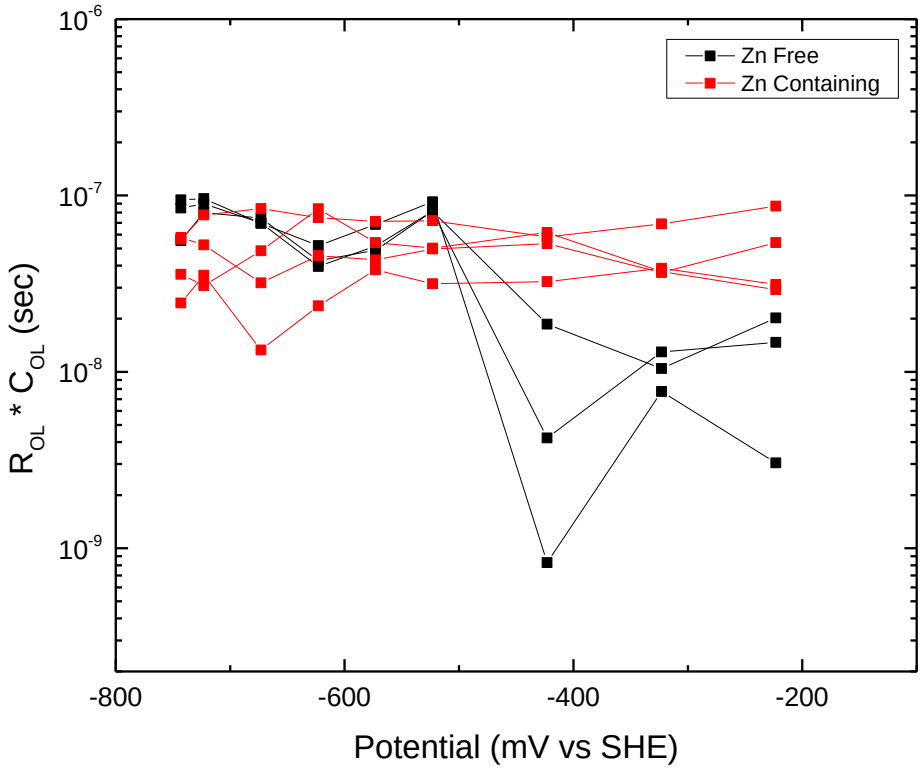

Figure 5-7: Fitting results of seven different tests (three tests in Zn free solution and four tests in Zn containing solution) for $R_{OL}C_{OL}$ representing the porous outer layer of whiskers and particles. Each line shows one sample oxidized at different potentials from -743mV $_{SHE}$ to -223mV $_{SHE}$.

Chapter 6. Conclusions

In order to investigate the effect of Zn addition in primary water on the passivity of Alloy 600, both *in-situ* EIS and *ex-situ* TEM-EDS are conducted. The two questions that are addressed in the study are (1) how does Zn change the oxidation process, and (2) how does Zn change the oxide chemistry.

After combining the results of EIS and TEM-EDS, it is found that

1. The passive layer of Alloy 600 formed in both Zn containing and Zn free PWR PW consists of a MO porous outer layer, chromite intermediate layer, and Cr_2O_3 inner layer in a potential range between -700 mV $_{SHE}$ and -223 mV $_{SHE}$. The existence of each layer is justified by DPA and previous Raman analysis on Alloy 600.

2. At all potentials tested, Zn^{2+} only substitutes for Ni^{2+} and Fe^{2+} in the outer layer and intermediate layer, and no Zn is observed in the inner layer. The variance in Zn concentration in the outer layer and intermediate layer indicates the diffusion direction of Zn.

3. The most significant effect of Zn on oxide formation according to TEM is the change in morphology in outer layer from whiskers to more uniform crystalline oxides. It is also found that Zn incorporation promotes the precipitation of Ni and Fe, as well as the dissolution of Fe into the solution.

4. The EIS overall spectrum does not show a difference with Zn addition, however, after fitting the spectrum into equivalent circuits constructed based on possible reactions taking place based on TEM morphology, it is shown that the addition of Zn in the solution significantly changes the resistance of oxidation injection (100 times larger for Zn containing solution) at the IL/OL interface at potentials below -573 mV $_{SHE}$. The change in the value is likely a result of hydrated Zn adsorption to the film surface, preventing the incorporation of oxygen into the inner layer.

5. The fact that all other parameters of the EIS model do not change is consistent with the TEM results, regarding the composition and thickness of the inner layer. The EIS fitting also suggested that the inner layer is an n-type semiconductor at potentials below-500 mV $_{SHE}$, a p-type semiconductor at potentials above -500 mV $_{SHE}$. A continuous p-type Cr_2O_3 inner layer is confirmed at all test potentials by TEM, so the results suggests that an n-type CrOOH could be present at -500 mV $_{SHE}$, as is also predicted by DPA analysis.

References

[1] R. B. Rebak and Z. Szklarska-Smialowska, “The mechanism of stress corrosion cracking of alloy 600 in high temperature water,” *Corros. Sci.*, vol. 38, no. 6, pp. 971–988, Jun. 1996.

[2] IAEA, “Stress Corrosion Cracking in Light Water Reactors: Good Practices and Lessons Learned,” 2011.

[3] G. Wu, “A Probabilistic-Mechanistic Approach to Modeling Stress Corrosion Cracking Propagation in Alloy 600 Components with Applications,” Thesis, 2011.

[4] R. H. Jones, Ed., *Stress-Corrosion Cracking: Materials Performance and Evaluation, Second Edition*. Metals Park, OH: ASM International, 2017.

[5] “Steam Generator Reference Book, Revision 1,” Electric Power Research Institute (EPRI), Palo Alto, CA, RP2858; RP4004, Dec. 1994.

[6] P. K. Mathur and S. V. Narasimhan, “Good Water Chemistry practices for PHWRs,” *Cool. Technol. Water-Cool. React.*, vol. 1, pp. 90–93, 1992.

[7] *ASM Handbook Volume 2: Properties and Selection: Nonferrous Alloys and Special-Purpose Materials*, vol. 2. ASM International, 1990.

[8] F. Leonard, “Study of Stress Corrosion Cracking of Alloy 600 in High Temperature High Pressure water,” University of Manchester, 2010.

[9] S. S. Hwang, Y. S. Lim, S. W. Kim, D. J. Kim, and H. P. Kim, “ROLE OF GRAIN BOUNDARY CARBIDES IN CRACKING BEHAVIOR OF Ni BASE ALLOYS,” *Nucl. Eng. Technol.*, vol. 45, no. 1, pp. 73–80, Feb. 2013.

[10] G. S. Was and K. Lian, “Role of Carbides in Stress Corrosion Cracking Resistance of Alloy 600 and Controlled-Purity Ni-16% Cr-9% Fe in Primary Water at 360°C,” *CORROSION*, vol. 54, no. 9, pp. 675–688, Sep. 1998.

[11] A. Aguilar, J. L. Albarran, H. F. Lopez, and L. Martinez, “Microstructural response on the cracking resistance of alloy 600,” *Mater. Lett.*, vol. 61, no. 1, pp. 274–277, Jan. 2007.

[12] R. W. Staehle and J. A. Gorman, “Quantitative Assessment of Submodes of Stress Corrosion Cracking on the Secondary Side of Steam Generator Tubing in Pressurized Water Reactors: Part 2,” *CORROSION*, vol. 60, no. 1, pp. 5–63, Jan. 2004.

[13] P. M. Scott, “An overview of materials degradation by stress corrosion in PWRs,” presented at the EUROCORR 2004: long term prediction and modeling of corrosion, France, 2004.

[14] J. Flis, “Role of oxide films in stress corrosion cracking of mild steel in nitrate solutions,” *Corros. Sci.*, vol. 15, no. 6, pp. 553–564, Jan. 1975.

[15] C. S. Kumai, “An in-situ SERS investigation of the passive film on stainless steel at high temperature in pressurized water,” Ph.D., University of California, Berkeley, United States -- California, 2000.

[16] Q. Peng, J. Hou, K. Sakaguchi, Y. Takeda, and T. Shoji, “Effect of dissolved hydrogen on corrosion of Inconel Alloy 600 in high temperature hydrogenated water,” *Electrochimica Acta*, vol. 56, no. 24, pp. 8375–8386, Oct. 2011.

[17] T. TERACHI *et al.*, “Influence of Dissolved Hydrogen on Structure of Oxide Film on Alloy 600 Formed in Primary Water of Pressurized Water Reactors,” *J. Nucl. Sci. Technol.*, vol. 40, no. 7, pp. 509–516, Jul. 2003.

[18] J. Panter, B. Viguier, J.-M. Cloué, M. Foucault, P. Combrade, and E. Andrieu, “Influence of oxide films on primary water stress corrosion cracking initiation of alloy 600,” *J. Nucl. Mater.*, vol. 348, no. 1, pp. 213–221, Jan. 2006.
[19] H. Lefaix-Jeuland, L. Marchetti, S. Perrin, M. Pijolat, M. Sennour, and R. Molins, “Oxidation kinetics and mechanisms of Ni-base alloys in pressurised water reactor primary conditions: Influence of subsurface defects,” *Corros. Sci.*, vol. 53, no. 12, pp. 3914–3922, Dec. 2011.
[20] A. Machet *et al.*, “XPS and STM study of the growth and structure of passive films in high temperature water on a nickel-base alloy,” *Electrochimica Acta*, vol. 49, no. 22, pp. 3957–3964, Sep. 2004.
[21] F. Wang, “In-situ Surface Enhanced Raman Spectroscopy Investigation of the Surface Films on Alloy 600 and Alloy 690 in Pressurized Water Reactor-Primary Water,” Ph.D., University of California, Berkeley, United States -- California, 2012.
[22] I. Betova, M. Bojinov, P. Kinnunen, and T. Saario, “Zn injection in Pressurized Water Reactors - laboratory tests, field experience and modelling,” VTT, Espoo, VTT-R-05511-11, 2011.
[23] H. Kawamura *et al.*, “The Effect of Zinc Addition to Simulated PWR Primary Water on the PWSCC Resistance, Crack Growth Rate and Surface Oxide Films Characteristics of Prefilmed Alloy 600,” presented at the CORROSION 98, 1998.
[24] K. Miyajima and H. Hideo Hirano, “Thermodynamic Consideration on the Effect of Zinc Injection into PWR Primary Coolant for the Reduction of Radiation Build Up and Corrosion Control,” presented at the CORROSION 2001, 2001.
[25] S. E. Ziemniak and M. Hanson, “Zinc treatment effects on corrosion behavior of Alloy 600 in high temperature, hydrogenated water,” *Corros. Sci.*, vol. 48, no. 10, pp. 3330–3348, Oct. 2006.
[26] J. Huang, X. Liu, E.-H. Han, and X. Wu, “Influence of Zn on oxide films on Alloy 690 in borated and lithiated high temperature water,” *Corros. Sci.*, vol. 53, no. 10, pp. 3254–3261, Oct. 2011.
[27] X. Liu, X. Wu, and E.-H. Han, “Influence of Zn injection on characteristics of oxide film on 304 stainless steel in borated and lithiated high temperature water,” *Corros. Sci.*, vol. 53, no. 10, pp. 3337–3345, Oct. 2011.
[28] X. Liu, X. Wu, and E.-H. Han, “Effect of Zn injection on established surface oxide films on 316L stainless steel in borated and lithiated high temperature water,” *Corros. Sci.*, vol. 65, no. Supplement C, pp. 136–144, Dec. 2012.
[29] T. S. Mintz and T. M. Devine, “Influence of Surface Films on the Susceptibility of Inconel 600 to Stress Corrosion Cracking,” *Key Eng. Mater.*, vol. 261–263, pp. 875–884, 2004.
[30] H. Kim and D. D. Macdonald, “Measurement of steady-state hydrogen electrode reactions on Alloys 600 and 690 tubes,” *Corros. Sci.*, vol. 52, no. 4, pp. 1139–1145, Apr. 2010.
[31] X. Li, J. Wang, E.-H. Han, and W. Ke, “Corrosion behavior for Alloy 690 and Alloy 800 tubes in simulated primary water,” *Corros. Sci.*, vol. 67, no. Supplement C, pp. 169–178, Feb. 2013.
[32] Y. Qiu, T. Shoji, and Z. Lu, “Effect of dissolved hydrogen on the electrochemical behaviour of Alloy 600 in simulated PWR primary water at 290°C,” *Corros. Sci.*, vol. 53, no. 5, pp. 1983–1989, May 2011.

[33] T. S. Mintz *et al.*, “Electrochemical Synthesis of Functionalized Nickel Oxide Nanowires,” *Electrochem. Solid State Lett.*, vol. 8, no. 9, pp. D26–D30, Jan. 2005.
[34] F. Huang, J. Wang, E.-H. Han, and W. Ke, “Microstructural characteristics of the oxide films formed on Alloy 690 TT in pure and primary water at 325°C,” *Corros. Sci.*, vol. 76, no. Supplement C, pp. 52–59, Nov. 2013.
[35] L. Kaufman, “Pourbaix Diagrams in High Temperature Water for Ni-Cr-Fe Alloys,” EPRI, Palo Alto, 2008.
[36] Z. Zhang, J. Wang, E.-H. Han, and W. Ke, “Influence of dissolved oxygen on oxide films of Alloy 690TT with different surface status in simulated primary water,” *Corros. Sci.*, vol. 53, no. 11, pp. 3623–3635, Nov. 2011.
[37] D. D. Macdonald, “The history of the Point Defect Model for the passive state: A brief review of film growth aspects,” *Electrochimica Acta*, vol. 56, no. 4, pp. 1761–1772, Jan. 2011.
[38] J. Macák, P. Sajdl, P. Kučera, R. Novotný, and J. Vošta, “In situ electrochemical impedance and noise measurements of corroding stainless steel in high temperature water,” *Electrochimica Acta*, vol. 51, no. 17, pp. 3566–3577, Apr. 2006.
[39] M. E. Orazem and B. Tribollet, “Equivalent Circuit Analogs,” in *Electrochemical Impedance Spectroscopy*, John Wiley & Sons, Inc., 2008, pp. 153–162.
[40] D. D. Macdonald and M. Urquidi-Macdonald, “Theory of Steady-State Passive Films,” *J. Electrochem. Soc.*, vol. 137, no. 8, pp. 2395–2402, Aug. 1990.
[41] M. E. Orazem and B. Tribollet, “The Kramers-Kronig Relations,” in *Electrochemical Impedance Spectroscopy*, John Wiley & Sons, Inc., 2008, pp. 427–445.
[42] P. Lu, B. Kursten, and D. D. Macdonald, “Deconvolution of the Partial Anodic and Cathodic Processes during the Corrosion of Carbon Steel in Concrete Pore Solution under Simulated Anoxic Conditions,” *Electrochimica Acta*, vol. 143, no. Supplement C, pp. 312–323, Oct. 2014.
[43] R.-W. Bosch and M. Vankeerberghen, “In-pile electrochemical tests of stainless steel under PWR conditions: Interpretation of electrochemical impedance spectroscopy data,” *Electrochimica Acta*, vol. 52, no. 27, pp. 7538–7544, Oct. 2007.
[44] S. Sharifi-Asl, M. L. Taylor, Z. Lu, G. R. Engelhardt, B. Kursten, and D. D. Macdonald, “Modeling of the electrochemical impedance spectroscopic behavior of passive iron using a genetic algorithm approach,” *Electrochimica Acta*, vol. 102, no. Supplement C, pp. 161–173, Jul. 2013.
[45] D. D. Macdonald, “Some personal adventures in passivity—A review of the point defect model for film growth,” *Russ. J. Electrochem.*, vol. 48, no. 3, pp. 235–258, Mar. 2012.
[46] M. Bojinov *et al.*, “Electrochemical study of the passive behaviour of Ni–Cr alloys in a borate solution—a mixed-conduction model approach,” *J. Electroanal. Chem.*, vol. 504, no. 1, pp. 29–44, May 2001.
[47] I. Betova, M. Bojinov, V. Karastoyanov, P. Kinnunen, and T. Saario, “Effect of water chemistry on the oxide film on Alloy 690 during simulated hot functional testing of a pressurised water reactor,” *Corros. Sci.*, vol. 58, no. Supplement C, pp. 20–32, May 2012.
[48] M. Bojinov, A. Galtayries, P. Kinnunen, A. Machet, and P. Marcus, “Estimation of the parameters of oxide film growth on nickel-based alloys in high-temperature water electrolytes,” *Electrochimica Acta*, vol. 52, no. 26, pp. 7475–7483, Sep. 2007.
[49] T. M. Devine, “Influence of Primary Water Chemistry on Oxides Formed on Alloy 600 and Alloy 690,” in *Proceedings of the 15th International Conference on Environmental*

Degradation of Materials in Nuclear Power Systems — Water Reactors, Springer, Cham, 2011, pp. 967–992.
[50] S. E. Ziemniak and M. Hanson, “Corrosion behavior of NiCrFe Alloy 600 in high temperature, hydrogenated water,” *Corros. Sci.*, vol. 48, no. 2, pp. 498–521, Feb. 2006.
[51] J. Huang, X. Wu, and E.-H. Han, “Electrochemical properties and growth mechanism of passive films on Alloy 690 in high-temperature alkaline environments,” *Corros. Sci.*, vol. 52, no. 10, pp. 3444–3452, Oct. 2010.
[52] H. J. Mathieu and D. Landolt, “An investigation of thin oxide films thermally grown in situ on Fe□24Cr and Fe□24Cr□11Mo by auger electron spectroscopy and X-ray photoelectron spectroscopy,” *Corros. Sci.*, vol. 26, no. 7, pp. 547–559, Jan. 1986.
[53] S. Zhang, Y. Tan, and K. Liang, “Zinc addition changes the semiconductor properties of oxide films of Alloy600 in high temperature water,” *Mater. Lett.*, vol. 68, no. Supplement C, pp. 36–39, Feb. 2012.
[54] P. Bénézeth, D. A. Palmer, D. J. Wesolowski, and C. Xiao, “New Measurements of the Solubility of Zinc Oxide from 150 to 350°C,” *J. Solut. Chem.*, vol. 31, no. 12, pp. 947–973, Dec. 2002.
[55] H. Sun, X. Wu, and E.-H. Han, “Effects of temperature on the protective property, structure and composition of the oxide film on Alloy 625,” *Corros. Sci.*, vol. 51, no. 11, pp. 2565–2572, Nov. 2009.
[56] D. D. Macdonald, “The Point Defect Model for the Passive State,” *J. Electrochem. Soc.*, vol. 139, no. 12, pp. 3434–3449, Dec. 1992.
[57] S. P. Harrington and T. M. Devine, “Analysis of Electrodes Displaying Frequency Dispersion in Mott-Schottky Tests,” *J. Electrochem. Soc.*, vol. 155, no. 8, pp. C381–C386, Aug. 2008.
[58] D. A. Palmer, P. Bénézeth, C. Xiao, D. J. Wesolowski, and L. M. Anovitz, “Solubility Measurements of Crystalline NiO in Aqueous Solution as a Function of Temperature and pH,” *J. Solut. Chem.*, vol. 40, no. 4, p. 680, Apr. 2011.

Appendix

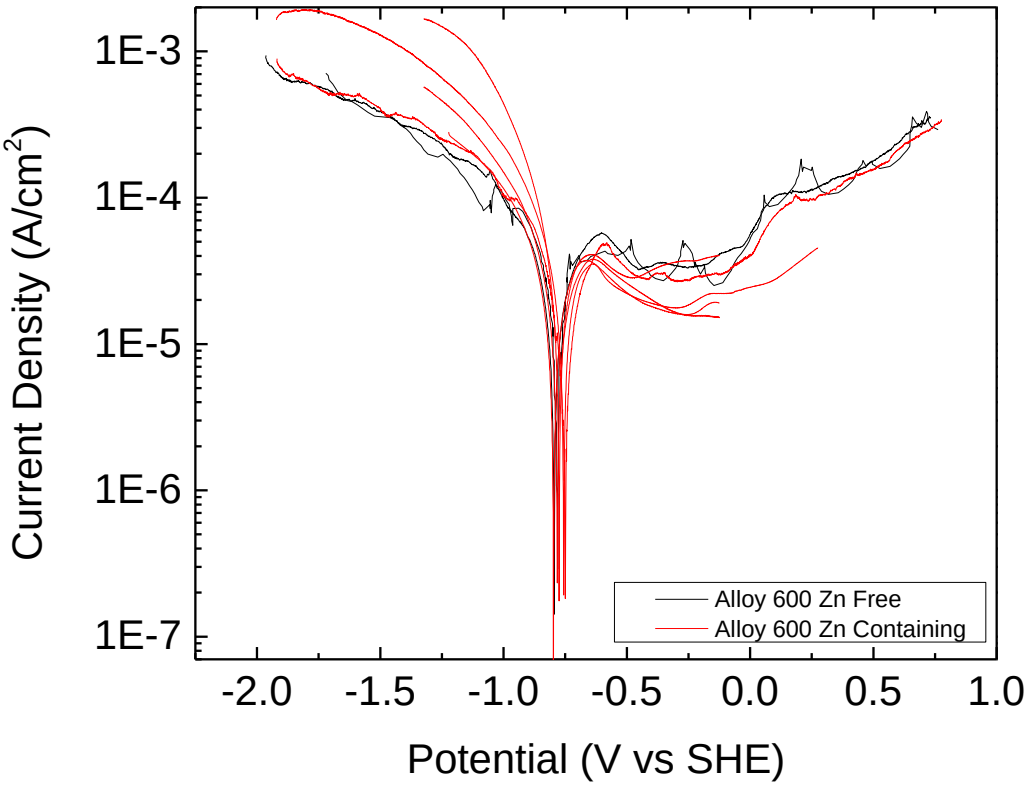

Figure A-1: Polarization curves for Alloy 600 in PWR Primary water at 320°C at 1mV/s. The plot includes 2 scans in Zn free solution and 5 scans in Zn containing solution.